Experimental Design and Implementation of Two Dimensional Transformations of Light in Waveguides and Polarization

Matthew Runyon

A thesis presented under the supervision of Dr. Jeff S. Lundeen for the degree of Master of Science

uOttawa

Department of Physics
University of Ottawa
Ottawa-Carleton Institute for Physics
Canada

October 29th, 2017

© Matthew Runyon, Ottawa, Canada, 2017

Declaration of Authorship

I, Matthew Runyon, declare that this thesis titled, "Experimental design and implementation of two dimensional transformations of light in waveguides and polarization" and the work presented in it are my own. I confirm that:

1. This work was done wholly or mainly while in candidature for a research degree at this University.
2. No part of this thesis has previously been submitted for a degree or any other qualification at this University or any other institution.
3. Where I have consulted the published work of others, this is always clearly attributed.
4. Where I have quoted from or indicated the work of others, the source and/or relevant personnel is always given. With the exception of such quotations and indications, this thesis is entirely my own work.
5. I have acknowledged all main sources of help.

Abstract

Photonics, the technological field that encompasses all aspects of light, has been rapidly growing and increasingly useful in uncovering fundamental truths about nature. It has helped detect gravitational waves, allowed for a direct measurement of the quantum wave function, and has helped realize the coldest temperatures in the universe. But photonics has also had an enormous impact on day-to-day life as well; it has enabled high capacity and/or high speed telecommunication, offered cancer treatment solutions, and has completely revolutionized display and scanning technology. All of these discoveries and applications have required a superb understanding of light, but also a high degree of control over the sometimes abstract properties of light.

The work contained in this thesis explores two novel means of controlling and manipulating two different abstract properties of light. In Part I, the property under investigation is the polarization state of light – a property that is paramount to all light-matter interactions, and even some light-light interactions such as interference. Here, a liquid crystal on silicon spatial light modulator (LCOS-SLM)'s capabilities in manipulating the polarization state of light is theoretically examined and experimentally exploited, tested, and reported on. It is found through experimentation that, for an appropriate range of beam sizes and input polarizations, a single LCOS-SLM can be used to produce any light field with an arbitrary, spatially varying polarization profile. In Part II, the property under investigation loosely corresponds to light's spatial degree of freedom – how light can move from one spot in space to another in a non-trivial manner. Here, control over light's position through a waveguide array through the use of quantum geometric phase is theoretically examined, simulated, and experimentally designed. It is found through simulation that a three-waveguide array is capable of implementing two dimensional unitary transformations.

The common theme between Part I and Part II is manipulating these properties of light to realize classes of general transformations. Moreover, if the light field is treated as a quantum state in the basis of either property under investigation, a two dimensional computational basis ensues. This is precisely the right cardinality for applications in quantum information.

Acknowledgements

I would like to acknowledge my supervisor, Dr. Jeff Lundeen, for his fundamental ideas and discussions with me on all work within this thesis. He has exhibited patience and care throughout my years in his lab (the Lundeen Lab), and has always been willing to help. I consider myself lucky to have had the opportunity to study under his supervision – I have learned a lot from him. There are many others who I would like to thank and acknowledge for various reasons:

Dr. Lambert Giner, a post-doctoral researcher in the Lundeen Lab, has provided many fruitful discussions and has taught me a handful of useful experimental techniques in the realm of optics. His patience and kindness in the process is appreciated and will not be forgotten. Dr. Giner has also granted permission to use two figures he has created in Part I of this thesis. Lastly, Dr. Giner has contributed significantly to the experimental setup in Part I by developing the software - hardware interface in LabView. This proved very useful in automation.

I've had the pleasure of working closely with Mr. Codey Nacke, a co-op student in physics who I supervised for the majority of his co-op term in the Lundeen lab. Mr. Nacke contributed to the experiment in Part I in several ways; he performed many setup calibrations, aided in software development, and participated in taking experimental data. His most notable contribution to the experiment of Part I was a particular software development effort which helped lead to the imaging of a picture of Van Gogh's *'Starry Night'* in polarization.

Dr. Ebrahim Karimi, a professor and colleague, has significantly contributed to the fundamental theoretical ideas behind the experiment in Part I. I've had the pleasure of attending a graduate course he taught and found him to be an excellent lecturer. I thank him for engaging in several discussions with me and always showing utmost courtesy and kindness.

Ms. Alicia Sit, an undergraduate physics student and colleague, has also significantly contributed to the theoretical aspects of the experiment in Part I. I have had the pleasure of presenting alongside Ms. Sit and having pleasant discussions, scientific or otherwise.

I am also grateful to Mr. Hugo Larocque for providing the q-plates that were tested and used for the experiment in Part I. I've enjoyed all of my discussions with him, and I thank him for his willingness to help.

While I have not had the pleasure in meeting Ms. Marissa Granados-Baez, she deserves my thanks and acknowledgement for participating in preliminary aspects of the experiment in Part I.

I've also not had the pleasure in meeting Dr. Xin-Ding Zhang, a Chinese professor who visited the University of Ottawa from Guangzhou the year before I enrolled. Dr. Zhang is responsible for the theory behind the experiment in Part II, having done much work in non-Abelian geometric phase. He also performed the COMSOL simulation that extracted the coupling coefficient for the silicon waveguides, and provided preliminary design parameters for the Hadamard and Pauli-X gate.

I'd like to thank Dr. Robert Boyd, professor and Canada Excellence Research Chair (CERC) in Quantum Nonlinear Optics, for his leadership within the CERC group. It is obvious that Dr. Boyd genuinely wants his students to succeed, and he always presents himself to the group with enthusiasm and kindness. It has been a pleasure to meet him and be part of the team.

During my M.Sc., I participated in a silicon photonics course and workshop, namely the Silicon Electronic Photonics Integrated Circuits (SiEPIC) Passives Workshop. SiEPIC is a Natural Sciences and Engineering Research Council of Canada (NSERC) funded program designed to train undergraduate and graduate students in silicon photonics, directed by Dr. Lukas Chrostowski, a professor at the University of British Colombia. It was through this program that I was able to submit the silicon photonic design of Part II for fabrication. I was also able to use some custom SiEPIC library elements to aid in this design, which I am very grateful for. I'd like to thank Dr. Ksenia Dolgaleva for providing the necessary subscriptions to allow for my participation in this program, and I'd like to thank Dr. Chrostowski for his lectures and efforts with respect to the SiEPIC program, and for joining me for lunch on a few occasions to discuss physics, engineering, and life.

I've had the pleasure of engaging in many friendly discussions and social events with many different people within CERC. While some of these people have already been mentioned, I would also like to acknowledge Mr. Tomás (Jefferson) Florez, Mr. Guillaume Thekkadeth, Mr. Davor Curić, Dr. Orad Reschef, Dr. Enno Giese, Dr. Robert Fickler, and Dr. Mikko Huttunen.

Last but not least, I would like to thank and acknowledge my family, friends, and especially my partner and soul mate, Kristin Wilson, for assisting me in all other aspects of my life to make this thesis possible.

In conclusion, very few achieve greatness / success all on their own. All those mentioned here have contributed to my idea of what success is, and in some cases have helped me step a little closer to it.

Contents

List of Figures

List of Tables

Acronyms

BPP bounded-error probabilistic polynomial time. 67

BQP bounded-error quantum polynomial time. 67

CCD charge coupled device. viii, xi, 8, 17, 21, 23, 25, 32–34, 88

CERC Canada Excellence Research Chair. v

CMC Canadian Microelectronics Corporation. 79

CML compact model library. 79

CMOS complementary metal oxide semiconductor. 26

DUT device under test. 81

EME eigenmode expansion. xi, 66, 81, 85, 86

FDFD finite difference frequency domain. 81

FDTD finite difference time domain. 81

FWTM full width at tenth maximum. x, 36, 57, 62

GQC geometric quantum computation. 66, 67

HWP half waveplate. viii, ix, xi, 14, 18, 21–23, 25, 26, 31, 36, 37, 39

ICP inductively coupled plasma. 79

IME Institute of Microelectronics. 79, 91

LC liquid crystal. 16, 17, 26

LCD liquid crystal display. 17

LCOS-SLM liquid crystal on silicon spatial light modulator. iii, 4

LOQC linear optical quantum computing. 67

LUT look-up table. 28, 32

MMF multi-mode fibre. 13

MMI multi-mode interferometer. 84, 91

MPW multi-project wafer. 79

MZI Mach-Zehnder interferometer. 91

NHQC non-adiabatic holonomic quantum computation. 66, 67, 69

NMR nuclear magnetic resonance. 67

NPBS non-polarizing beamsplitter. viii, 21, 26–28, 30, 64

NSERC Natural Sciences and Engineering Research Council of Canada. v

OAM orbital angular momentum. 18

PBS polarizing beamsplitter. viii, ix, 21, 25, 36, 37

PhC photonic crystal. 84, 91

PMF polarization maintaining fibre. xi, 13, 89, 90

QWP quarter waveplate. viii, xi, 14–16, 21, 25, 26, 37, 39

RWA rotating wave approximation. 74

SDL schematic-driven layout. 78

SIC-POVM symmetric informationally complete positive operator valued measure. ix, 37, 38, 40, 41, 50, 51, 63

SiEPIC Silicon Electronic Photonics Integrated Circuits. v, 79

SLM spatial light modulator. viii, xi, 3, 4, 17, 18, 21–26, 28, 30–34, 36, 37, 40–42, 44, 61–64, 94

SMF single mode fibre. xi, 89, 90

STIRAP stimulated Raman adiabatic passage. 72

TE transverse electric. 81, 86, 88

UV ultraviolet. 79

VGER variable general elliptical retarder. 16

Introduction

This thesis is broken down into two distinct parts and is heterogeneous by design. Part I speaks to free space optics and investigates polarization transformations. The experimental setup was assembled with many optical components, but the true workhorse of this experiment is an active device known as a spatial light modulator. This experiment was carried out to completion with novel experimental results and there is, as of the final submitted version of this thesis, a manuscript in progress.

On the other hand, Part II speaks to integrated optics and investigates waveguide mode transformations. The true workhorse of this experiment was to be a fabricated, passive micro-sized device composed of coupled waveguides. This experiment was not carried out to completion due to an unforeseen delay in fabrication, which was not something the author had control over since this fabrication was performed by a third party (Institute of Microelectronics, Singapore). In lieu of experimental results, the author has obtained numerical results to provide a baseline for future experimental results.

Despite the obvious differences between each experiment, they are intimately related: each experiment investigates two-dimensional transformations on photonic degrees of freedom. Here, dimensionality refers to the cardinality of the Hilbert space defining either degree of freedom. In order to completely specify the polarization state of light, one must express an arbitrary polarization in terms of basis vectors, of which there are two. Polarization is inherently two dimensional. For the waveguide array, there are three waveguides and so, fundamentally, there are three basis vectors required to completely specify the mode. However, only two of these waveguides are able to sustain light within them by design. For all intents and purposes, the third waveguide is neglected so that only a two dimensional subspace of the three dimensional Hilbert space is considered in the mode transformations. Hence, each system is treated two dimensionally.

Since the systems of Part I and Part II are treated two dimensionally, all photonic transformations under study are described mathematically in terms of the Poincaré (Bloch) sphere. The Poincaré sphere is a popular theoretical construct within the field quantum information and offers an excellent visualization of transformations on two dimensional quantum systems (qubits). The Poincaré sphere is introduced and studied in detail in Part I and sees continued use in Part II.

Part I

Polarization Transformations with Spatial Light Modulators

Overview

The sections of Part I are organized as follows: in Chapter 2, a brief motivation and literature review is given for pursuing two dimensional transformations in polarization. Chapter 3 contains theoretical underpinnings as to the description and definition of polarization (Section 2.1), as well as a description of how birefringent media can manipulate polarization in a spatially varying manner (Sections 2.2 - 2.3). Chapter 3 concludes with a general method to measure an arbitrary polarization state known as Stokes Polarimetry (Section 2.4).

Chapter 4 describes the experimental setup that realizes two dimensional polarization transformations. Here, a general description of the system and its subsystems is given (Section 3.1) as well as the setup calibration procedure (Section 3.2) and image processing techniques (Section 3.3).

Chapter 5 contains experimental results containing examples of uniform to uniform transformations (Section 4.1), uniform to non-uniform transformations (Section 4.2), and non-uniform to uniform transformations (Section 4.3). In this context, 'uniform' and 'non-uniform' refer to whether a wave front has a spatially varying polarization ('non-uniform') or not, and therefore also speaks to the complexity of the transformations*.

Chapter 6 is dedicated to the analysis of various errors and uncertainties that exist within the setup, namely those associated with waveplates (Section 5.1), quantization errors (Section 5.2), and errors associated with the optical axes of the SLM pixels (Section 5.3).

Finally, a conclusion of the experiment is offered in Chapter 7.

*There are several words used to describe whether or not a polarization state is spatially varying across the wave front. For example, the terms 'pure' and 'impure' are also used.

Chapter 1

Motivation

Whenever the polarization of a light field is considered in conventional photonic applications, it is assumed to be uniform across the wave front, i.e. the same polarization exists at each infinitesimal point of the wave's transverse profile. Moreover, conventional optical elements can only modify the polarization state in a uniform manner as well. While these uniform polarization transformations have proved useful to date, perhaps more general, non-uniform polarization transformations will lead to other useful applications. Indeed, it has been shown [1] that generating specific non-uniform polarization profiles, i.e. radially polarized light fields, are able to focus more sharply than the same field with a uniform polarization. Perhaps one day non-uniform polarization profiles may offer application to fields such as telecommunications, where various regions of the wave front can serve as independent, polarization-dependent channels. Or perhaps these polarization states can push the boundaries of polarization imaging [2], where graphical information can be encoded in a light field in such a way that is invisible to the naked eye. In any case, a means of arbitrarily manipulating polarization in full generality is critical to maximizing technological capabilities, and the means explored in this work is through LCOS-SLMs.

SLMs are devices that have previously found use in generating light fields with specific intensity and phase profiles in the past decade [3], [4], [5]. Since 2000, there has also been work done in producing spatially varying ('non-uniform') polarization profiles with SLMs, but these works have either only been able to produce final polarization states that are confined to a line or plane of the Poincaré sphere [6], [7], suffer loss from diffractive or interferometric techniques [8], [9], [10], [11], [12], [13], [14], [15], [16], or are solely focused on the production of final polarization states [17], [18], [19], [20], [21], [22]. Here, SLMs are used without any diffractive or interferometric methods to exploit the device's ability to perform polarization transformations in varying degrees of generality; the SLM is able to modify the polarization state of a light field point-by-point across its wave front through two successive phase modulations. While novel, spatially varying polarization profiles are indeed produced, the focus of this work is on the transformations themselves rather than the final output state.

Chapter 2

Theory

2.1 Polarization of Light

The polarization state of light, as explained in its wave-like description, is defined as the spatial dimension in which the light oscillates. There are six polarizations states that are commonly referred to throughout this work. They can all be expressed in terms of two linear polarizations defined with respect to the lab frame of reference. The conventions are as follows [23],

1. *Horizontal* polarization (linear polarization that is parallel with a flat table top in the lab frame), denoted by $|H\rangle$,
2. *Vertical* polarization (linear polarization that is perpendicular to a flat table top in the lab frame), denoted by $|V\rangle$,
3. *Diagonal* polarization, denoted by $|D\rangle = \frac{|H\rangle+|V\rangle}{\sqrt{2}}$,
4. *Antidiagonal* polarization, denoted by $|A\rangle = \frac{|H\rangle-|V\rangle}{\sqrt{2}}$,
5. *Right-circular* polarization, denoted by $|R\rangle = \frac{|H\rangle+i|V\rangle}{\sqrt{2}}$,
6. *Left-circular* polarization, denoted by $|L\rangle = \frac{|H\rangle-i|V\rangle}{\sqrt{2}}$.

These states constitute the *basis vectors* in the three, mutually unbiased bases ($\{H, V\}, \{D, A\}, \{R, L\}$) that can be used to represent a polarization state in the Jones basis with Jones vectors $\vec{v} \in \mathbb{C}^2$. Such a Jones vector takes the following form in the HV basis,

$$\vec{v} = \begin{bmatrix} \cos(\alpha) \\ \sin(\alpha)e^{i\phi} \end{bmatrix}, \tag{2.1}$$

where ϕ is the relative phase difference between the $|H\rangle$ and $|V\rangle$ components and α characterizes the amplitude of each component. Polarization has several other mathematical representations, but none more general than the *Stokes parameters*, a 4-tuple of real numbers $\vec{S} = [s_0, s_1, s_2, s_3]$.

The parameter s_0 represents the intensity of the light field and is used for normalization as follows,

$$\vec{S} = \frac{1}{s_0} \begin{bmatrix} s_1 \\ s_2 \\ s_3 \end{bmatrix}. \tag{2.2}$$

This *reduced* Stokes vector then describes a vector in three-dimensional space, i.e. $\vec{S} \in \mathbb{R}^3$, with $-1 \leq s_i \leq 1$. This allows for a geometrical representation of polarization as a vector on the Poincaré sphere, as shown in Fig. 2.1. The Poincaré sphere is an incredible aid in the visualization of two dimensional quantum states and their transformations. The s_i can be related to the Jones

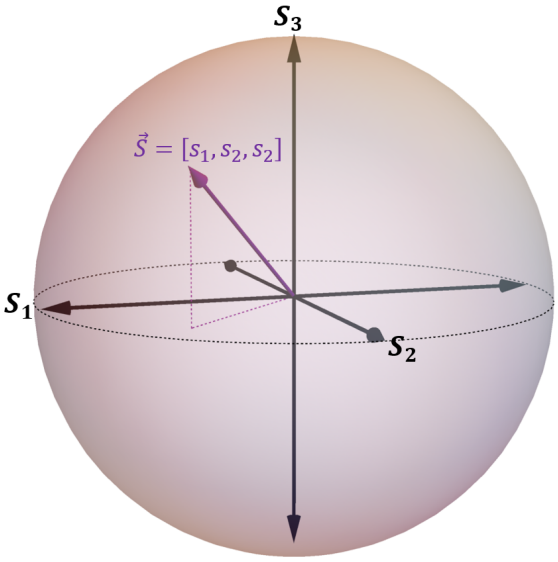

Figure 2.1: Poincaré sphere.

parameters through the following system of equations,

$$s_1 = \cos(2\alpha), \tag{2.3a}$$

$$s_2 = \sin(2\alpha)\cos(\phi), \tag{2.3b}$$

$$s_3 = \sin(2\alpha)\sin(\phi). \tag{2.3c}$$

Each pair of complementary basis vectors are represented by the positive and negative axes of the Poincaré sphere. A graphical representation is shown in Fig. 2.2 to illustrate this, and the convention is as follows,

1. $s_1 = 1$ corresponds to horizontal polarization, $|H\rangle$,
2. $s_1 = -1$ corresponds to vertical polarization, $|V\rangle$,
3. $s_2 = 1$ corresponds to diagonal polarization, $|D\rangle$,
4. $s_2 = -1$ corresponds to antidiagonal polarization, $|A\rangle$,

5. $s_3 = 1$ corresponds to right-circular polarization, $|R\rangle$,

6. $s_3 = -1$ corresponds to left-circular polarization , $|L\rangle$.

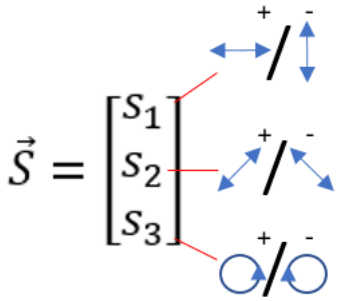

Figure 2.2: Convention for Stokes Parameters

The advantage of the reduced Stokes vector over the Jones vector is that it can also describe an impure (non-uniform) polarization state. This is measured by the *degree of polarization*, $0 \leq \text{DOP} \leq 1$ [24],

$$\text{DOP} = \sqrt{\frac{s_1^2 + s_2^2 + s_3^2}{s_0^2}}, \tag{2.4}$$

which is equivalent to $\left\|\vec{S}\right\|$ for $s_0 = 1$. For $s_0 = 1$, the reduced Stokes vector can also be used to construct a density matrix, $\hat{\rho}$, to describe the polarization quantum mechanically [25],

$$\hat{\rho} = \frac{1}{2}(s_0\hat{\sigma}_0 + s_1\hat{\sigma}_1 + s_2\hat{\sigma}_2 + s_3\hat{\sigma}_3), \tag{2.5}$$

where the $\hat{\sigma}_i$ are the Pauli matrices,

$$\hat{\sigma}_0 = \begin{bmatrix} 1 & 0 \\ 0 & 1 \end{bmatrix}, \quad \hat{\sigma}_1 = \begin{bmatrix} 1 & 0 \\ 0 & -1 \end{bmatrix}, \quad \hat{\sigma}_2 = \begin{bmatrix} 0 & i \\ -i & 0 \end{bmatrix}, \quad \hat{\sigma}_3 = \begin{bmatrix} 0 & 1 \\ 1 & 0 \end{bmatrix}, \tag{2.6}$$

and,

$$s_i = \text{Tr}(\hat{\sigma}_i\hat{\rho}). \tag{2.7}$$

The density matrix and the Stokes vector are the only representations that can describe an impure (non-uniform) polarization state as well as pure (uniform) polarization states. In this work, both representations are used. When a density matrix is used, an alternative measure of how impure the polarization of a light field is given by the *quantum purity*, $\frac{1}{2} \leq P \leq 1$,

$$P = \text{Tr}(\hat{\rho}^2) = \frac{1 + \left|\vec{S}\right|}{2}. \tag{2.8}$$

For a completely mixed state, $P = \frac{1}{2}$. For a pure state, $P = 1$. Finally, for pure states only, one may also represent a polarization state graphically with the polarization ellipse, as shown in Fig. 2.3. This representation consists of only two parameters; the major axis, Ψ, and the ellipticity, χ.

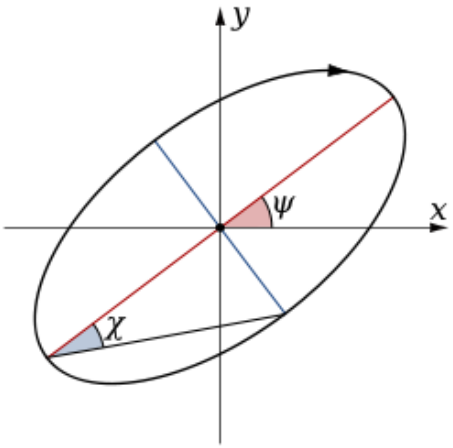

Figure 2.3: The polarization ellipse.

The elliptical representation of polarization is linked to the Stokes parameters by the following relations,

$$2\Psi = \tan^{-1}\frac{s_2}{s_1}, \tag{2.9a}$$

$$2\chi = \tan^{-1}\frac{s_3}{s_1^2 + s_2^2}. \tag{2.9b}$$

This representation finds utility in qualitative graphical representations of wave front polarizations, as described in Section 2.1.1.

2.1.1 Graphical Polarization Representation

It is often useful to be able to quickly check what a measurement of polarization yielded qualitatively through a graphical method. Often times, a Stokes vector alone does not offer an intuitive, geometrical description of what the polarization state is. The polarization ellipse addresses this deficiency, and an example is shown in Fig. 2.4.

Here, roughly each pixel on the CCD camera (detector) is ascribed to a unique polarization ellipse. Upon inspection, one can immediately see which regions of the detected light field are more elliptical or more linear in polarization than others. One problem with this representation is one cannot determine the handedness of each ellipse upon inspection. In order to graphically display a more complete picture of the polarization, one needs to return to a description with Stokes components.

Instead of generating a single image where each pixel on the CCD camera is depicted by a polarization ellipse, one can generate three images where each image's pixels denote a particular Stokes component. For example, the pixels of the first image may correspond to the s_1 component, the pixels of the second image may correspond to the s_2 component, and the pixels of the third image may correspond to the s_3 component. The magnitude of each component (recall $-1 \leq s_i \leq 1$) is described by a *colour map*. This colour map is constructed such that a minimum value

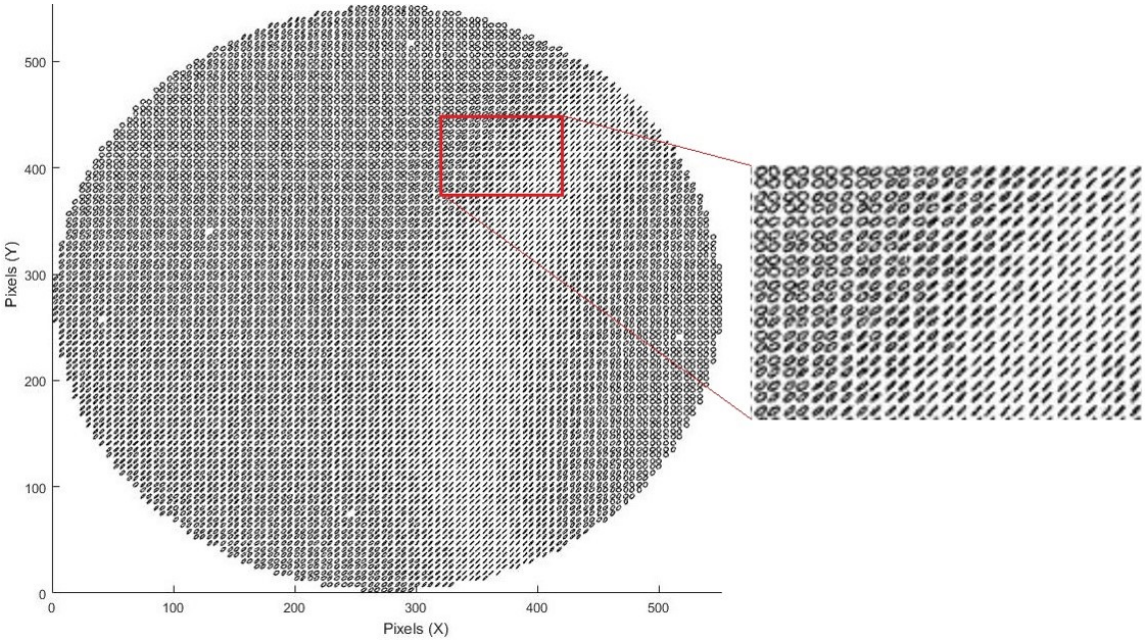

Figure 2.4: The polarization of a light field is represented by a polarizaton ellipse at each pixel of a CCD camera. One can see that the upper left portion of the highlighted region is more circular in comparison to the bottom right region, indicating that the polarization here has a higher ellipticity.

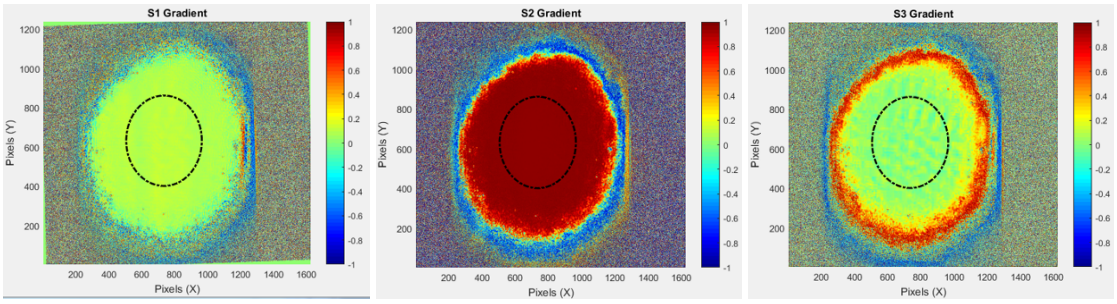

(a) Colourmap of s_1 component (b) Colourmap of s_2 component (c) Colourmap of s_3 component

Figure 2.5: The polarization of a light field is represented by Stokes components at each pixel of a CCD camera. This visual method makes non-uniformities in polarization strikingly obvious, since each pixel can have a distinct colour. The black dotted line indicates the $1/e^2$ beam waist.

of -1 corresponds to a blue colour, a maximum value of +1 corresponds to a red colour, and an intermediate value of 0 corresponds to a green colour.

2.2 Polarization Transformations

2.2.1 General Transformations

A polarization transformation $\hat{T}$ can be defined as a linear map of the set of all Stokes vectors onto itself,

$$\hat{T} : \vec{S} \rightarrow \vec{S}. \tag{2.10}$$

In the most general case, this mapping can be visualized as a three dimensional rotation by an angle ζ about an arbitrary axis $\hat{k}$ in the Poincaré sphere,

$$\hat{T} \equiv \hat{R}(\zeta, \hat{k}), \tag{2.11}$$

where $\hat{R}(\zeta, \hat{k}) \in SO(3)$ (the *special orthogonal group of dimension 3*) and the angle ζ is referred to as the *retardance*. A visual representation is shown in Fig. 2.6 on the Poincaré sphere.

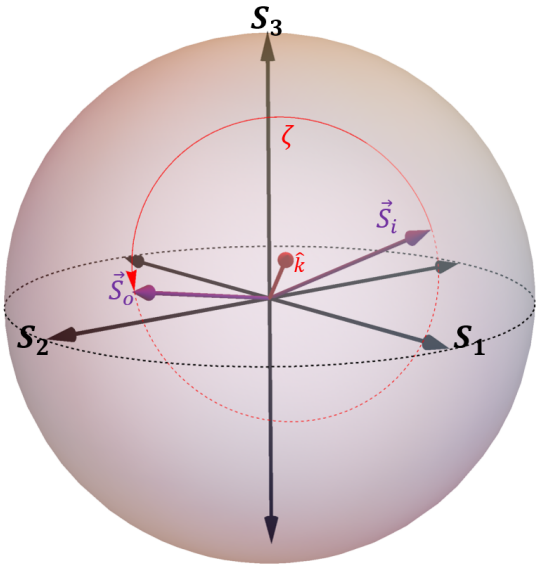

Figure 2.6: A general polarization transformation. The rotation angle is denoted by ζ, the axis of rotation is denoted by $\hat{k}$.

Formalizing polarization transformations in the form of Eq. (2.11) implies generality in that the retardance between $\vec{S}_i$ and $\vec{S}_o$ is fixed [26]; regardless of the input state $\vec{S}_i$, the angular displacement between $\vec{S}_i$ and the output state $\vec{S}_o$ is the same – the transformation does not discriminate against the choice of $\vec{S}_i$. If the retardance ζ and the orientation of the rotation axis $\hat{k}$ can both be tuned arbitrarily, a transformation from any $\vec{S}_i$ to any $\vec{S}_o$ is possible. These transformations are mentioned because there is a subtle distinction between them and what is experimentally implemented in this work, which is elucidated in the following subsection.

2.2.2 Two-Step Transformations

Other useful transformations can be described in a similar formalism, but with less generality. In particular, a two-step process composed of two successive rotations with *fixed* rotation axes $\hat{k}_1$, $\hat{k}_2$ can convert a *subset* of all arbitrary input states $\vec{S}_i$ to any arbitrary output state $\vec{S}_o$, provided both input and output states are known *a priori*. These two-step transformations describe the theory behind the main experimental aspect of this work and are explained below. For a visual representation on the Poincaré sphere, see Fig. 2.7.

Consider a particular subset of Stokes vectors $\vec{S}' \subseteq \vec{S}$ that is yet to be defined. Consider the following *one-to-many* mapping,

$$\hat{T}_{\vec{S}_i \to \vec{S}_o} : \vec{S}' \to \vec{S}. \tag{2.12}$$

This mapping can be implemented with two successive, orthogonal rotations, each confined to a distinct two-dimensional plane,

$$\hat{T}_{\vec{S}_i \to \vec{S}_o} \equiv \hat{R}(\zeta_2, \hat{k}_2)\hat{R}(\zeta_1, \hat{k}_1). \tag{2.13}$$

In terms of the Poincaré sphere, the orthogonal axes of rotation are chosen to be fixed with $\hat{k}_1 = S_1$ and $\hat{k}_2 = S_2$. To produce a desired mapping from $\vec{S}_i = [s_1^i, s_2^i, s_3^i] \in \vec{S}'$ to $\vec{S}_o = [s_1^o, s_2^o, s_3^o] \in \vec{S}$, the retardances ζ_1 and ζ_2 are *not* fixed and can be calculated for each valid mapping of interest. They are given by Sit *et al.* [26] as,

$$\zeta_1 = \tan_2^{-1}\left(\frac{\operatorname{sgn}(s_2^i s_3^m - s_3^i s_2^m)\left|[0, s_2^i, s_3^i] \times [0, s_2^m, s_3^m]\right|}{[0, s_2^i, s_3^i] \cdot [0, s_2^m, s_3^m]}\right) \bmod 2\pi, \tag{2.14}$$

$$\zeta_2 = \tan_2^{-1}\left(\frac{\operatorname{sgn}(s_1^o s_3^m - s_3^o s_1^m)\left|[s_1^m, 0, s_3^m] \times [s_1^o, 0, s_3^o]\right|}{[s_1^m, 0, s_3^m] \cdot [s_1^o, 0, s_3^o]}\right) \bmod 2\pi, \tag{2.15}$$

$$\vec{S}_m = \left[s_1^i, s_2^o, \operatorname{sgn}(s_3^o)\left(\sqrt{\left(s_3^i\right)^2 + \left(s_2^i\right)^2 - \left(s_2^o\right)^2}\right]\right., \tag{2.16}$$

where $\vec{S}_m = \hat{R}(\zeta_1, \hat{S}_1)\vec{S}_i$ is an intermediate polarization state that results from the first rotation and serves as the starting point for the second rotation. Note that the inverse tangent function $\tan_2^{-1}\left(\frac{y}{x}\right)$ in Eq. (2.14) and Eq. (2.15) is the *four quadrant* inverse tangent function, which is defined for $-\pi \leq \tan_2^{-1}\left(\frac{y}{x}\right) \leq \pi$ [27]. Geometrically, these formulae give the positive angle ζ_i between two vectors that are confined to the $S_i - S_3$ plane. Eq. (2.14) has an angular reference to $\vec{S}_i$ and Eq. (2.15) has an angular reference to $\vec{S}_m$. While this two-step process is useful in implementing many state-to-state mappings, generality is lost since the required retardances ζ_i for a desired transformation are explicitly dependent on $\vec{S}_i$ and $\vec{S}_o$, as is evident from Eq. (2.14) and Eq. (2.15). Furthermore, only a certain subset $\vec{S}'$ of all possible $\vec{S}_i$ can be used to reach *any* desired $\vec{S}_o$. This subset is determined by the axes of rotation, $\hat{k}_1$ and $\hat{k}_2$, as well as their ordering. The requirement defining the valid $\vec{S}_i$ (the subset $\vec{S}'$) is that if the first rotation is about $\hat{k} = [k_1, k_2, k_3]$, then $\vec{S}_i$ must satisfy,

$$k_1\left(s_1^i\right) + k_2\left(s_2^i\right) + k_3\left(s_3^i\right) = 0. \tag{2.17}$$

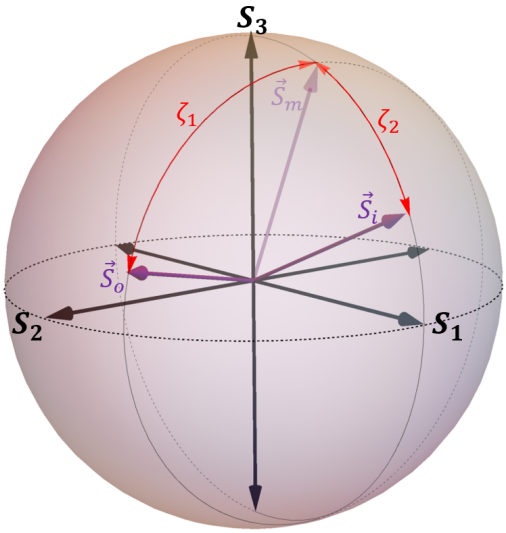

Figure 2.7: A two-step transformation $\hat{T}_{\vec{S}_i \to \vec{S}_o}$. Here, $\vec{S}_i$ rotates about $\hat{S}_2$ by an angle ζ_2, to an intermediate state $\vec{S}_m$. $\vec{S}_m$ then rotates about $\hat{S}_1$ by an angle ζ_1 to reach the final output state $\vec{S}_o$.

For the case of Eq. (2.13) with $\hat{k}_1 = S_1$ and $\hat{k}_2 = S_2$ (as in this experiment), this implies that $\vec{S}_i$ must have a vanishing s_1 component in order to map to any desired $\vec{S}_o$. This loss of generality is obvious upon geometrical considerations, as illustrated in Fig. 2.8. If one views the Poincaré sphere from above the S_3 axis and looks directly down the S_3 axis, only the $S_1 - S_2$ plane is visible. For the choice of $\vec{S}_i$ shown, the possible $\vec{S}_o$ are confined within the purple solid lines since the rotation of $\vec{S}_i$ about S_1 can only have an extent along S_2 as far as the extent of the Poincaré sphere itself along S_2.

Thus, due to the requirement of knowing $\vec{S}_i$ and $\vec{S}_o$ a priori and the restriction of possible input states for an arbitrary output state, this transformation is not completely general. As a particular example, imagine one sought to modify the polarization coming out of a physically stable multi-mode fibre (MMF). Contrary to a PMF, the nature of a MMF will, in general, produce a polarization at its output that is different from its input – the MMF performs some polarization transformation on the input state. One could not use this two-step transformation to *un-do* this polarization transformation in complete generality. One would have to measure the output polarization of the MMF, and then use Eq. (2.14) - Eq. (2.16) to determine the appropriate ζ_i that will revert the MMF output polarization back to its input polarization. However, as soon as the output polarization of the MMF is no longer that which was used in the calculation of ζ_i (which may happen by simply changing the input polarization to the MMF), then ζ_i needs to be recalculated. A general transformation would not require any recalculation, it would simply *un-do* the transformation performed by the MMF regardless of the input (and output) to (and from) the MMF.

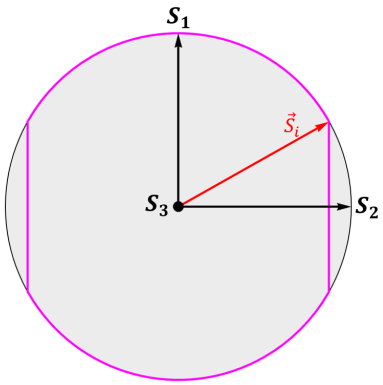

Figure 2.8: A view of the Poincaré sphere looking directly down the S_3 axis. Since the first rotation is about $\hat{S}_1$ and $\vec{S}_i$ has $s_1 \neq 0$, the possible $\vec{S}_o$ are restricted to the area within the magenta perimeter.

2.3 Birefringent Media

2.3.1 General Considerations

A material which displays two different indices of refraction is said to be *birefringent*. In crystals, which are solids defined by a high degree of atomic ordering, this property is the result of anisotropic binding forces creating an anisotropy in the refractive index. Birefringence in crystals is thus a geometric property, and any light travelling through such a crystal will, in general, encounter an asymmetric atomic structure [28]. The consequence of this asymmetry can be profound for polarization effects. In particular, the $|H\rangle$ and $|V\rangle$ components of a light field can acquire a relative phase difference after travelling through such a crystal, thereby changing the polarization.

A crystal is said to be characterized by a particular *optic axis*, which is the direction through the crystal where the atoms are arranged symmetrically [28]. When there is only one such direction, the crystal is said to be *uniaxial*. This optic axis whose orientation is denoted by $\hat{c}$, helps to define the two different indices of refraction of a birefringent crystal as follows:

Consider a light field characterized by the following electric field vector with wave vector $\vec{k}$, frequency ω, amplitude A, and arbitrary polarization direction $\hat{p}$,

$$\vec{E}(\vec{r},t) = Ae^{i(\vec{k}\cdot\vec{r}-\omega t)}\hat{p}. \tag{2.18}$$

If the polarization $\hat{p}$ is oriented along $\hat{c}\times\hat{k}$, $\vec{E}(\vec{r},t)$ is said to experience the *extraordinary* index of refraction, n_e. If $\hat{p}$ is orthogonal to $\hat{c}\times\hat{k}$, $E(\vec{r},t)$ is said to experience the *ordinary* index of refraction, with $n_o \neq n_e$. It is worth noting that n_e is, in general, a function of the angle θ (in addition to the wavelength) between the optic axis and $\vec{k}$ according to [29],

$$\frac{1}{n_e(\theta)^2} = \frac{\sin^2(\theta)}{\bar{n}_e^2} + \frac{\cos^2(\theta)}{n_o^2}, \tag{2.19}$$

where $\bar{n}_e$ is the *principal* extraordinary index of refraction, defined when $\theta = \frac{\pi}{2}$.

With these considerations, the $|H\rangle$ and $|V\rangle$ components of $\vec{E}(\vec{r},t)$ can experience distinct phases, thereby transforming the polarization from $\hat{p}$ to $\hat{p}'$. If $\hat{c}$ is along the horizontal or vertical, a uniaxial crystal may be described in the HV basis as a 2 x 2 matrix,

$$\mathrm{LC}\,(\zeta) = \begin{bmatrix} 1 & 0 \\ 0 & e^{i\zeta} \end{bmatrix}, \tag{2.20}$$

where ζ is the phase difference between the $|H\rangle$ and $|V\rangle$ components of $\vec{E}(\vec{r},t)$ after traversing a distance d within the crystal,

$$\zeta = \frac{2\pi d}{\lambda}(n_e - n_o). \tag{2.21}$$

Eq. (2.20) implies that this polarization transformation is unitary, i.e. $LC \in SU(2)$ (the *special unitary group of dimension 2*). Since *SU(2)* is homomorphic to *SO(3)* [30], the transformation can be visualized as a rotation about an axis, just as described in Section 2.2. Under the circumstances leading to Eq. (2.20), the particular axis of rotation is the S_1 axis of the Poincaré sphere, and the relative phase between the $|H\rangle$ and $|V\rangle$ components is, again, the retardance ζ. Thus, a uniaxial crystal performs unitary polarization transformations that can be described as rotations on the Poincaré sphere, $\hat{R}(\zeta,\hat{k})$.

2.3.2 Waveplates

Waveplates, which are tremendously popular in optics, are passive devices made from uniaxial crystals. The most common wave plates are the QWP and the HWP, whose names derive from the amount of retardance they nominally impart to a light field. Waveplates have a fixed retardance for a given wavelength, but are constructed so that the orientation of the optic axis, $\hat{c}$, is tunable. The ability to tune $\hat{c}$ is made possible by placing the uniaxial crystal inside of a rotating housing such that any incident light field will have $\hat{k} \perp \hat{c}$. A common waveplate and housing is shown in Fig. 2.9.

The transformation that a waveplate performs can also be described by a three dimensional rotation consistent with Eq. (2.11). Here, the retardance ζ is defined by the thickness of the waveplate as per Eq. (2.21), and the axis of rotation $\hat{k}$ lies in the $S_1 - S_2$ plane at an angle 2Φ from the positive S_1 axis, where Φ is the angle between the optic axis $\hat{c}$ and the horizontal [26]. In the case of a HWP, the retardance is $\zeta = \pi$. In the case of a QWP, the retardance is $\zeta = \frac{\pi}{2}$.In the language of Section 2.2.1, the HWP and QWP can be assigned the transformations,

$$\mathrm{HWP}\,(2\Phi) = \hat{R}(\pi, 2\Phi), \tag{2.22}$$

$$\mathrm{QWP}\,(2\Phi) = \hat{R}(\frac{\pi}{2}, 2\Phi). \tag{2.23}$$

While either of these waveplates alone implement a transformation consistent with Eq. (2.11), they are not general since they have a fixed retardance and the axis of rotation is only tunable within the $S_1 - S_2$ plane. This implies that one waveplate alone cannot perform any arbitrary polarization state-to-state transition.

In order to perform arbitrary state-to-state transitions with waveplates, one needs to make use of both QWPs **and** HWPs. General unitary transformations are also possible with specific combinations of three or four of these waveplates. As a specific example, there exists a variable

Figure 2.9: A QWP manufactured by Union Optics. In the black, inner-most circular region, one can see two lines which indicate the orientation of the optic axis.

general elliptical retarder (VGER), which is composed of the following sequence of waveplates [31],

$$\text{VGER} \equiv \text{QWP}\left(2\Phi\right)\text{HWP}\left(2\Phi'\right)\text{QWP}\left(2\Phi\right)^{-1}\text{HWP}\left(2\Phi''\right). \tag{2.24}$$

The VGER provides an arbitrary retardance about an arbitrary axis. The trouble is that these devices can only implement these transformations in a uniform manner, i.e. each point in the wave front will experience the same effect, and mechanically rotating the waveplates to appropriately orient the fast axis can be cumbersome.

2.3.3 Liquid Crystals

A liquid crystal (LC) is a state of matter so named because it has properties of both liquids and crystals. One important crystalline property that LCs can display is a high degree of order, namely in the arrangement of each molecule's orientation throughout the LC. This molecular arrangement in LC devices gives rise to birefringence, much like the uniaxial crystals described in Section 2.3.1. Thus, under the appropriate conditions, LCs obey Eq. (2.20).

LCs are novel because the birefringence they exhibit is electrically tunable. For *nematic phase* liquid crystal devices, as used in this work, the constituent molecules are long and rod shaped, as shown in Fig. 2.10. These molecules form permanent electric dipoles - they will align themselves with the direction of any externally applied electric field. When driven by an electric field, the molecules can fall in and out of alignment with various orientations, thus changing the birefringence and therefore the retardance, ζ, of the material.

Due to this tunable retardance, LCs can also be combined with waveplates to realize various polarization transformations, as will be explained in more generality in Section 2.3.4.

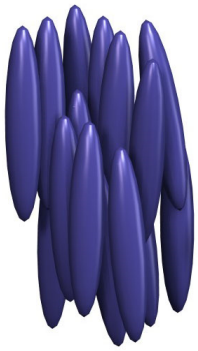

Figure 2.10: Long, rod-shaped liquid crystal molecules aligning in nematic phase.

2.3.4 Spatial Light Modulators

A SLM is an array of LC cells, much like a liquid crystal display (LCD). Thus, one might describe the action of an ideal SLM as a discrete extension of Eq. (2.20),

$$\mathrm{SLM}_{ij}\left(\zeta_{ij}\right) = \begin{bmatrix} 1 & 0 \\ 0 & e^{i\zeta_{ij}} \end{bmatrix}. \tag{2.25}$$

Each individual LC cell is indexed as (i, j) and serves as a polarization rotator, $\hat{R}\left(\zeta_{ij}, \hat{S}_1\right)$. Each LC cell in the array at position (i, j) has the same fixed optic axis but can be electrically biased individually to acquire a distinct retardance ζ_{ij}. A light field incident on an SLM can then undergo distinct polarization transformations in distinct regions of the wave front, which produces a non-uniform polarization profile. An example of these discretized regions of a light field is shown in Fig. 2.11.

The implementation of the two-step transformation of Eq. (2.13) can now be fully described, where a non-uniform transformation can be made on a particular set of input states $\vec{S}_i \in \vec{S}'$ to reach a non-uniform desired output state $\vec{S}_o \in \vec{S}$ with an arbitrary polarization in each discrete region (i, j) of the wavefront. If the axis of rotation of the SLM is aligned with the horizontal such that the nominal rotation of the polarization state is about S_1, one can realize a more general, discretized version of Eq. (2.13) as follows [26],

$$\hat{R}(\zeta'_{ij}, \hat{k}_2)\hat{R}(\zeta_{ij}, \hat{k}_1) \equiv \mathrm{HWP}\left(\frac{\pi}{8} + \frac{\pi}{2}\right)\mathrm{SLM}\left(\zeta'_{ij}\right)\mathrm{HWP}\left(\frac{\pi}{8}\right)\mathrm{SLM}\left(\zeta_{ij}\right). \tag{2.26}$$

Eq. (2.26) implies that the two-step polarization transformation is realized by having a light field sequentially operated on by a SLM, HWP, another SLM, and another HWP – one actually needs two phase modulations from two SLMs. Ideally, one would have two transmissive SLMs in sequence with a HWP after each SLM, but one may also make do with one reflective SLM. For one reflective SLM, the light field must make two incidences on the SLM with one HWP before and after the second incidence. Intuitively, the first HWP has the effect of rotating the polarization state by $\frac{\pi}{4}$ and the second HWP rotates it back. This allows for the SLM to first rotate a polarization state about one axis of the Poincaré sphere before the first HWP, and rotate the polarization state

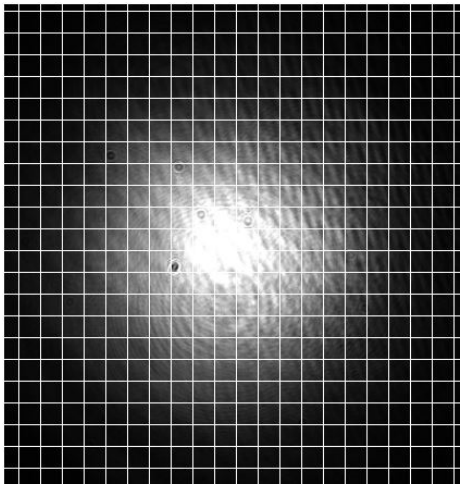

Figure 2.11: The light field is discretized into discrete cells, each corresponding to a pixel on the CCD camera. Cell size is exaggerated for clarity.

about a second orthogonal axis before the second HWP. The second HWP completes the final polarization rotation to the desired polarization state. The presence of two orthogonal rotation axes implies a Stokes vector can be rotated *anywhere* on the Poincaré sphere.

2.3.5 q-plates

A q-plate is a passive, birefringent device made of a vortex-patterned liquid crystal film that has found use in modifying the orbital angular momentum (OAM) content of light fields [32]. Unlike the other birefringent media discussed in this section, the q-plate is a *multiaxial* device; it has many different optic axes. Moreover, due to the liquid crystalline nature of the q-plate, its birefringence is variable by applying a voltage across it. One key parameter in classifying a q-plate is the *topological charge* q of the q-plate, which can take on positive or negative integer or half integer values. Intuitively, this value is proportional to how many times the azimuthal variation of the optic axes reach horizontal between 0 and 2π (see Fig. 2.12). Moreover, for a q-plate with topological charge q, an incident light field will acquire $2q\hbar$ of OAM. In addition to a q-plate's capability in modify-

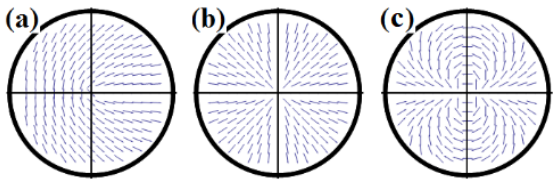

Figure 2.12: Multiaxial representation of q-plates with various topological charge: (a) q-plate with $q = 1/2$, b) q-plate with $q = 1$, c) q-plate with $q = 2$. Image taken (with written permission) from Ebrahim Karimi's Ph.D thesis [33].

ing the OAM content of light fields, they can also produce spatially varying polarization states. This can be intuitively understood by considering the discussion of Section 2.3.1 and treating the multiaxial nature of a q-plate in terms of locally uniaxial sections.

2.4 Stokes Polarimetry

Stokes polarimetry is a statistical method to measure each Stokes parameter of a light field. This enables the reconstruction of the density matrix that describes the polarization state of the light field, and is, in this work, hence also referred to as quantum state tomography.

There are a few important features that a quantum system must exhibit in order for quantum state tomography to be valid. First, the particle whose quantum state one wishes to measure must be available in abundance with perfect reproducibility. This is because many measurements of the particle are required for statistical accuracy, and so it is assumed that identical measurements on any two particles in an ensemble would yield results with identical probabilities.

The general idea is to project the state one seeks to measure, $\hat{\rho}$, onto each positive and negative axis of the Poincaré sphere*. The intensity of the projections are, by themselves, enough to reconstruct the Stokes parameters or density matrix. More formally, consider the following projectors,

$$\hat{P}_{|H\rangle} = |H\rangle \langle H| , \tag{2.27a}$$

$$\hat{P}_{|V\rangle} = |V\rangle \langle V| , \tag{2.27b}$$

$$\hat{P}_{|D\rangle} = |D\rangle \langle D| , \tag{2.27c}$$

$$\hat{P}_{|A\rangle} = |A\rangle \langle A| , \tag{2.27d}$$

$$\hat{P}_{|R\rangle} = |R\rangle \langle R| , \tag{2.27e}$$

$$\hat{P}_{|L\rangle} = |L\rangle \langle L| . \tag{2.27f}$$

The Pauli matrices are recovered from these projectors as follows,

$$\hat{\sigma_0} = \hat{P}_{|H\rangle} + \hat{P}_{|V\rangle}, \tag{2.28a}$$

$$\hat{\sigma_1} = \hat{P}_{|H\rangle} - \hat{P}_{|V\rangle}, \tag{2.28b}$$

$$\hat{\sigma_2} = \hat{P}_{|R\rangle} - \hat{P}_{|L\rangle}, \tag{2.28c}$$

$$\hat{\sigma_3} = \hat{P}_{|D\rangle} - \hat{P}_{|A\rangle}. \tag{2.28d}$$

By Eq. (2.7), $s_i = \mathrm{Tr}(\hat{\sigma_i}\hat{\rho})$. Due to the linearity of the trace operator [35], each s_i can be expressed in terms of the projectors,

$$s_0 = \mathrm{Tr}\left(\hat{P}_{|H\rangle}\hat{\rho}\right) + \mathrm{Tr}\left(\hat{P}_{|V\rangle}\hat{\rho}\right)), \tag{2.29a}$$

$$s_1 = \mathrm{Tr}\left(\hat{P}_{|H\rangle}\hat{\rho}\right) - \mathrm{Tr}\left(\hat{P}_{|V\rangle}\hat{\rho}\right)), \tag{2.29b}$$

*Projecting onto each positive and negative axis gives an overcomplete set of data. It has been shown [34] that the quantum state tomography of a light field requires only four measurements.

$$s_2 = \mathrm{Tr}\left(\hat{P}_{|R\rangle}\hat{\rho}\right) - \mathrm{Tr}\left(\hat{P}_{|L\rangle}\hat{\rho}\right)), \tag{2.29c}$$

$$s_3 = \mathrm{Tr}\left(\hat{P}_{|D\rangle}\hat{\rho}\right) - \mathrm{Tr}\left(\hat{P}_{|A\rangle}\hat{\rho}\right)). \tag{2.29d}$$

Each matrix trace in Eq. (2.29) is a probability of measuring a particular state. These probabilities are analogous to normalized measurements of polarization-dependent intensity in the lab.

Finally, an application of Eq. (2.5) reconstructs the density matrix of the previously unknown quantum state, $\hat{\rho}$.

Chapter 3

Experimental Setup

3.1 Description

In Fig. 3.1, 636 nm light from a Thorlabs LDM9LP single mode pigtailed diode laser is coupled to a Thorlabs SM600 single mode fibre. The fibre is collimated in free space by a $f = 11$ mm aspheric lens. The $1/e^2$ beam waist is expanded from 550 μm after the lens to 1.28 mm after transmitting through two plano-convex lenses with focal lengths of 75 mm and 175 mm. The light transmits through a balanced PBS, QWP, and HWP at the input polarization tuning stage so that the input polarization is well defined. The light transmits through the first 50:50 NPBS before the first incidence on the SLM, where the first phase modulation occurs. The light is reflected off of the SLM and first NPBS and directed through a HWP, which, as described in Section 3.1.1, is responsible for providing an orthogonal rotation axis such that a proper two-step polarization transformation can occur. The light transmits through a second 50:50 NPBS before its second incidence on the SLM, where a second phase modulation occurs. Finally, the light reflects off of the SLM and second NPBS and is directed through a QWP, HWP, and PBS before being captured by a CCD camera. The CCD camera operates at an exposure time of 0.65 seconds with zero gain. Due to the presence of the PBSs and NPBSs, the total power at the output is, at most, 6.25% of the input power. Specific details of each component are given in Table 3.1 - Table 3.4.

Component	Manufacturer	Model	Diameter (in.)	Type
M_1-M_4	Newport	Valumax ER.2	1	Silver
M_5	Thorlabs	PFD10-03-P01	1	Silver

Table 3.1: Mirror specifications.

3.1.1 The Intermediate Half Waveplate

As alluded to in Section 3.1, the light field must pass through a HWP in between incidences on the SLM. This is because the SLM is only able to rotate the polarization state about one axis of the Poincaré sphere. In order to realize a more general transformation, a second rotation about an orthogonal axis is necessary, as described by Eq. (2.26). The *intermediate* HWP does exactly this;

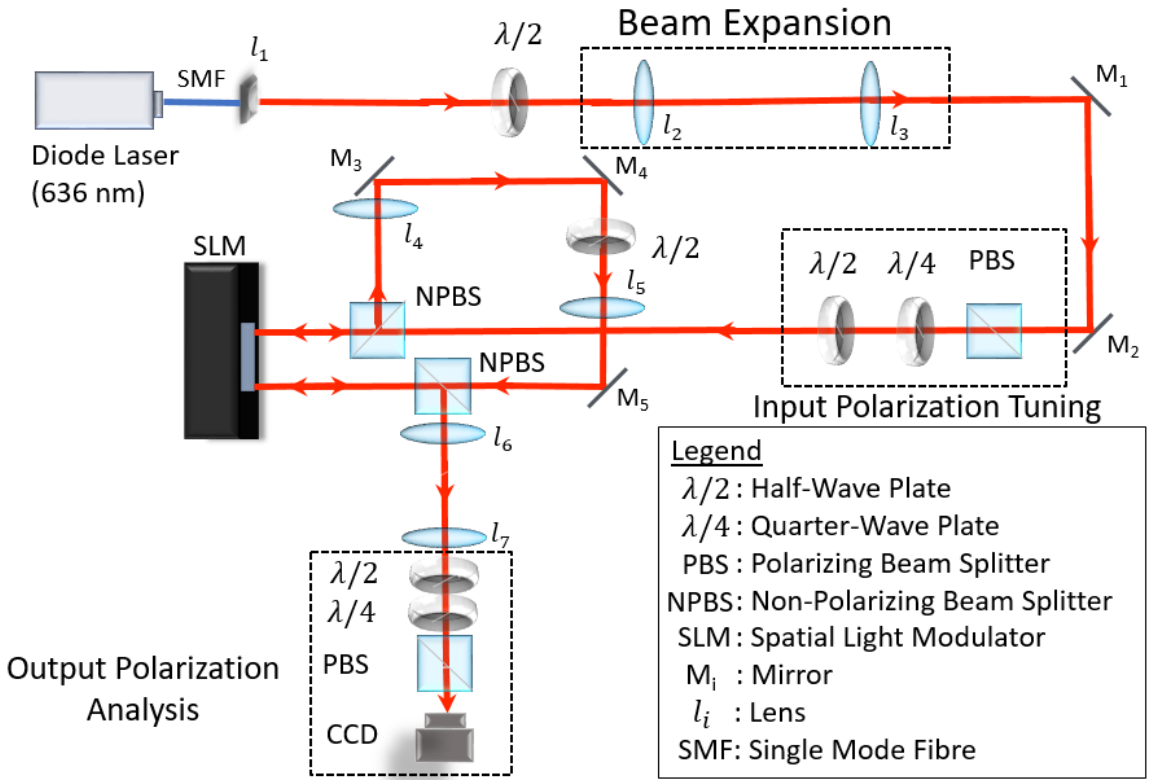

Figure 3.1: Schematic of experimental setup.

Component	Manufacturer	Diameter (in.)	Focal Length (mm)	Type
l_1	Thorlabs	0.22	11	Aspheric
l_2	Edmund Optics	1	75	Plano Convex Fused Silica
l_3	Edmund Optics	1	175	Plano Convex Fused Silica
l_4-l_7	Edmund Optics	1	100	Plano Convex Fused Silica

Table 3.2: Lens specifications.

Nominal Retardance	Manufacturer	Wavelength (nm)	Type
$\lambda/2$	Thorlabs	633	True Zero Order
$\lambda/4$	Thorlabs	633	True Zero Order

Table 3.3: Waveplate specifications.

the first phase modulation from the SLM rotates the initial polarization state $\vec{S}_i$ about the S_1 axis to an intermediate polarization state, $\vec{S}_m$, by imparting a phase ζ_{ij} at each discrete region (i, j) of the wave front,

$$\vec{S}_m = \text{SLM}\left(\zeta_{ij}\right)\vec{S}_i. \tag{3.1}$$

Device	Dimensions	Pixel Size (μm)	Frames Per Second	Pixel Bit Depth
CCD camera	1626 x 1236	4.4 x 4.4	20	12
SLM	792 x 600	20 x 20	60	8

Table 3.4: Basler aca1600-20gm CCD and Hamamatsu LCOS-SLM X10468-07 specifications.

The subsequent action of the intermediate HWP and SLM rotates $\vec{S}_m$ about the S_2 axis by ζ'_{ij} at each discrete region i, j of the wave front. According to Eq. (2.26), a final HWP should exist after the last phase modulation from the SLM to rotate the polarization state to $\vec{S}_o$. In order to reduce the complexity of the setup, this final waveplate is removed as its absence can be compensated for in the data analysis by simply swapping the definitions of the Stokes components s_1 and s_2 with one another.

3.1.2 4f Focusing System(s)

If a light field has a highly non-uniform polarization profile, then it necessarily has a large phase gradient between orthogonal polarization components across its wave front. This is intuitive when one considers that the SLM creates a non-uniform polarization by imparting a non-uniform phase to one of the light field's polarization components. For mathematical considerations, consider a light field in the plane wave approximation with propagation along $\hat{z}$ and a transversely varying phase $\Theta(x, y)$ between $|H\rangle$ (i.e. $\hat{x}$) and $|V\rangle$ (i.e. $\hat{y}$),

$$\vec{E}(x, y, z, t) = \frac{1}{\sqrt{2}} e^{i(k_x x + k_y y + k_z z - \omega t)} (\hat{x} + e^{i\Theta(x,y)} \hat{y}). \tag{3.2}$$

If $\Theta(x, y)$ is constant across the wave front, then Eq. (3.2) describes a uniform polarization – the relative phase $\Theta(x, y)$ has a spatial gradient of zero. If, however, the relative phase is not constant across the wave front, then Eq. (3.2) describes a non-uniform polarization – the relative phase $\Theta(x, y)$ will have a non-zero spatial gradient. To see this, assume that $\Theta(x, y) = k'_x x + k'_y y$, where k'_x, k'_y are constants of propagation. The transverse relative phase gradient $\nabla_\perp \Theta(x, y) = \left(\frac{\partial}{\partial x} \hat{x} + \frac{\partial}{\partial y} \hat{y} \right) \Theta(x, y)$ is given by,

$$\nabla_\perp \Theta(x, y) = k'_x \hat{x} + k'_y \hat{y} = \vec{k}_\perp. \tag{3.3}$$

Thus, a large transverse phase gradient implies a large transverse component in momentum space. This implies the wave front normal vectors do not make small angles with the propagation direction and can therefore not propagate without loss to divergence [23].

In order to retain as much light as possible, a *4f focusing system* is positioned after each phase modulation. Such systems are composed of two lenses of focal lengths f_1 (the *objective* lens) and f_2 (the *collector* lens), positioned a distance $f_1 + f_2$ apart. The object plane is at a distance f_1 away from the objective lens (on the side opposite the collector) and the image plane is at a distance f_2 away from the collector lens (on the side opposite the objective).

This arrangement *images* nearly all of the information in a light field from the object plane to the image plane, as shown in Fig. 3.2. While imaging can be performed with a single lens, one must bear in mind the Fourier transforming property of lenses, namely that the image plane of a

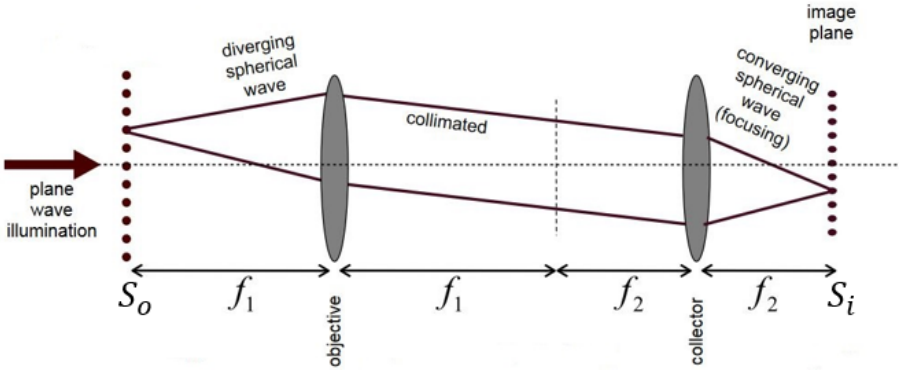

Figure 3.2: General 4f imaging system (modified from [36])

lens is also the Fourier plane of the lens*. For a concrete example, one can consider a plane wave description of a light field as in Eq. (3.2) incident on a lens of focal length f. If the lens is centred at $z = 0$, the time-independent image of the light field formed by this single lens is given by,

$$\vec{E}\left(k_x, k_y, f\right) = \mathcal{F}\left(\vec{E}\left(x, y, -f\right)\right), \tag{3.4}$$

where

$$\mathcal{F}\left(\vec{E}\left(x, y, -f\right)\right) = \int_{-\infty}^{\infty}\int_{-\infty}^{\infty} \vec{E}\left(x, y, -f, t\right) e^{i\left(k_x x + k_y y\right)} dx dy. \tag{3.5}$$

In this experiment, it is undesirable to change the wavefunction of the light field since one is only interested in modifying the polarization at specific points in the initial light field. In order to retain the information of the initial light field, the Fourier transform must be *un-done*, so to speak. For absolutely integrable, continuous functions $f(\xi)$†, the Fourier transform has the property that,

$$f\left(-\xi\right) = \mathcal{F}\left(\mathcal{F}\left(f\left(\xi\right)\right)\right). \tag{3.6}$$

For optics, the above considerations indicate that two lenses composing a 4f system can successfully produce a two-dimensional inverted image of the original light field at a distance of 4f away – hence its name. The setup shown in Fig. 3.1 employs two such systems. The first 4f system images the modulated light field from the first incidence on the SLM onto the position of the light field at the second incidence on the SLM, though the image from the first incidence will be flipped about the horizontal with respect to the second incidence. This flip can be accounted for (and is explained in Section 3.3.1) such that the SLM can predictably operate on the appropriate regions of the light field for a second time. The second 4f system images the resulting light field at the second incidence of the SLM onto the CCD camera for analysis. The focal lengths of the lenses are all 100 mm, so the placement of all the setup components is very specific to ensure that proper imaging occurs as described above.

*For clarity, the image plane of a single lens is one focal length away from the lens on the side opposite the object, provided the object is also one focal length away.

†This condition poses little trouble for conventional optics, as lasers have a Gaussian wavefunction. This wavefunction is continuous and absolutely integrable.

3.1.3 Implementing Stokes Polarimetry

The projectors of Eq. (2.27) are realized by a QWP, HWP, and PBS. The waveplates are placed on motorized stages as in Fig. 3.3 and interfaced with LabView so that the procedure of creating the projections can be fully automated. The PBS is necessary for normalization, as without a polarization-sensitive device, the measured intensity at each pixel of the CCD would be constant for each projection. The relative waveplate orientations used to perform the appropriate projections are given in Table 3.5.

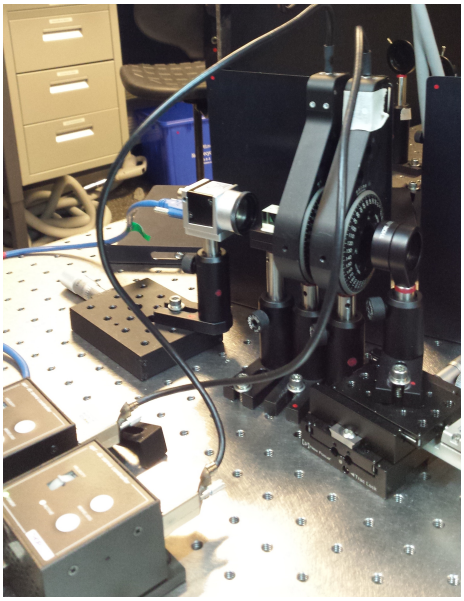

Figure 3.3: The motorized QWP, HWP, and PBS required for Stokes polarimetry.

Projector	HWP Angle (°)	QWP Angle (°)
$\hat{P}_{\|H\rangle}$	0	0
$\hat{P}_{\|V\rangle}$	45	0
$\hat{P}_{\|A\rangle}$	-22.5	45
$\hat{P}_{\|D\rangle}$	22.5	45
$\hat{P}_{\|R\rangle}$	0	45
$\hat{P}_{\|L\rangle}$	45	45

Table 3.5: Waveplate settings for Stokes Polarimetry. Note: 0° has been defined as 326.473° and 5.435° for the HWP and QWP, respectively.

3.1.4 Interference Fringes

One problem that was observed early on in the experiment was the presence of *polarization fringes* across the wave front: discrete regions with distinct polarizations appearing in sparse periodicity (see Fig. 3.4). This effect was observed even when the SLM was programmed to impart a uniform phase, and was therefore largely unexpected. The presence of these fringes were attributed to two kinds of Fabry-Perot effects that occur when working with reflective SLMs similar to the one used in this experiment [37].

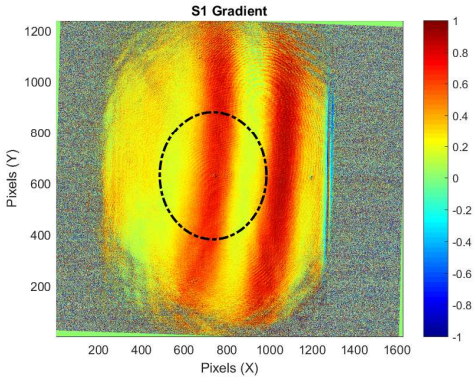

(a) Colourmap of s_1 component

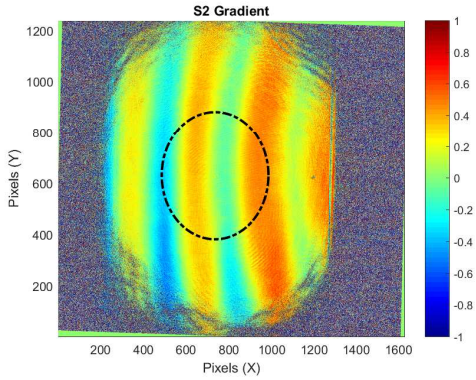

(b) Colourmap of s_2 component

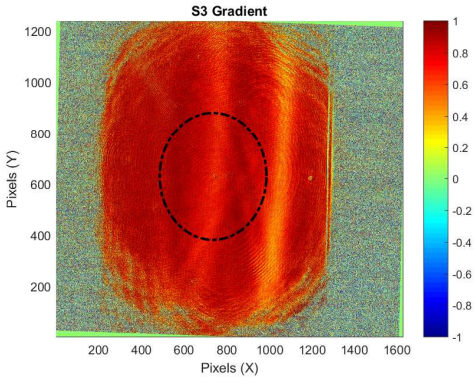

(c) Colourmap of s_3 component

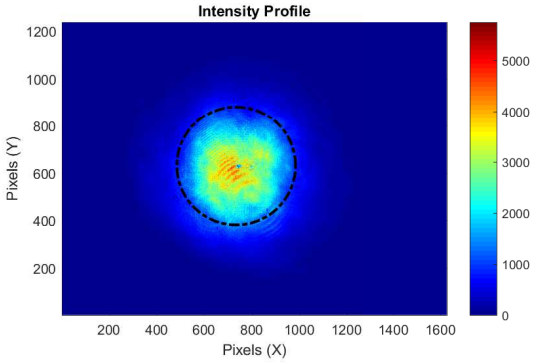

(d) Colourmap of intensity

Figure 3.4: Tomographic results that show the interference fringes. One can see that the fringes only occur in polarization, not intensity. The black dotted light indicates the $1/e^2$ beam waist.

These Fabry-Perot effects are a result of the SLM's design. The construction of the SLM involves a display window that is composed of several layers of material, i.e. a *dielectric stack*, usually consisting of a liquid crystal layer, a protective glass layer, and potentially another phase-compensating dielectric layer in front of a curved complementary metal oxide semiconductor (CMOS) backplane. A non-negligible amount of light can undesirably reflect between the layers of the stack before reaching the silicon back plane such that interference can occur among the

ordinary and extraordinary rays, as well interference from each ray with itself[‡]. Moreover, the setup itself realizes several cavities, especially between the NPBS and the SLM window, which can give rise to additional interference or additional (and unintended) phase modulations. Two

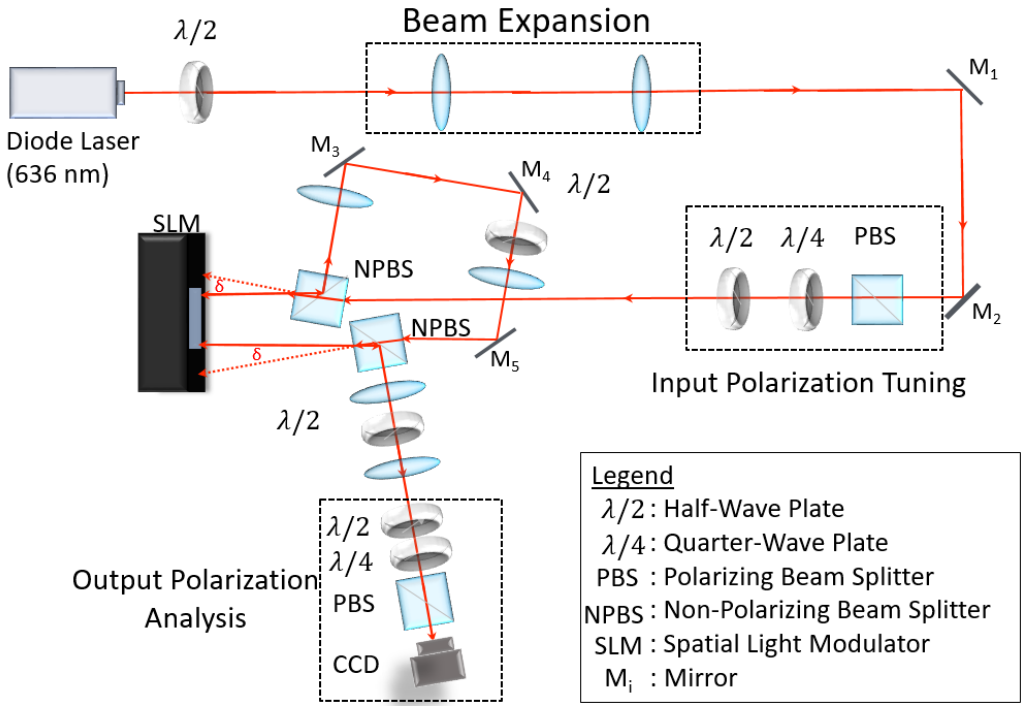

Figure 3.5: The NPBS are rotated by a small angle δ so that the light reflected from the face of the NPBS nearest the SLM misses the active SLM window.

strategies were employed to combat these problems. The first was to rotate each NPBS in front of the SLM window by a small angle δ, as shown in Fig. 3.5. This tilt forced any reflected light from the face of the NPBS to be directed away from the SLM window. This required each component in the setup to be correspondingly rotated. The second strategy to combat interference was to operate the diode laser at a lower bias current; recall that one condition for interference to occur is that the light must have a sufficiently long coherence time [28]. This quantity can be converted into a coherence length through regular kinematics, and is interpreted as the maximum distance over which a wave can exhibit some specified degree of coherence. For an optical source of Gaussian spectral distribution, the coherence length L_c, defined as when the visibility of interference reaches 50%, can be expressed in terms of the centre wavelength λ_0 and -3 dB linewidth $\Delta\lambda$ as [39],

$$L_c = \sqrt{\frac{2\ln 2}{\pi}}\frac{\lambda_0^2}{\Delta\lambda}. \tag{3.7}$$

According to Eq. (3.7), as the linewidth of the source increases, the coherence length decreases.

[‡]This interference has been studied elsewhere and characterized by a finesse parameter in a simplified model of a single LC layer with reflections on either side [38].

To reduce the linewidth of a laser diode, the laser diode can be operated with a bias current that is below the threshold current. This will produce light from spontaneous emission and therefore the light will have a broader spectrum. Thus, in an attempt to mitigate the interference, the bias current was set to a value of 20 mA (the minimum bias current – well below the threshold value of 70 mA). The spectrum of the output for this bias current was measured by an Ando AQ6315 spectrum analyzer and is shown in Fig. 3.6 and indicates a -3 dB linewidth of approximately 13.2 nm (or roughly 5.6 THz), which corresponds to a coherence length of $20\mu m$ by Eq. (3.7). The linewidth of the laser when operating at a bias current of 70 mA is shown in Fig. 3.7 and is roughly 0.09 nm, which corresponds to a coherence length of 3 mm. Operating the laser at this setting and rotating the NPBS was sufficient in getting rid of the fringes observed in Fig. 3.4.

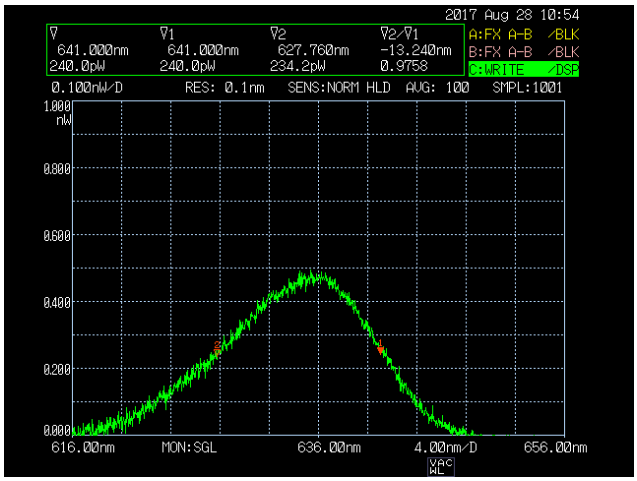

Figure 3.6: The laser linewidth measured at a bias current of 20 mA.

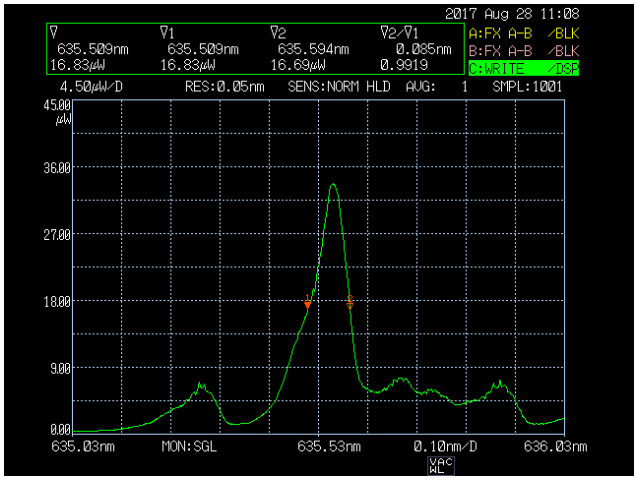

Figure 3.7: The laser linewidth measured at a bias current of 70 mA.

3.2 SLM Calibration

3.2.1 Pixel-by-Pixel Phase-Gray Determination

The SLM has been designed and manufactured such that it can be treated as a traditional monitor that interfaces with a computer. The amount of phase that the SLM imparts at a given pixel is directly proportional to the 8 bit grayscale value at that given pixel. Thus, intricate phase patterns are imparted by placing intricate grayscale patterns on the SLM, which is accomplished in the same manner as placing a particular background image on computer. The exact amount of phase that a given level of grayscale imparts is nominally given by the manufacturer as a linear function,

$$\phi_{ij}(g_{ij}) = C g_{ij}, \tag{3.8}$$

where $g_{ij} \in [0, 255]$ is the grayscale value at pixel (i, j) and $C = \frac{2\pi}{118}$ is the nominal phase-gray proportionality constant provided by the manufacturer. However, the value of C is not distinct for each pixel of interest, and testing has proven it should be (see Fig. 3.8). To accurately program the SLM, an independent calibration of each illuminated pixel was carried out. This was accomplished by measuring the change in polarization of each discrete region i, j of an incident light field for a given change in grayscale of every pixel i', j' on the SLM for many different trials. Plots of total phase versus change in grayscale were then made and a look-up table (LUT) was stored in memory to model this phase-gray relationship exactly. Since there are two incidences on the

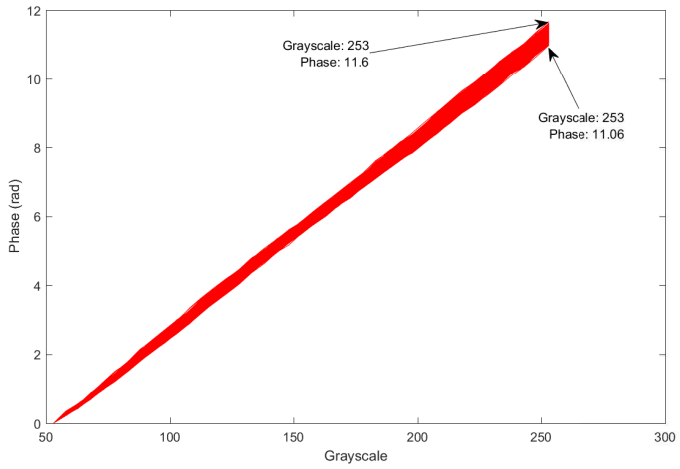

Figure 3.8: The phase-gray relationship is plotted for 10^4 pixels across the wave front. The phase-gray relationships deviate significantly from pixel to pixel, and this deviation increases with grayscale. A maximum phase discrepancy between individual pixels (within the FWTM beam waist) for the same grayscale value of 0.54 rad was measured.

SLM, two separate calibration runs were carried out. Performing the calibration of either side independently is not necessary, but is useful in what it reveals about the setup: *the axes of rotation* $\hat{k}_{ij}$ *can be determined for all pixels illuminated by the second incidence when* $\vec{S}_i = |H\rangle$. This is possible

because the optic axis of the SLM is aligned with the horizontal, so if only $|H\rangle$ or $|V\rangle$ is incident on the SLM for the first phase modulation, there will be no effect for the first phase modulation. Only after transmission through the intermediate half wave plate can the SLM have any effect on the polarization state. Knowing these axes of rotations is not only useful for verification of expected behaviour, but also serves to quantify errors, as explained in Section 5.3.

3.2.2 Pixel-by-Pixel Phase Calibration

Once the phase-gray relationship for each pixel was determined, a phase calibration for the entire setup is required. A phase calibration is defined as some grayscale pattern that is placed on the SLM such that any input polarization $\vec{S}_i$ sent into the setup will also be measured at the output of the setup. This is necessary since each optical element can, in general, modify the polarization state of any incident light field upon reflection provided that the field is not perfectly aligned with the plane of incidence (or perpendicular to it) [28] – two cases which will virtually never exist within the setup. In particular, any reflective elements in the setup (mirrors, NPBS, etc.) can alter any polarization state that is not $|H\rangle$ or $|V\rangle$ by Eq. (2.20). Additionally, while the phase-gray relationship for each pixel can be completely determined, it is completely determined *only up to a reference phase*. In other words, even if a grayscale of zero is placed at each pixel of the SLM, some minute phase is still imparted at each pixel, and this phase is not necessarily the same for each pixel. So, mathematically, the experimental setup performs an unavoidable default transformation $\hat{A}$ such that,

$$\vec{S}_o = \hat{A}_{ij}\vec{S}_i. \tag{3.9}$$

A pixel-by-pixel phase calibration is the grayscale pattern that realizes the inverse transformation $\hat{A}_{ij}^{-1}$, which is guaranteed to exist since the $\hat{A}_{ij}$ performed by the optical elements in the setup are merely phases between $|H\rangle$ and $|V\rangle$ – precisely the phases the SLM imparts. This inverse transformation $\hat{A}_{ij}^{-1}$ is defined such that,

$$\vec{S}_o = \hat{A}_{ij}\hat{A}_{ij}^{-1}\vec{S}_i = S_i. \tag{3.10}$$

In order to obtain $\hat{A}_{ij}^{-1}$, an input state $\vec{S}_i = |D\rangle$ is used and the output polarization at each pixel is measured, i.e. each pixel is assigned a Stokes vector $\vec{S}_o$. Once these Stokes vectors are assigned, the angular displacement from the initial polarization state is calculated and is decomposed into two components:

1. A rotation about S_1,
2. A rotation about S_2,

Essentially, the first rotation describes all undesired phases that occur before the intermediate HWP and after the first incidence on the SLM (but including the first incidence on the SLM), since these can only rotate the polarization about S_1. This can be compensated for by placing grayscale values on the pixels illuminated by the first incidence on the SLM. Mathematically, it is very similar to Eq. (2.14), i.e. the formula for ζ_1,

$$\zeta_1^{\text{cal}} = 2\pi - \zeta_1. \tag{3.11}$$

The second rotation describes all undesired phases that occur after the intermediate HWP and before the second incidence on the SLM (but including the second incidence on the SLM), since these effectively rotate the polarization about S_2. This can be compensated for by placing a grayscale value on the pixels illuminated by the second incidence on the SLM. Mathematically, it is very similar to Eq. (2.15), i.e. the formula for ζ_2 with $\vec{S}_m = \vec{S}^{rot}$, where $\vec{S}^{rot} = \text{SLM}\left(\zeta_1^{\text{cal}}\right)\vec{S}_i$ and can be calculated *a priori* by the Rodrigues' rotation formula [40],

$$\vec{S}^{rot} = \vec{S}_i \cos\left(\zeta_1^{\text{cal}}\right) + \left(S_1 \times \vec{S}_i\right) \sin\left(\zeta_1^{\text{cal}}\right) + S_1(S_1 \cdot \vec{S}_i)\left(1 - \cos\left(\zeta_1^{\text{cal}}\right)\right) S_1. \tag{3.12}$$

Then,

$$\zeta_2^{\text{cal}} = 2\pi - \zeta_2, \tag{3.13}$$

where it is understood that this formula applies to each pixel i, j.

These formulae can be interpreted as simply reversing the undesired, orthogonal rotations that occurred before and after the intermediate HWP. This is reasonable because all transformations in the setup can be described by rotations $\hat{R}\left(\zeta, \hat{k}\right)$, and rotations have the property,

$$\left(\hat{R}\left(\zeta, \hat{k}\right)\right)^{-1} = -\hat{R}\left(\zeta, \hat{k}\right) = \hat{R}\left(2\pi - \zeta, \hat{k}\right). \tag{3.14}$$

Finally, the phases ζ_1^{cal} and ζ_2^{cal} can be translated into grayscale values for the pixels illuminated by the first and second incidence, respectively, by using the phase-gray LUTs. This results in a *grayscale calibration image* as shown in Fig. 3.9. This grayscale image must be added on top of any nominal grayscale pattern that is used to produce a desired transformation $\hat{T}_{\vec{S}_i \to \vec{S}_o}$ (modulo 2π) so that the effect of $\hat{A}_{ij}$ is nullified as per Eq. (3.10).

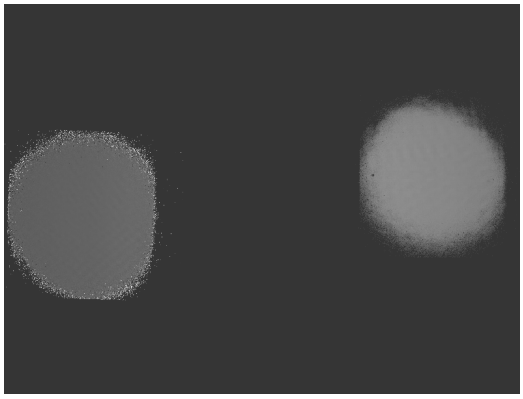

Figure 3.9: The grayscale calibration image implementing $\hat{A}_{ij}^{-1}$.

3.3 Image Processing

3.3.1 CCD-SLM Pixel Mapping

A mapping must exist between the pixels illuminated by the light field on each of the two separate incidences of the SLM, (i_1^{SLM}, j_1^{SLM}) and (i_2^{SLM}, j_2^{SLM}), and the pixels of the CCD camera, (i^{CCD}, j^{CCD}), since one must be able to program particular SLM pixels to modify particular regions of the light field for a particular transformation. These particular regions are defined by the CCD pixels detecting them (previously, (i^{CCD}, j^{CCD}) was denoted by (i', j')). When constructing this mapping, one must be diligent in appropriately accounting for the following:

1. There is a mismatch between pixel dimensions and pixel number among the SLM and CCD camera – the mapping is not bijective,
2. The pixel labels (i^{SLM}, j^{SLM}) and (i^{CCD}, j^{CCD}) are both indexed starting from $(1, 1)$, but it is not true that $(1^{SLM}, 1^{SLM})$ modifies the polarization detected at $(1^{CCD}, 1^{CCD})$ – there is a need for fiducial information,
3. There are image flips (inversions) between incidences on the SLM that were described in Section 3.1.2,
4. There could be a rotation of the image between incidences on the SLM and the CCD camera.

To address the first point of pixel mismatch, the one-to-many mapping between the pixels of the CCD camera and SLM was assumed to be linear with offset indices,

$$(j^{SLM} - j_0^{SLM}) = \lfloor m_j \left(j^{CCD} - j_0^{CCD} \right) \rfloor, \tag{3.15a}$$

$$(i^{SLM} - i_0^{SLM}) = \lfloor m_i \left(i^{CCD} - i_0^{CCD} \right) \rfloor. \tag{3.15b}$$

Here, (i_0^{SLM}, j_0^{SLM}) and (i_0^{CCD}, j_0^{CCD}) denote fiducial pixels on the SLM and CCD camera, respectively, which are pixels that have the same index. The quantities $m_i < 1$ and $m_j < 1$ are constants to be determined which account for the mismatch in pixel size along the rows and columns, respectively. These constants are less than unity since the CCD camera pixels are much smaller than the SLM pixels in both dimension and number. Rounding, in this case by way of the floor function $\lfloor \rfloor$, is required to ensure valid, integer pixel assignments. Since there are two incidences on the SLM, it is more appropriate to define two functionally identical sets of linear equations, each distinguished by subscripts which indicate either the first (1) or second (2) incidence. The mapping for the first incidence is given by Eq. (3.15), and the mapping for the second incidence is given by,

$$(j_2^{SLM} - j_{2,0}^{SLM}) = \lfloor m_j \left(j^{CCD} - j_{2,0}^{CCD} \right) \rfloor, \tag{3.16a}$$

$$(i_2^{SLM} - i_{2,0}^{SLM}) = \lfloor m_i \left(i^{CCD} - i_{2,0}^{CCD} \right) \rfloor. \tag{3.16b}$$

To address the third point of image flips, one simply needs to *flip* the mapping for the second incidence pixels about the vertical. Mathematically, this translates to negation of Eq. (3.16a). Lastly, an image rotation about the propagation axis is possible if a geometric phase ensues from the light field coming out of the plane of incidence due to small misalignments in the setup. This effect has

been noticed between the incidences on the SLM and also explains why the grayscale calibration image of Fig. 3.9 has the grayscale image on the left lower than the grayscale image on the right. If the angle of rotation is θ, this can be rectified by rotating the pixel maps for the second incidence by an angle θ through the use of a standard rotation matrix. Thus, the final equations constituting the pixel map for the second incidence is, in matrix form,

$$\begin{bmatrix} i_2^{SLM} - i_{2,0}^{SLM} \\ j_2^{SLM} - j_{2,0}^{SLM} \end{bmatrix} = \begin{bmatrix} \cos\theta & -\sin\theta \\ \sin\theta & \cos\theta \end{bmatrix} \begin{bmatrix} \lfloor m_i \left(i^{CCD} - i_{2,0}^{CCD} \right) \rfloor \\ \lfloor -m_j \left(j^{CCD} - j_{2,0}^{CCD} \right) \rfloor \end{bmatrix}, \tag{3.17}$$

and the final equation constituting the pixel map for the first incidence is, in matrix form,

$$\begin{bmatrix} i_1^{SLM} - i_{1,0}^{SLM} \\ j_1^{SLM} - j_{1,0}^{SLM} \end{bmatrix} = \begin{bmatrix} \lfloor m_i \left(i^{CCD} - i_{1,0}^{CCD} \right) \rfloor \\ \lfloor m_j \left(j^{CCD} - j_{1,0}^{CCD} \right) \rfloor \end{bmatrix}. \tag{3.18}$$

The values m_i and m_j were determined experimentally through Fourier analysis; in Fig. 3.10a, one

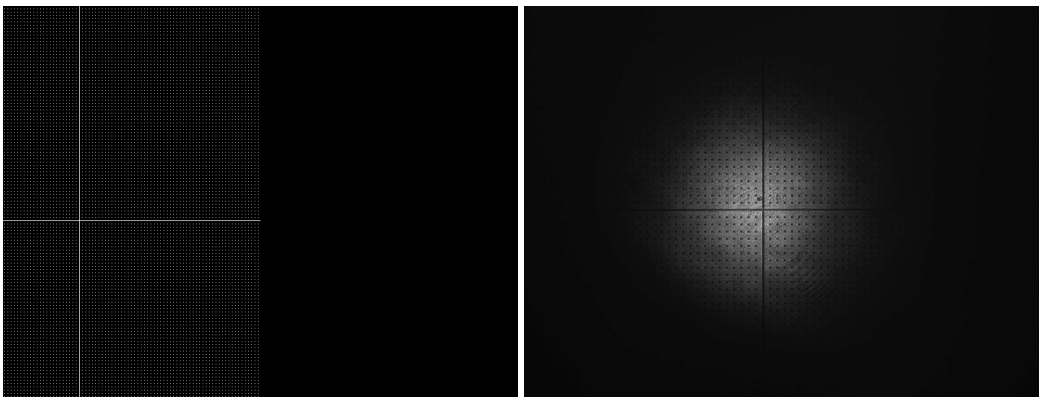

(a) Fiducial image placed on the SLM. (b) Imaged light field on the CCD camera.

can see a periodic grayscale image placed on the SLM and the resulting periodic intensity image captured by the CCD camera is in Fig. 3.10b. Let the imaged intensity distribution be given by $f_{i^{CCD} j^{CCD}}$. Let the modulated pixel frequency along the rows and columns of this image be given by ω_i^{CCD} and ω_j^{CCD}, respectively. Let the modulated pixel frequency along the rows and columns for the grayscale image be given by ω_i^{SLM} and ω_j^{SLM}, respectively. Then,

$$m_i = \frac{\omega_i^{SLM}}{\omega_i^{CCD}}, \tag{3.19a}$$

$$m_j = \frac{\omega_j^{SLM}}{\omega_j^{CCD}}. \tag{3.19b}$$

The periodicities ω_i^{CCD} and ω_j^{CCD} can be determined by calculating the discrete Fourier transform

of f_{ij},

$$F_{IJ} = \frac{1}{mn} \sum_{i=0}^{m} \sum_{j=0}^{n} f_{ij} e^{-2\pi\iota(\frac{iI}{m} + \frac{jJ}{n})}, \tag{3.20}$$

where m and n are the number of rows and columns of CCD camera pixels, respectively, and ι is the imaginary unit. The rows and columns are mapped to the Fourier domain in accordance with the Nyquist frequency,

$$I = [-\frac{1}{2}\nu, \frac{1}{2}\nu], \tag{3.21}$$

$$J = [-\frac{1}{2}\nu, \frac{1}{2}\nu], \tag{3.22}$$

where $\nu = 1$ is the pixel sampling rate and $||I|| = m$, $||J|| = n$. The coordinates of the highest peak in F_{IJ} should correspond to $(\omega_i^{CCD}, \omega_j^{CCD})$, which were found to be (0.0530, 0.0526). Thus, by Eq. (3.19), $m_i = 0.209$ and $m_j = 0.208$. If one were to perform a more simple calculation by simply dividing the pixel dimensions by one another, one would find $m_i = m_j = 0.22$, which has a percent difference of 5.5% with the experimentally determined results.

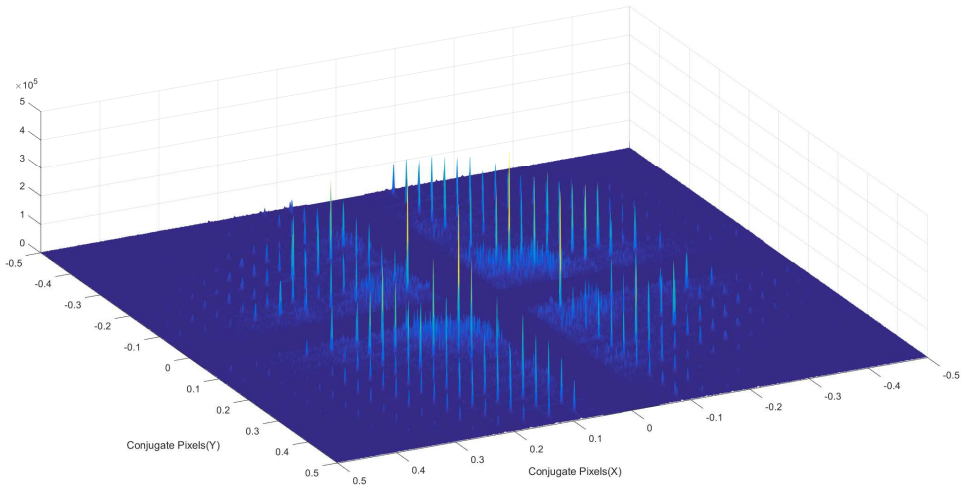

Figure 3.11: F_{ij}, as plotted in the frequency domain. Low frequency components were manually filtered out. The four central peaks of interest are seen with red tips.

Chapter 4

Experimental Results

Two metrics are used to quantify the success of a polarization transformation and are computed from $\vec{S}_o$. The first is quantum purity, P, which is defined by Eq. (2.8) and measures how uniform a light field's polarization is. The second is state fidelity, $0 \leq F \leq 1$, which is a measure of how similar two quantum states $\hat{\rho}$ and $\hat{\rho}'$ are. It is useful for comparing experimental results with theoretical results and is defined by,

$$F = \mathrm{Tr}\left(\sqrt{\sqrt{\hat{\rho}'}\hat{\rho}\sqrt{\hat{\rho}'}}\right). \tag{4.1}$$

Indistinguishable states have $F = 1$ and orthogonal states have $F = 0$. An average over all Stokes vectors $\vec{S}_{ij}$ within the FWTM beam waist (denoted by a dotted black line in the figures containing Stokes component colourmaps) of the output state is taken to assign a Stokes vector for the entire light field. Finally, $\hat{\rho}$ is recovered with an application of Eq. (2.5) to compute the fidelity and purity.

Before any polarization transformation was performed, a benchmark of the tomography's accuracy was made. To do this, one measured the polarization state resulting from placing a PBS and HWP oriented at 22.5° in the path of a light field. Here, one expects to measure a *near-perfect* $|D\rangle$. It was found that $|D\rangle$ was measured with a fidelity of 0.999 and a quantum purity of 0.995. These results are shown in Fig. 4.1. When the uncalibrated setup is used as intended, i.e. without the PBS as per Fig. 3.1, the resulting output polarization does not have a good fidelity with the input state nor a high purity, hence the need for the aforementioned phase calibration as explained in Section 3.2.2. As a specific example, when no grayscale calibration pattern is placed on the SLM, the output polarization for an input polarization $\vec{S}_i = |D\rangle$ results in a fidelity of 0.728 and a purity of 0.946 – a clear indication that an appropriate calibration is required. The setup calibration was constructed as per Section 3.2.2 and tested by placing the grayscale calibration image on the SLM (as shown in Fig. (3.9)) and measuring the resulting output polarization state $\vec{S}_o$ for various input polarization states $\vec{S}_i$. These results are summarized in Table 4.1.

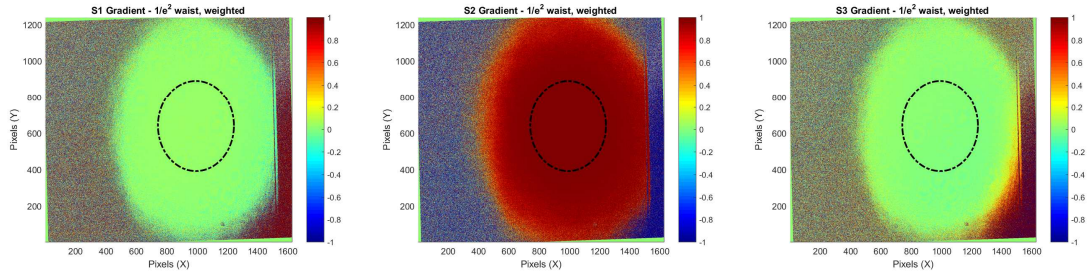

(a) Colourmap of s_1. (b) Colourmap of s_2. (c) Colourmap of s_3.

Figure 4.1: The Stokes components for a light field corresponding to a near-perfect $|D\rangle$.

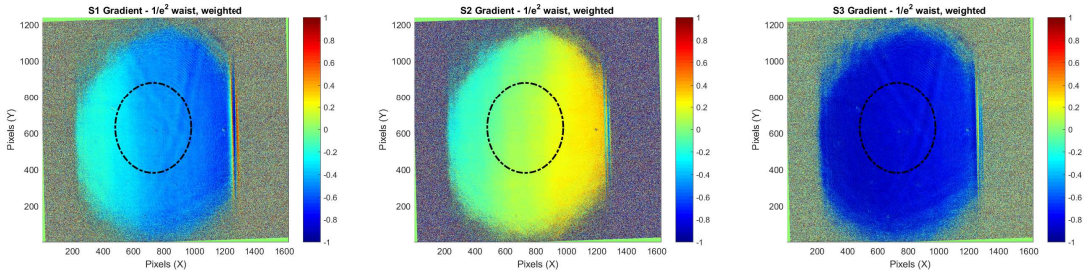

(a) Colourmap of s_1. (b) Colourmap of s_2. (c) Colourmap of s_3.

Figure 4.2: The Stokes components for a $|D\rangle$-polarized light field after an uncalibrated setup. Ideally, a) is uniform and green, b) is uniform and red, and c) is uniform and green.

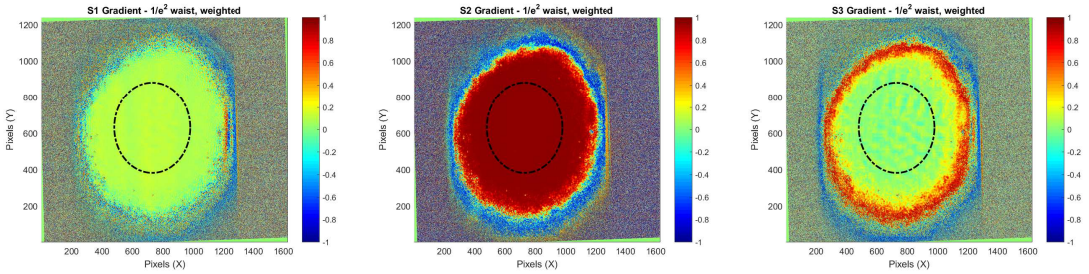

(a) Colourmap of s_1. (b) Colourmap of s_2. (c) Colourmap of s_3.

Figure 4.3: The Stokes components for a $|D\rangle$-polarized light field after a calibrated setup.

Input State	Output State	Fidelity	Purity
[1 0 0]	[0.793 0.008 0.325]	0.947	0.868
[0 1 0]	[0.098 0.953 0.064]	0.988	0.961

Table 4.1: Baseline measurements of state fidelity and quantum purity for a calibrated system.

4.1 Uniform to Uniform Transformations

After benchmarking the calibrated setup's performance, some uniform to uniform transformations were made. An important preliminary result should show that the experimental setup is capable of mapping a uniform input polarization to any arbitrary uniform output polarization, much like a HWP and QWP in sequence. In order to demonstrate that *any* output polarization state can be reached, a set of four output states forming a SIC-POVM was selected to map to. The simplest definition of a SIC-POVM includes any set of d^2 normalized vectors $|\phi_k\rangle \in \mathbb{C}^d$ satisfying [34],

$$\left|\langle\phi_k|\phi_j\rangle\right|^2 = \frac{1}{d+1}, \qquad k \neq j. \tag{4.2}$$

For $d = 2$, these states form a tetrahedron within the Poincaré sphere if the vector tips are connected together as shown in Fig. 4.4. Since these sets are known to be optimal for performing quantum state tomography [34], one reasons that if these SIC-POVM states can be produced by the experimental setup from some $\vec{S}_i \in \vec{S}'$, then any arbitrary polarization state can be produced for an input $\vec{S}_i = |D\rangle \in \vec{S}'$. The result of each mapping is given in Table 4.2. These results indi-

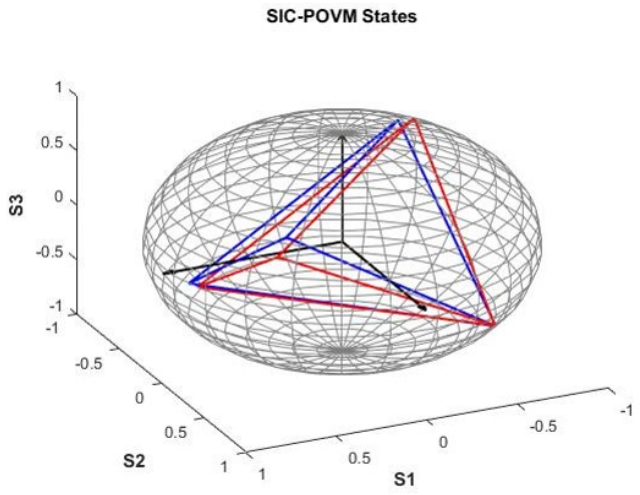

Figure 4.4: The SIC-POVM states form a tetrahedron in the Poincaré sphere. The blue and red vertices represent the theoretical and experimental SIC-POVM states, respectively.

Theory	$\frac{1}{\sqrt{3}}[1,1,1]$	$\frac{1}{\sqrt{3}}[1,-1,-1]$	$\frac{1}{\sqrt{3}}[-1,1,-1]$	$\frac{1}{\sqrt{3}}[-1,-1,1]$
Expt.	$[0.50, 0.69, 0.49]$	$[0.58, -0.61, -0.40]$	$[-0.43, 0.59, -0.46]$	$[-0.54, -0.41, 0.56]$
Purity	0.98	0.93	0.88	0.89
Fidelity	0.99	0.98	0.97	0.97

Table 4.2: Uniform to Uniform Transformations. Note: $\frac{1}{\sqrt{3}} = 0.58$

cate that the setup can map $\vec{S}_i = |D\rangle$ to a uniform, arbitrary state. Quantitatively, it does so with

fidelities and purities that are on par with the calibration benchmarks of Table 4.1. For a graphical representation of each tetrahedral state, colourmaps of individual Stokes components are given in Fig. 4.5 - Fig. 4.8. An example of a grayscale image used to perform one of these transformations is given in Fig. 4.9.

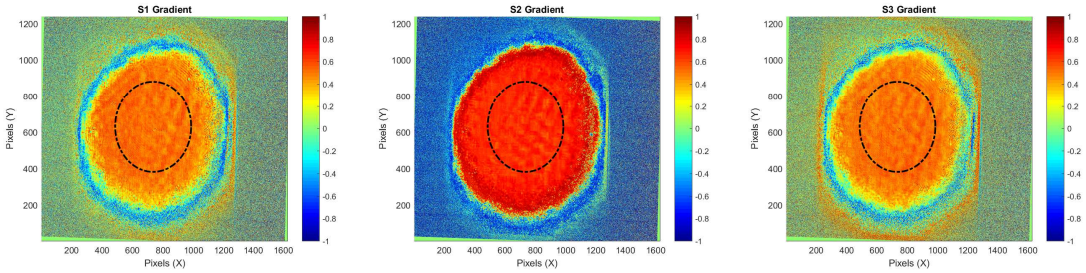

(a) Colourmap of s_1. (b) Colourmap of s_2. (c) Colourmap of s_3.

Figure 4.5: Stokes components plotted in colourmaps for $\vec{S} = \frac{1}{\sqrt{3}}[1, 1, 1]$.

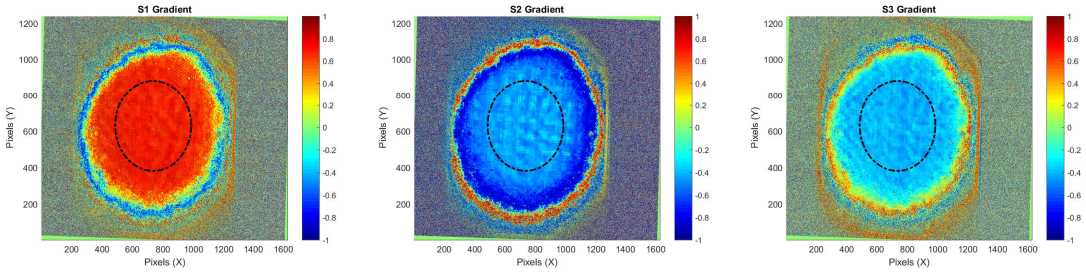

(a) Colourmap of s_1. (b) Colourmap of s_2. (c) Colourmap of s_3.

Figure 4.6: Stokes components plotted in colourmaps for $\vec{S} = \frac{1}{\sqrt{3}}[1, -1, -1]$.

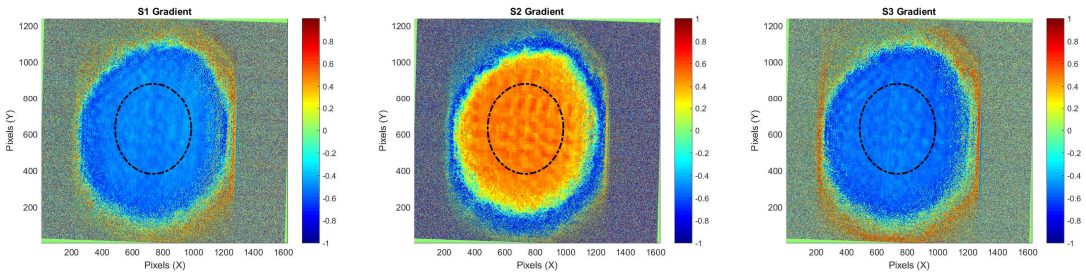

(a) Colourmap of s_1. (b) Colourmap of s_2. (c) Colourmap of s_3.

Figure 4.7: Stokes components plotted in colourmaps for $\vec{S} = \frac{1}{\sqrt{3}}[-1, 1, -1]$.

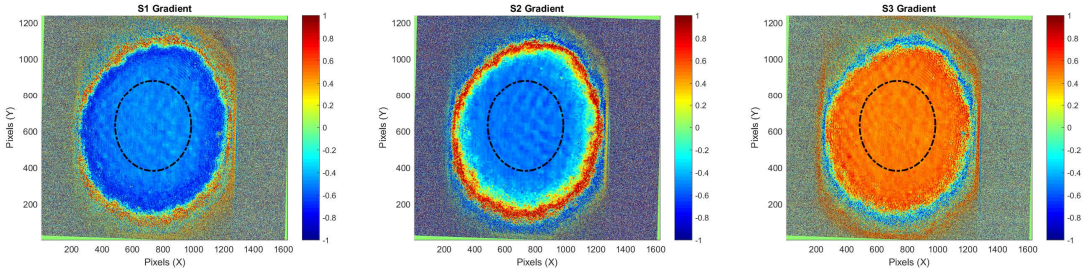

(a) Colourmap of s_1. (b) Colourmap of s_2. (c) Colourmap of s_3.

Figure 4.8: Stokes components plotted in colourmaps for $\vec{S} = \frac{1}{\sqrt{3}}[-1, 1, -1]$.

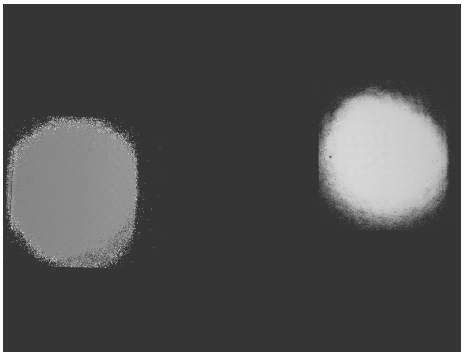

Figure 4.9: Grayscale image used to produce $\vec{S} = \frac{1}{\sqrt{3}}[1, -1, -1]$.

4.2 Uniform to Non-Uniform Transformations

The uniform-to-uniform results are important for proof-of-principle but are not overly useful since a HWP and QWP can, together, be more versatile in performing a uniform transformation. This is because the possible input states are not limited to the subset $\vec{S}'$. The primary usefulness of this setup resides in the ability to implement $\hat{T}_{\vec{S}_i \to \vec{S}_o}$ *point-by-point* across a wave front. In order to demonstrate this, the same transformations of Section 4.1 were performed 'in one shot', i.e. the SIC-POVM states were placed in the *same* wave front, organized by quadrant. Transformations of this kind are not possible with conventional optics such as waveplates, and results of this non-uniform transformation are given in Table 4.3. The grayscale image is in Fig. 4.11.

	Quadrant 1	**Quadrant 2**	**Quadrant 3**	**Quadrant 4**
Theory	$\frac{1}{\sqrt{3}}[1, 1, 1]$	$\frac{1}{\sqrt{3}}[1, -1, -1]$	$\frac{1}{\sqrt{3}}[-1, 1, -1]$	$\frac{1}{\sqrt{3}}[-1, -1, 1]$
Expt.	$[0.44, 0.70, 0.51]$	$[0.50, -0.58, -0.51]$	$[-0.53, -0.41, 0.48]$	$[-0.49, 0.43, -0.61]$
Purity	0.96	0.92	0.84	0.90
Fidelity	0.99	0.98	0.96	0.98

Table 4.3: Uniform to Non-Uniform Transformations. Note: $\frac{1}{\sqrt{3}} = 0.58$

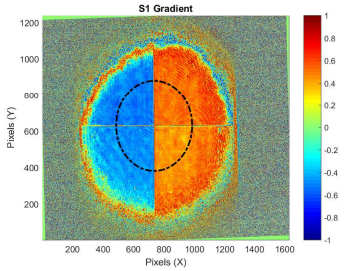

(a) Colourmap of s_1.

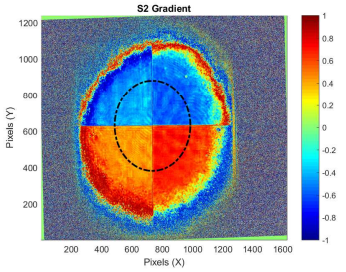

(b) Colourmap of s_2.

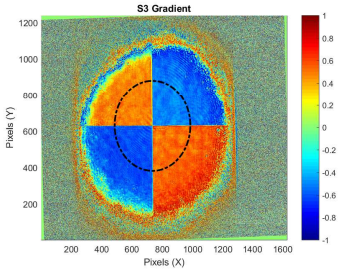

(c) Colourmap of s_3.

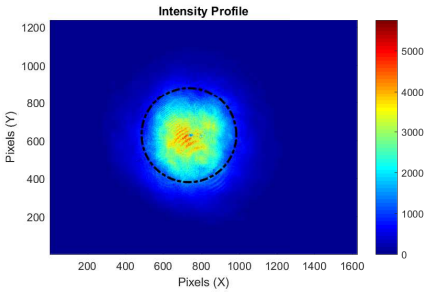

(d) Colourmap of intensity.

Figure 4.10: The Stokes components and intensity for the light field containing distinct SIC-POVM states in each quadrant.

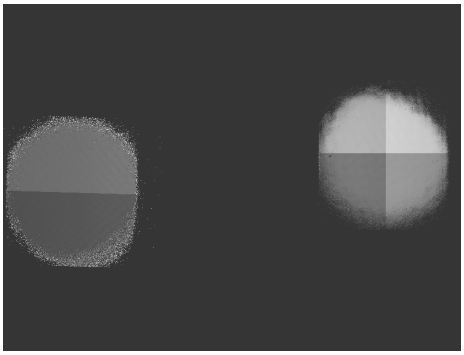

Figure 4.11: Grayscale image used to produce a light field with all SIC-POVM states.

While this non-uniform transformation successfully resulted in the desired state, only four distinct transformations were performed at once. This is a small number of transformations when one considers that each pixel of the SLM can transform light independently. One way that was conceived to exploit this was through *polarization imaging*. With this setup, full images can be en-

coded in polarization that are hidden to humans*, but can be revealed through Stokes polarimetry and the graphical methods described in Section 2.1.1.

To this end, an image of Van Gogh's *Starry Night* was encoded in polarization: Fig. 4.12 shows the original painting, where one can see many individual contours (brush strokes) creating the image. These contours were quantified by a Python script (written by Codey Nacke) and stored in an array. By using the elliptical representation of polarization, a contour can actually describe particular linear polarization states when characterized by an angle with respect to the horizontal (i.e. the principal axis of the ellipse, ψ). Since any elliptical representation can map directly to a particular Stokes vector, Eq. (2.14) - Eq. (2.16) can be used to program the SLM to create an image in polarization, as shown in Fig. 4.13. The grayscale image to do so is shown in Fig. 4.15. One may notice that some contours of Fig. 4.13 appear darker than others. This is intentional, as the darkness of each contour relates to the ellipticity of the polarization state at that particular point in the wave front by the following equation,

$$s_3^{ij} = 1 - 2\left(\frac{g_{ij}}{\max\left(g_{ij}\right)}\right), \tag{4.3}$$

where g_{ij} is the rendered grayscale level of Van Gogh's original painting at the pixel indexed by i, j.

Figure 4.12: A cropped *Starry Night* to image with polarization.

4.3 Non-Uniform to Uniform Transformations

It was demonstrated in Section 4.2 that the setup was capable of performing uniform-to-non-uniform transformations. To show more versatility of the setup, a q-plate was added after the input polarization tuning stage of Fig. 3.5 in an attempt to modify a non-uniform polarization state so that it is uniform – a non-uniform-to-uniform transformation. Here, linear (diagonal, $|D\rangle$) light was incident on an electrically unbiased q-plate of topological charge $q = -1$. This generated a non-uniform polarization profile, as explained in Section 2.3.5. When the grayscale calibration

*Humans are not capable of directly sensing polarization with the naked eye, as some other animals can [2].

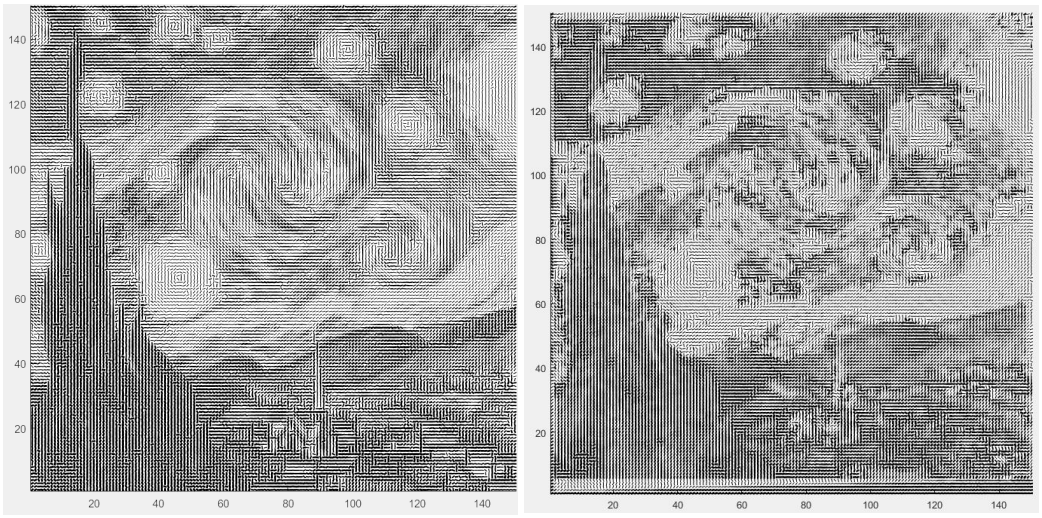

(a) Simulated rendering of *Starry Night*. (b) Experimental rendering of *Starry Night*.

Figure 4.13: *Starry Night*, painted in polarization.

image is placed on the SLM, one can measure the light field that was modified by the q-plate and incident on the SLM, as shown in Fig. 4.16a - Fig. 4.16c. This allows for a description of $\vec{S}_i$ and is the only additional step required in non-uniform-to-uniform transformations when compared to the procedure for performing any other previously described transformation. Various output states were selected to transform to, and the results of doing so are shown in Table 4.4.

	Fidelity	**Purity**
Pre-Correction	0.698	0.552
Post-Correction	0.965	0.880
Difference	**0.267**	**0.328**

Table 4.4: Non-uniform-to-uniform transformation results. The *Pre-Correction* row lists the data for the polarization state after the q-plate. The *Post-Correction* row lists the data for the polarization state after the q-plate and phase modulation with the SLM. Both fidelities are with respect to the desired output state, $\vec{S}_o = [-0.58, 0, 0.58]$.

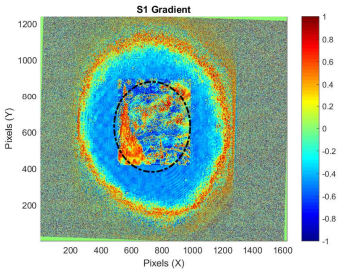

(a) Colourmap of s_1.

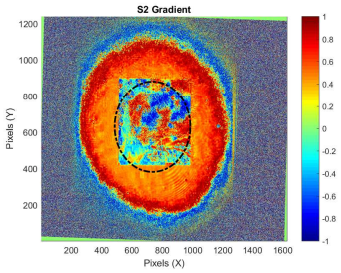

(b) Colourmap of s_2.

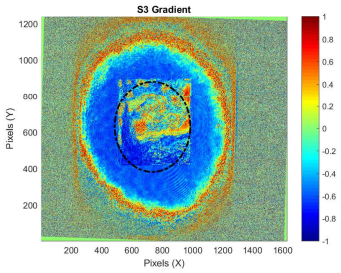

(c) Colourmap of s_3.

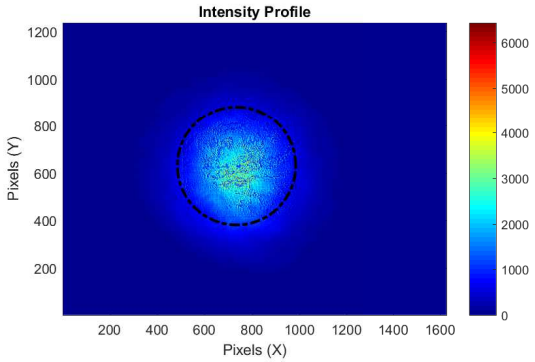

(d) Colourmap of intensity.

Figure 4.14: The Stokes components for the light field containing *Starry Night*.

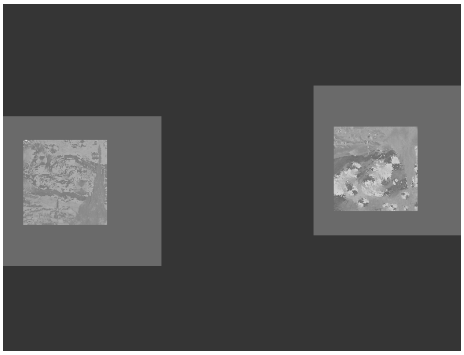

Figure 4.15: Grayscale image used to produce a light field with *Starry Night* encoded in polarization.

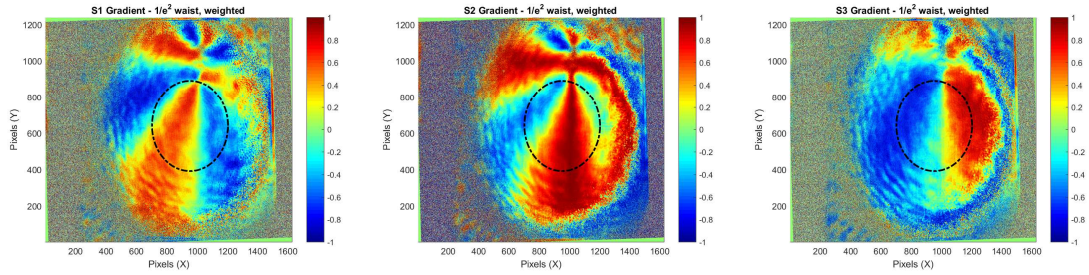

(a) Colourmap of s_1. (b) Colourmap of s_2.. (c) Colourmap of s_3.

Figure 4.16: Stokes components for the *pre-correction* light field resulting from introducing a q-plate into the setup.

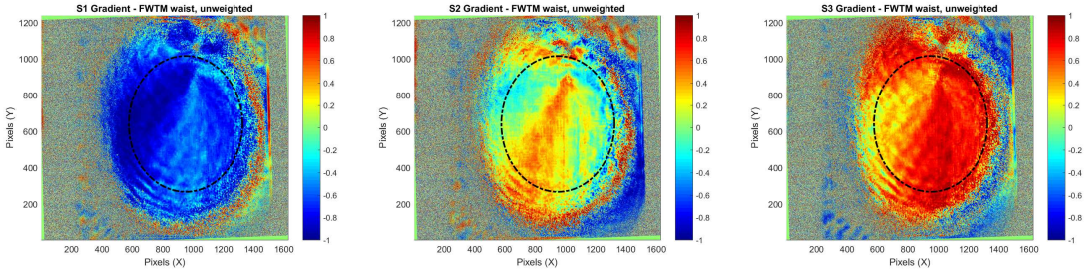

(a) Colourmap of s_1. (b) Colourmap of s_2. (c) Colourmap of s_3.

Figure 4.17: Stokes parameters for the *post-correction* light field resulting from introducing a q-plate into the setup. Ideally, a) is uniform and light blue, b) is uniform and green, c) is uniform and light red.

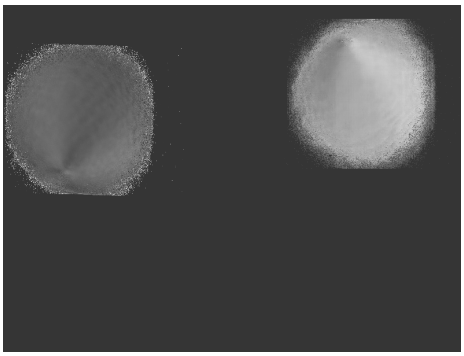

Figure 4.18: Grayscale image used to convert q-plate input to uniform output.

Chapter 5

Error Analysis

5.1 Errors in Waveplates

The Stokes Polarimetry described in Section 2.4 assumes that the projectors of Eq. (2.27) are perfect, i.e. the waveplates that implement these projectors are ideal. This is of course not the case; waveplates are seldom made without error in their retardance, and therefore any measurements with them are generally biased.

There is, however, an inversion method to compensate for waveplates with small deviations in their nominal retardance, which was written about by Altepeter *et al.* [41]. The general idea is to assume that the projection operators realized by the waveplates are imperfect in that they will project onto a state $|\psi'\rangle$ instead of a desired state $|\psi\rangle$. This results in the following Pauli-*like* operators,

$$\hat{\sigma_0}' = \hat{P}_{|H'\rangle} + \hat{P}_{|V'\rangle}, \tag{5.1a}$$

$$\hat{\sigma_1}' = \hat{P}_{|H'\rangle} - \hat{P}_{|V'\rangle}, \tag{5.1b}$$

$$\hat{\sigma_2}' = \hat{P}_{|R'\rangle} + \hat{P}_{|L'\rangle}, \tag{5.1c}$$

$$\hat{\sigma_3}' = \hat{P}_{|D'\rangle} + \hat{P}_{|A'\rangle}, \tag{5.1d}$$

which give rise to the following Stokes-*like* parameters when measured,

$$t_0 = \mathrm{Tr}\left(\hat{\sigma_0'}\hat{\rho}\right), \tag{5.2a}$$

$$t_1 = \mathrm{Tr}\left(\hat{\sigma_1'}\hat{\rho}\right), \tag{5.2b}$$

$$t_2 = \mathrm{Tr}\left(\hat{\sigma_2'}\hat{\rho}\right), \tag{5.2c}$$

$$t_3 = \mathrm{Tr}\left(\hat{\sigma_3'}\hat{\rho}\right). \tag{5.2d}$$

An application of Eq. (2.7) reveals how these can be linearly related to the true Stokes parameters,

$$t_i = \sum_{k=0}^{3} \mathrm{Tr}\left(\sigma_i'\sigma_k\right) s_k. \tag{5.3}$$

Thus, the following linear matrix equation can be written,

$$\begin{bmatrix} t_0 \\ t_1 \\ t_2 \\ t_3 \end{bmatrix} = \begin{bmatrix} \mathrm{Tr}\left(\sigma_1'\sigma_1\right) & \mathrm{Tr}\left(\sigma_1'\sigma_2\right) & \mathrm{Tr}\left(\sigma_1'\sigma_3\right) & \mathrm{Tr}\left(\sigma_1'\sigma_4\right) \\ \mathrm{Tr}\left(\sigma_2'\sigma_1\right) & \mathrm{Tr}\left(\sigma_2'\sigma_2\right) & \mathrm{Tr}\left(\sigma_2'\sigma_3\right) & \mathrm{Tr}\left(\sigma_2'\sigma_4\right) \\ \mathrm{Tr}\left(\sigma_3'\sigma_1\right) & \mathrm{Tr}\left(\sigma_3'\sigma_2\right) & \mathrm{Tr}\left(\sigma_3'\sigma_3\right) & \mathrm{Tr}\left(\sigma_3'\sigma_4\right) \\ \mathrm{Tr}\left(\sigma_4'\sigma_1\right) & \mathrm{Tr}\left(\sigma_4'\sigma_2\right) & \mathrm{Tr}\left(\sigma_4'\sigma_3\right) & \mathrm{Tr}\left(\sigma_4'\sigma_4\right) \end{bmatrix} \begin{bmatrix} S_0 \\ S_1 \\ S_2 \\ S_3 \end{bmatrix}, \tag{5.4}$$

or more compactly,

$$\vec{T} = \mathbf{B}\vec{S}. \tag{5.5}$$

As long as the Pauli-like operators of Eq. (5.1) are linearly independent, the 4x4 matrix of Eq. (5.4) (**B**) is invertible. Thus, the Stokes parameters can be recovered from the Stokes-*like* parameters, which come from measurements with *imperfect* waveplates, by inverting Eq. (5.4). The retardances

Waveplate	**Ideal Retardance (rad)**	**Measured Retardance (rad)**	**Deviation (Wavelengths)**
QWP	1.57	1.51	$\approx \lambda/105$
HWP	3.14	3.07	$\approx \lambda/90$

Table 5.1: Waveplate Retardances for Stokes Polarimetry

of the wave plates used to make the projections were characterized as seen in Table 5.1. This resulted in the final, inverted matrix $\mathbf{B}^{-1}$ of Eq. (5.3),

$$\mathbf{B}^{-1} = \begin{bmatrix} 1.000 & -0.035 & 0.002 & 0.000 \\ 0.000 & 0.999 & -0.003 & 0.050 \\ 0.000 & 0.001 & 1.001 & -0.022 \\ 0.000 & 0.035 & -0.002 & 1.000 \end{bmatrix}. \tag{5.6}$$

The fact that $\mathbf{B}^{-1}$ is so close to the identity matrix implies that accounting for the error in the waveplates is likely not significant. In order to check this, Mathematica code was written (by L. Giner) to check how this inversion method would affect projective measurements of intensity for an input state $\vec{S}_i = |H\rangle$. These data can be used to determine what the reconstructed Stokes vector (or density matrix) of the light field will be with the imperfect waveplates. The results are summarized in Table 5.2. Due to the near perfect fidelities, this error was deemed negligible.

State	**Ideal Stokes Vector**	**Simulated Stokes Vector**	**Fidelity**
$\|H'\rangle$	$[1, 0, 0]$	$[1.00, -0.04, 0.09]$	1.00
$\|V'\rangle$	$[-1, 0, 0]$	$[-1.00, 0.05, -0.09]$	1.00
$\|D'\rangle$	$[0, 1, 0]$	$[0.04, 1.04, 0.00]$	1.00
$\|A'\rangle$	$[0, -1, 0]$	$[-0.03, -0.96, 0.00]$	0.99
$\|R'\rangle$	$[0, 0, 1]$	$[-0.00, 0.00, 0.99]$	1.00
$\|L'\rangle$	$[0, 0, -1]$	$[0.00, -0.00, -1.00]$	1.00

Table 5.2: State discrimination for ideal vs. non-ideal waveplates.

5.2 Quantization Errors

Since the SLM uses only 8 bits of information to encode the grayscale values g_{ij} for each pixel, there is an associated quantization error. This error can be expressed as an angular displacement of a Stokes vector on the Poincaré sphere, δ_Q,

$$\delta_Q = \sqrt{\frac{1}{2}\left(\frac{\partial\zeta_1}{\partial g_{ij}}\right)^2 + \frac{1}{2}\left(\frac{\partial\zeta_2}{\partial g_{i'j'}}\right)^2}. \tag{5.7}$$

In words, if one assumes that the retardance per unit grayscale varies approximately linearly (as per the manufacturer's specification), the maximum error in retardance associated with an arbitrary $\hat{T}_{\vec{S}_i\to\vec{S}_o}$ is the Pythagorean sum of one half of the minimum retardance for each phase modulation.

If an average over all linear approximations to the phase-grayscale relationship at each illuminated pixel $\left(i^{SLM}, j^{SLM}\right)$ is taken to determine an average change in phase per one grayscale, $\frac{\partial\zeta_2}{\partial g_{i'j'}} = 0.05\frac{\text{rad}}{\text{grayscale}}$. By Eq. (5.7),

$$\delta_Q = 0.05\frac{\text{rad}}{\text{grayscale}}. \tag{5.8}$$

One reasons that any grayscale value can be inaccurate in phase by ± 0.025 rad. Due to the presence of two phase modulations, each region of the wave front is actually determined by two grayscale values, so the inaccuracy of phase due to quantization errors is reasonably assumed to be $\delta_Q = 0.05$ rad.

Intuitively, this error describes the deviation one can expect in producing a desired polarization state. For the sake of example, consider programming the SLM to produce $|H\rangle = \vec{S} = [1, 0, 0]$, but a phase error of $\delta_Q = 0.05$ rad is present. For the sake of simplicity, assume this phase error speaks to an undesirable rotation (or lack thereof) about the S_2 axis. By the Rodrigues' rotation formula, the state produced will be $\vec{S} = [0.999, 0, -0.050]$, which has a fidelity of 0.9997 with $|H\rangle$.

5.3 Errors in Axes of Rotation

The transformation of Eq. (2.13), $\hat{T}_{\vec{S}_i\to\vec{S}_o} \equiv \hat{R}(\zeta_2, \hat{k}_2)\hat{R}(\zeta_1, \hat{k}_1)$ assumes that $\hat{k}_1 = \hat{s}_1$ and $\hat{k}_2 = \hat{s}_2$. The rotation axis $\hat{k}_1$ can be checked, as explained in Section 3.2.1. The actual axis of rotation of $\hat{k}_1$ averaged over all pixels in the beam waist was found to be $\hat{k}_1' = [0.128, 0.991, 0.044]$. This will result in an angular displacement from the expected position on the Poincaré sphere, and therefore gives rise to an error. If the deviation in rotation axis is itself expressed an an angular displacement, $\theta_{\hat{k}_1'}$, an upper bound on the resultant error in intended polarization, $\delta_{\hat{k}_1'}$, is given by,

$$\delta_{\hat{k}_1'} \leq 2\theta_{\hat{k}_1'}, \tag{5.9}$$

which is deduced from geometrical considerations. It was found that $\delta_{\hat{k}_1'} \leq 0.268$ rad, which corresponds to roughly five levels of grayscale.

Additionally, the axis of rotation for each pixel varies slightly with respect to one another. The largest angular deviation in the axes of rotation between two distinct pixels in the beam waist is

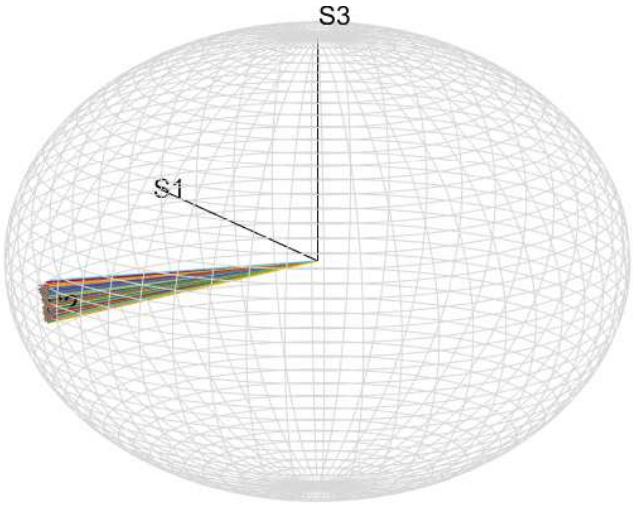

Figure 5.1: The axes of rotation for approximately 10^4 illuminated pixels within the FWTM beam waist on the first incidence are plotted. They deviate from one another, but are generally all about S_2, as expected.

0.2054 rad. Thus, it is expected that minor non-uniformities in polarization will arise in such a way that it cannot be perfectly compensated for. This is discussed in Chapter 6.

5.4 Sources of Signal Loss

As explained in Section 3.1.2, a large transverse phase gradient results in a large transverse component in the wave vector, causing some information within the light field to be lost. The error associated with this is hard to quantify and is more of a visual distortion. A particularly bad example is shown in Fig. 4.14d, the intensity distribution for *Starry Night*. Generally one is able to tell when a large phase gradient will ensue by inspection of the grayscale image – if there is large contrast in the grayscale image, there will be a large phase gradient (see Fig. 4.15). Additionally, the pixelated nature of the SLM leads to diffraction losses [37] and is quantified by a diffraction efficiency by the manufacturer of approximately 90% [42].

Chapter 6

Summary and Discussion

A single spatial light modulator has been used to create modify the polarization state of a light field with very high generality. In particular, a uniform polarization state has been transformed to various other polarization states constituting a SIC-POVM, both uniformly and non-uniformly. Additionally, a uniform polarization state has been modified to encode Van Gogh's *Starry Night* in an elliptical polarization representation.

While all of these transformations resulted in final polarization states that had fidelities upwards of 0.96, it is noted that some of the SIC-POVM states had quantum purities as low as 0.84. For reference, the most pure polarization state that has been realized experimentally has had a purity of 0.98, which results from an initial polarization $\vec{S}_i = |H\rangle$ traversing the setup with zero expected phase modulation from the SLM. Thus, while it is not expected to be able to produce states with perfect purity i.e., $P = 1$, it is expected to be able to produce states with purities at least as high as 0.98. So why is it that two of the SIC-POVM states, namely $\vec{S} = \frac{1}{\sqrt{3}}[-1, 1, -1]$ and $\vec{S} = \frac{1}{\sqrt{3}}[-1, -1, 1]$, have a lower purity than the others, $\vec{S} = \frac{1}{\sqrt{3}}[1, 1, 1]$ and $\vec{S} = \frac{1}{\sqrt{3}}[1, -1, -1]$?

The answer is likely due to the fact that each pixel has a different axis of rotation. In some cases this difference is quite large and can change the intended behaviour of one pixel as much as five grayscales in phase, as explained in Section 5.3. This error will also be more profound for some states than others. In particular, the axes differ in such a way that any states with a positive s_1 component will be constructed more accurately than states with a negative s_1 component, as is obvious by inspection of Fig. 5.1. Here, one can see a large spread in the polarization states at each pixel around $-S_1$ in comparison to $+S_1$. It is precisely the states with a negative s_1 that have the worst purities, since the difference in axes of rotation amongst the pixels is greatest here, resulting in a larger attributable error.

Another cause for imperfect results is the presence of a *grid-like* pattern in polarization that shows up in the colourmaps of the Stokes parameters shown in each result. This grid-like polarization effect is thought to be a result of the experimental setup, as one can see in each of the grayscale images of Section 4.1 that this pattern is noticeable in grayscale. It is not clear why the calibration procedure has resulted in a phase pattern that has grid-like characteristics. One hypothesizes that some sort of diffraction effect from the pixels of the SLM is a possible explanation.

It was mentioned in Section 3.1.4 that forcing a shorter coherence length of the source laser and the tilting of various optical components were employed to counter interference effects. Funda-

mentally, the former seems like the measure that is more effective in stopping interference. The tilting of the NPBS was mainly employed so that the light reflected from the NPBS would not be doubly imaged at the SLM by the 4f system.

Future directions of this work should include using the system to perform transformations that bring a non-uniform state to another non-uniform state for the sake of generality. Additionally, as the technology for transmissive SLMs improve, one may reduce the complexity of the setup by using transmissive devices instead of reflective ones to avoid interference effects or doubly imaging any light as a result of beam overlap. If transmissive SLMs are improved, there may be more opportunity for experiments with three phase modulations from SLMs. This would be especially interesting since a more general transformation described by Eq. (2.11) could be carried out at each pixel [26].

Part II

Non-Abelian Geometric Phase in Silicon Waveguide Arrays

Overview

The sections of Part II are organized as follows: in Chapter 9, a brief motivation is given for pursuing two dimensional transformations in integrated slab waveguides. Additionally, a brief literature review pursuant to geometric phase and quantum computation is given.

Chapter 10 contains theoretical underpinnings as to the description and definition of geometric phase (Section 8.1) and its application to the waveguide array (Section 8.2). It also explains the fundamentals behind non-adiabatic holonomic quantum computation (NHQC).

Chapter 11 contains information about the design and fabrication of the waveguide array. Guiding principles of the design are offered in Section 9.1 and the layout generation and fabrication process are detailed are offered in Sections 9.2 and 9.3, respectively.

Chapter 12 contains simulation data. The simulation consists of an eigenmode expansion (EME) and details of what this means are given in Section 10.1. Convergence of simulation parameters are shown in Section 10.2, and the nominal design performance is discussed in Section 10.3.

Chapter 13 contains details of the experimental setup that was devised for eventual device testing.

Finally, chapter 14 offers a conclusion of the design and simulation work.

Chapter 7

Motivation

One phrase that is often mentioned when discussing quantum technologies is *quantum supremacy*, which refers to realizing a scalable, universal quantum computer - a computer with qubits - that is capable of solving classicaly intractable problems. Classically *tractable* problems are problems that can be solved (with some reasonable error margin) in polynomial time, i.e. bounded-error probabilistic polynomial time (BPP) problems. Classically *intractable* problems are problems that can only be solved in exponential time. If universal quantum computers are realized, they could offer a maximal advantage of solving particular classical, exponentially hard problems in *quantum* polynomial time* [43]. Put simply: quantum computers offer more computational power to solve particular problems. If this power can be appropriately harnessed, it promises to advance medicine, air traffic control, sensing, resource extraction, astronomy – the list goes on and on.

The notion of a quantum computer started in the 1980's, where many introductions and reviews [44], [45] of the subject often make mention of ideas of Yuri Manin [46] or Richard Feynman [47]. Various schemes have been proposed to physically realize a quantum computer, such as linear optical quantum computing (LOQC) [48], trapped-ion quantum computing [49], topological quantum computing [50], superconducting quantum computing [51], geometric quantum computation (GQC) [52], and, more recently, NHQC [53].

In essence, NHQC is very similar to GQC in that geometric phases (or Berry phases) are used to realize unitary transformations. NHQC extends GQC to the non-adiabatic regime and makes use of non-Abelian geometric phases in order to realize unitary transformations. The quantum mechanical formalism of geometric phase in the adiabatic regime was first establshed in 1984 by Sir Michael Berry [54], though Berry himself notes that generalizations of the Berry phase were mentioned earlier [55]. Shortly thereafter, a theoretical generalization of Berry's phase was made to non-adiabatic regimes by Aharanov and Anandan [56]. GQC was built on this non-adiabatic theory by Ekert *et al.* in 2000 [52], where the concepts were applied to quantum circuits and gates. A proof-of-principle experiment in GQC using nuclear magnetic resonance (NMR) was also performed (Jones *et al.*) [57] in 2000. Finally, GQC was extended to non-Abelian regimes in 2012 by Erik Sjöqvist [53]. Both GQC and NHQC are thought to be naturally resilient to specific types of errors due to the fact that the geometric phase is only dependent on the area enclosed by a path tra-

*Quantum computers can solve problems belonging to the complexity class bounded-error quantum polynomial time (BQP). This class is the quantum analog of BPP, but allows for the solution of classically intractable problems (by aid of quintessential quantum properties such as superposition and interference) in polynomial time with a reasonable error margin.

versed in some parameter space of a time dependent Hamiltonian [52]. Small perturbations to this path should not change the total area enclosed by it, thus preserving the geometric phase required to realize a particular unitary transformation. This experiment uses techniques of NHQC in an integrated photonic system to give rise to a platform for quantum computation that can implement any arbitrary, one-qubit unitary transformation. These transformations are intimately related to the polarization transformations of Part I as they too are simply rotations on the Poincaré sphere.

Previously, a proof-of-principle experiment in NHQC has seen success in artificial cold atoms [58] where a Hadamard gate was realized. In photonics, quantum gates operating on NHQC have yet to be realized, though there has been at least one photonic experimental observation of a particular type of geometric phase [59], namely *Abelian* geometric phase. In direct contrast of Abelian geometric phase, another categorization of non-Abelian geometric phase is made. The term *Abelian*[†] makes reference to commutativity. For example, in group theory, when the group operation is performed sequentially on two group elements, the result will not depend on which element was operated on first. The group is then known as being Abelian, or, synonymously, commutative. To the best of the author's knowledge, the completion of this experiment will be the first experimental demonstration of NHQC in a photonic system. Moreover, if the proposal for detecting the non-Abelian geometric phase is successful, it will be the first experimental demonstration of non-Abelian geometric phase in a photonic system.

[†]After Norwegian mathematician Neils Henrik Abel.

Chapter 8

Theory

8.1 Geometric Phase

In order to demonstrate the concept of geometric phase, a classical example will first be provided. First, incorrectly assume that the Earth is flat, and imagine you seek to take some simple journey around the Earth such that you start and finish in the same spot. For the sake of example, consider that this journey consists of travelling 100 kilometres north, followed by 100 hundred kilometres east, followed by 100 kilometres south, and finally another 100 kilometres west. One condition of this journey is that you are *always facing the same direction in your local frame of reference* – you cannot intentionally turn your body left or right from your initial orientation. Thus, in three of the four 100 kilometre stretches of this journey, you must either *side-step* or *back-pedal* to ensure you are maintaining the same initial orientation (the fourth 100 kilometre stretch allows you to simply walk forward and still maintain your initial orientation). After this journey is complete, you would expect to arrive in the same spot you started with a final orientation equal to your initial orientation.

Now consider a similar journey in a realistic view of Earth: a journey that starts and ends in the same spot whilst facing the same initial direction in your local frame of reference, but now the journey is on a *curved surface*. For the sake of example, imagine standing on one of the poles* of the Earth, say the North pole. Imagine initially travelling forward until you reach the equator, then side-stepping the same distance to your right, and then finally back-pedalling the same distance directly behind you.

Perhaps a clever person will realize that this journey will end in the same place it started despite having only three *stretches* instead of four, as in the flat-earth example. But the more crucial point is that the final facing direction will be different from the initial – anyone who makes this journey will be facing a direction 90° away from their initial orientation despite the requirement that one shall not try to do so intentionally. This change in direction is precisely a geometric phase and has been described as a global rotation without any local rotation [60]. The extent to which this rotation occurs is given by the *holonomy* of the connection†. This accumulated phase is a result of

*One need not limit themselves to starting on either pole – any point along the equator will suffice.

†The terms 'holonomy' and 'connection' in this context are mathematically sophisticated and fall within the realm of differential geometry. While they are central to the theoretical underpinnings of NHQC, they are not discussed in this work in detail. They are merely mentioned for background and potential further reading.

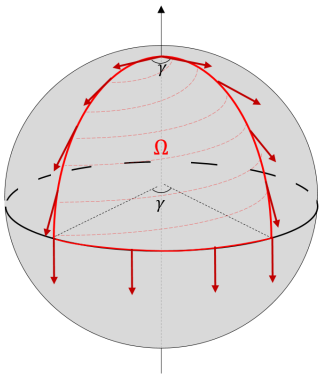

Figure 8.1: A vector subject to parallel transport along a closed loop on a curved surface will acquire a geometric phase γ proportional to the solid angle Ω enclosed by the loop.

two key features of this hypothetical scenario:

1. The journey was subject to *parallel transport*,
2. The journey was cyclic, i.e. it formed a *closed loop* in space

The first item refers to the fact that anyone partaking in this journey was not permitted to locally change the direction they were facing. The second item refers to the fact that the journey began and ended at the same spot. This is a virtue of topology, as the surface of the Earth is curved and gives rise to holonomy. Thus, with these two conditions, a global rotation of a vector is made possible without any explicit local rotation.

The previous example was entirely classical, but the notion of geometric phase was extended to the quantum world in 1984 by Sir Michael Berry [54]. In particular, Berry considered an evolving quantum system with Hamiltonian $\hat{H}(\mathbf{R}(t))$, where the evolution is caused by adiabatically varying the time-dependent, arbitrary parameter $\mathbf{R}(t)$ about a closed path $\mathcal{C}$ such that $\mathbf{R}(t=T) = \mathbf{R}(t=0)$. If the eigenstates of such a system are denoted by $|n(\mathbf{R})\rangle$, the time evolution of the state of the system is given by,

$$|\psi(t)\rangle = e^{-\frac{i}{\hbar}\int_0^t dt' E_n(\mathbf{R}(t'))} e^{i\gamma_n(t)} |n(\mathbf{R}(t))\rangle . \tag{8.1}$$

Here, the first exponential contains the traditional *dynamical* phase, and the second exponential contains the *geometric* phase, which Berry showed is given by,

$$\gamma_n(\mathcal{C}) = i \oint_{\mathcal{C}} \langle n(\mathbf{R}) | \nabla_{\mathbf{R}} n(\mathbf{R}) \rangle \cdot d\mathbf{R}, \tag{8.2}$$

where $\nabla_{\mathbf{R}}$ is the covariant derivative with respect to $\mathbf{R}$. In the language of differential geometry, the integrand is referred to as a *connection*, specifically the *Berry connection*, and is, in this context an imaginary, non-physical quantity. Eq. (8.2) was Berry's main result and the fundamental theoretical aspect of this experiment. An application of Stokes theorem to Eq. (8.2) can express this result in terms of an area as follows,

$$\gamma_n(\mathcal{C}) = -\iint_{\mathcal{C}} d\mathbf{S} \cdot \mathbf{V}_n(\mathbf{R}), \tag{8.3}$$

where,

$$\mathbf{V}_n \equiv \mathrm{Im} \sum_{m \neq n} \frac{\langle n(\mathbf{R}) | \nabla_{\mathbf{R}} \hat{H}(\mathbf{R}) | m(\mathbf{R}) \rangle \times \langle m(\mathbf{R}) | \nabla_{\mathbf{R}} \hat{H}(\mathbf{R}) | n(\mathbf{R}) \rangle}{(E_m(\mathbf{R}) - E_n(\mathbf{R}))^2}, \tag{8.4}$$

and $\mathbf{S}$ is the area enclosed by $\mathcal{C}$. It is useful to display $\gamma_n(\mathbf{R})$ as Eq. (8.3) because it becomes apparent that the geometric phase is proportional to some area enclosed by the curve $\mathcal{C}$ in space $\mathbf{R}$ ($d\mathbf{S}$ is an infinitesimal area element of this space). In fact, as Berry points out, when considering the case of $|n(\mathbf{R})\rangle$ being involved in a two-state degeneracy, Eq. (8.3) reduces tremendously to,

$$\gamma_{\pm}(\mathcal{C}) = \mp \frac{1}{2} \Omega(\mathcal{C}), \tag{8.5}$$

where $\Omega(\mathcal{C})$ is precisely the solid angle subtended by the path $\mathcal{C}$ in $\mathbf{R}$-space. This is why quantum gates that operate on this principle are thought to be robust against specific types of errors; if the path $\mathcal{C}$ is perturbed in such a way that the enclosed area remains constant, the geometric phase should also remain constant. The above treatment relied on adiabaticity, meaning the time evo-

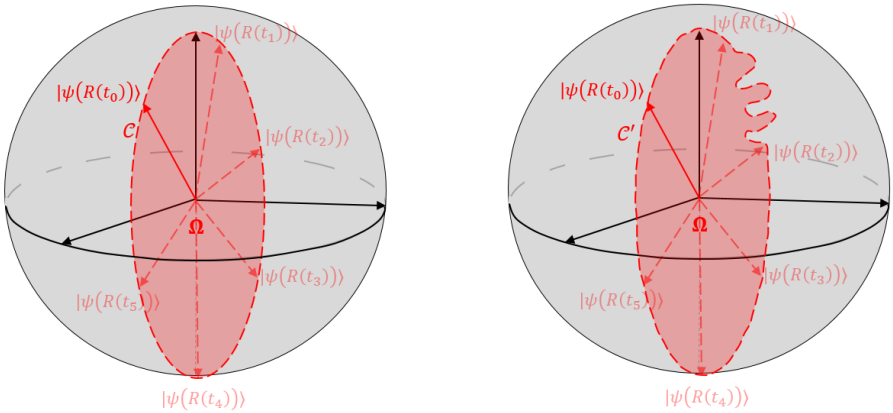

Figure 8.2: Two trajectories of a time evolving state in $\mathbf{R}$-space. On the left, the time evolution of $|\psi\rangle$ traces out a curve $\mathcal{C}$ in $\mathbf{R}$-space. The solid angle enclosed by $\mathcal{C}$ is Ω. On the right, the time evolution of $|\psi\rangle$ traces out a similar curve $\mathcal{C}'$ in $\mathbf{R}$-space – a perturbation occurs between t_1 and t_2. However, as long as the total solid angle Ω enclosed by either curve remains constant, the geometric phase will be identical in either case.

lution of the Hamiltonian was slow enough to make the approximation that, in the Schrödinger picture, any time evolving state could be written as an eigenstate of the instantaneous Hamiltonian. This was expressed through Eq. (8.1) by writing $|n(\mathbf{R}(t))\rangle$. A non-adiabatic generalization relies on choosing initial and final states ($|\psi(t=0)\rangle$ and $|\psi(t=t')\rangle$) that are not eigenstates of the initial Hamiltonian $\hat{H}(t=0)$ and differ only by a phase, i.e. $|\psi(t=0)\rangle = e^{i\gamma} |\psi(t=t')\rangle$ [61]. The initial state is then said to be *cyclic*.

Furthermore, the above treatment makes no mention of the Abelian or non-Abelian nature of the geometric phase. To distinguish between these two geometric phase characterizations in this context, one can imagine a time-dependent Hamiltonian evolving in such a way that it traverses two distinct closed loops in some parameter space. The phase is said to be Abelian if the acquired

geometric phase does not depend on which distinct path was traversed first. The phase is said to be non-Abelian if the acquired geometric phase does depend on which distinct path was traversed first[‡]. Mathematically, Abelian geometric phases correspond to a $U(1)$ (the unitary group of degree one, or the *circle* group – a group of all complex numbers of magnitude one with multiplication) gauge field and non-Abelian geometric phases correspond to a $SU(2)xU(1)$ (a product group composed of the special unitary group of dimension two and circle group) gauge field [62]. Thus, the Abelian nature refers to the *commutativity* (or lack thereof) of sequentially traversing two distinct paths, $\mathcal{C}$ and $\mathcal{C}'$, in the space spanned by $\Omega(t)$, even if both paths start and end in the same spot. If $\Omega(t)$ undergoes cyclic evolution along $\mathcal{C}$ followed by cyclic evolution along $\mathcal{C}'$, the geometric phase accumulated will not be equal to the geometric phase accumulated in the case that $\mathcal{C}'$ was traversed before $\mathcal{C}$ [63],

$$\gamma_{\mathcal{C}'\mathcal{C}} \neq \gamma_{\mathcal{C}\mathcal{C}'}. \tag{8.6}$$

8.2 Mode Transformations in a Three-Waveguide Array

Consider the coupled, three-waveguide device as shown in Fig. 8.3. The device describes a quantum system in a three-dimensional Hilbert space, where the basis vectors are the left, middle, and right waveguides, denoted by $|0\rangle$, $|2\rangle$, and $|1\rangle$, respectively. This quantum system is treated in a

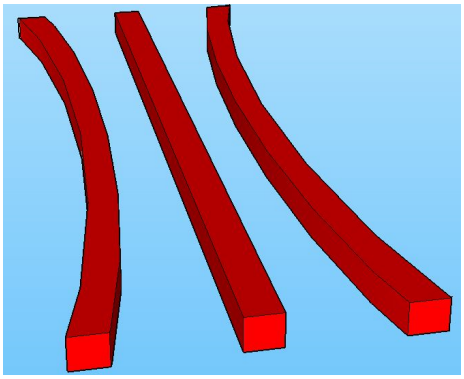

Figure 8.3: A three dimensional model of the waveguide array under investigation. The left, right, and centre waveguides are denoted by $|0\rangle$, $|1\rangle$, and $|2\rangle$, respectively.

similar spirit as induced population transfer in three-level atoms by stimulated Raman adiabatic passage (STIRAP) for the case of zero detuning [64]. In particular, population transfer of photons from $|0\rangle$ to $|1\rangle$ can occur, even though this *transition* is not allowed since the distance between these waveguides is large, creating a negligible probability for tunnelling to occur. The transition $|0\rangle \rightarrow |1\rangle$ is the result of intermediate transitions $|0\rangle \rightarrow |2\rangle$ and then $|2\rangle \rightarrow |1\rangle$, both of which are allowed since the distance between these waveguides is small, enabling a non-negligible probability for tunnelling between them. Computationally, the system is treated as a two-level system with the population of photons in the waveguides labelled $|0\rangle$ and $|1\rangle$ being the computational basis vectors. Population transfer between these waveguides can define unitary operations in this computational basis – a two-level subspace for a qubit to reside in. The formalism is as follows (as

[‡]More on this in Chapter 12

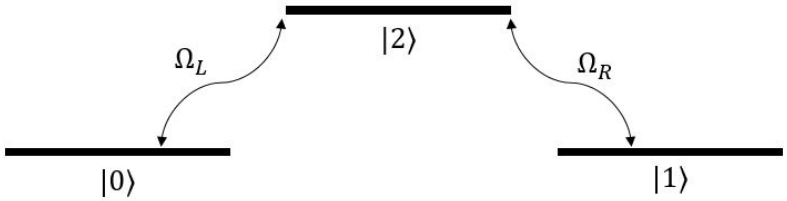

Figure 8.4: A three-level system. Transitions are induced by tunnelling, the rate of which is denoted by $\Omega_{L(R)}$, and may be distinct for the transitions $|0\rangle \rightarrow |2\rangle$ and $|1\rangle \rightarrow |2\rangle$.

compiled and interpreted by the author for use in this experiment from the theoretical work of X. Zhang [65], [66] and E. Sjökvist [53]):

Consider a Cartesian coordinate system such that the length of the centre waveguide (and therefore the propagation direction) is along $\hat{z}$. Let the tunnelling between the left waveguide, $|0\rangle$, and the centre waveguide, $|2\rangle$, be given by Ω_L. Let the tunnelling between the right waveguide, $|1\rangle$, and the centre waveguide, $|2\rangle$, be given by Ω_R. In general, each of these tunnelling rates are characterized by the waveguide-to-waveguide separation d as,

$$\Omega_{L(R)}(d^{L(R)}) = \Omega_0^{L(R)} e^{-\alpha d^{L(R)}}, \tag{8.7}$$

where α is a material-dependent decay constant (coupling coefficient) and $\Omega_0^{L(R)}$ is a proportionality constant $[m^{-1}]$. While the centre waveguide is straight, each adjacent waveguide is bent such that the distances d^L, d^R are characterized by a quadratic bending profile along z,

$$d^L(z) = d_0^L + az^2, \tag{8.8a}$$

$$d^R(z) = d_0^R + az^2, \tag{8.8b}$$

where $d_0^{L(R)}$ is the minimum waveguide separation between the left (right) and centre waveguide and a is a constant $[m^{-1}]$ that characterizes the *strength* of the bending. The tunnelling rates are then functions of propagation distance,

$$\Omega_L(z) = \Omega_0^L e^{-\alpha\left(d^L(z) - d_0^L\right)}, \tag{8.9a}$$

$$\Omega_R(z) = \Omega_0^R e^{-\alpha\left(d^R(z) - d_0^R\right)}. \tag{8.9b}$$

The tunnelling rates of Eq. (8.9) are parametrized as,

$$\Omega_L(z) = \Omega(z) \sin\left(\frac{\theta}{2}\right) e^{i\phi}, \tag{8.10a}$$

$$\Omega_R(z) = \Omega(z) \cos\left(\frac{\theta}{2}\right), \tag{8.10b}$$

where,

$$\Omega(z) = \Omega_0 e^{-\alpha(d(z) - d_0)}. \tag{8.11}$$

One should note that these parametrized couplings can also be interpreted as functions of time since $z = vt$, where v is the effective speed of the photons along the propagation direction. The interaction Hamiltonian for the system is then given in the rotating wave approximation (RWA) by [53],

$$\hat{H}(t) = \frac{\hbar\Omega(t)}{2} |2\rangle \left(\sin\frac{\theta}{2} e^{i\phi} \langle 0| + \cos\frac{\theta}{2} \langle 1| \right), \tag{8.12}$$

which describes Rabi oscillations with Rabi frequency $\Omega(t)$. This analogy requires that traditional energy eigenvalues are interpreted as effective indices, which, in the case of the waveguide array in question, means there are degenerate eigenstates. Since $\hat{H}(t)$ commutes with itself for all time t, the unitary operator describing this system is given by [67],

$$\hat{U}(\tau) = e^{-\frac{i}{\hbar}\int_{-\tau}^{\tau} \hat{H}(t)\, dt}. \tag{8.13}$$

When $\hat{U}(\tau)$ is projected onto the computational basis $\{|0\rangle, |1\rangle\}$, Eq. (8.13) reduces to [53],

$$\hat{U}(\tau)) = \hat{n}\cdot\vec{\sigma}, \tag{8.14}$$

where $\hat{n} \in \mathbb{R}^3$ and $\vec{\sigma} = [\sigma_x, \sigma_y, \sigma_z]$ are the Pauli matrices defined in Part I, Section 2.1. The parametrization of the tunnelling rates in Eq. (8.10) set $\hat{n}$ such that,

$$\hat{n} = \left(\sin\frac{\theta}{2}\cos\phi, \sin\frac{\theta}{2}\sin\phi, \cos\frac{\theta}{2} \right), \tag{8.15}$$

as shown in Fig. 8.5. Thus, $\hat{U}(\tau) \in SU(2)$ implements a universal unitary transformation whose

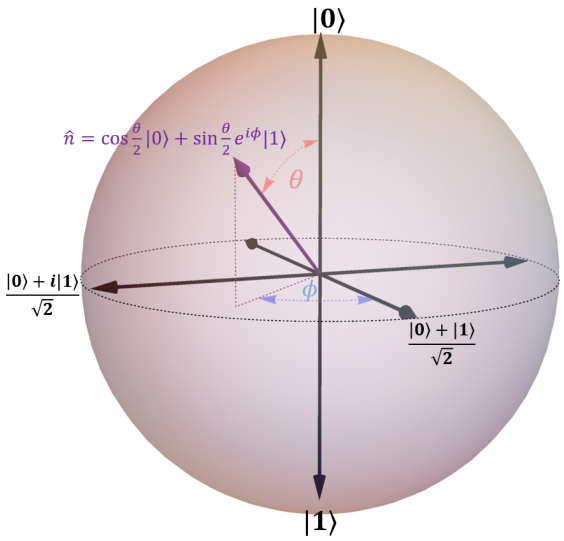

Figure 8.5: The parametrization of Eq. (8.10) depicted on the Poincaré sphere.

definition depends on the parameters θ, ϕ. This transformation can also be visualized as a rotation on the Poincaré sphere.

Now to draw some direct comparisons of how the theoretical underpinnings of geometric phase described in Section 8.1 play a role in the theory surrounding this coupled waveguide device. The time-dependent parameter that Berry's Hamiltonian depends on, $\mathbf{R}(t)$, is equivalent to the parametrized coupling within Eq. (8.12), namely $\Omega(t)$. The evolution of this parameter is guaranteed to be cyclic since [53], [68],

$$\int_{-\tau}^{\tau} \Omega(t)\, dt = \pi, \tag{8.16}$$

which is satisfied by keeping the ratio of the left- and right- waveguide couplings constant for all t. This locking of the ratio is important; doing so ensures that $\hat{H}(t)$ commutes with itself for all t and also satisfies the condition of parallel transport [68],

$$\langle n|\, \hat{H}(t)\, |m\rangle = 0 \,\forall\, m \neq n, \tag{8.17}$$

which is valid within the RWA. The choice of τ corresponds to the choice in device length along z and is explained in the Section 9.1.

Chapter 9

Photonic Chip Design & Fabrication

9.1 Design Principles

Since the material of choice is silicon, some preliminary material-dependent parameters were determined to aid in the design of the device. In particular, the coupling coefficient α was determined by COMSOL simulations for various waveguide separations. The general strategy was to construct two parallel, identical waveguides and separate them by a small distance d. As this simulation progresses, light starting in one waveguide eventually couples to the adjacent waveguide. The effective indices corresponding to the symmetric and antisymmetric supermodes were found for various d. The coupling coefficient can be extracted from these quantities by,

$$\Omega_0 = \frac{\pi \Delta n_{eff}}{\lambda}, \tag{9.1}$$

which follows from considering the system as a double-well potential with *transition time* $t = \frac{\hbar\pi}{E_{antisym} - E_{sym}}$ [69]. Here, Δn_{eff} is the difference in effective indices for the symmetric and antisymmetric supermodes and $\lambda = 1550$ nm is the wavelength of light in vacuum. Finally, a curve is fitted to Eq. (8.7) to find the coupling coefficient α. As mentioned in Section 8.2, the length of the device is a crucial design parameter that is set by Eq. (8.16); the integral of the parametrized coupling over the entire propagation length must be equal to π to guarantee cyclic evolution, a critical aspect for the acquisition of geometric phase. Substituting Eq. (8.11) and Eq. (8.8) into Eq. (8.16) gives,

$$\int_{-\tau}^{\tau} \Omega_0 e^{-\alpha a z^2}\, dz = \pi. \tag{9.2}$$

Using known techniques with respect to Gaussian integrals, namely [70],

$$\int e^{-\alpha a z^2}\, dz = \frac{\sqrt{\pi}\ \mathrm{erf}\left(\sqrt{a\alpha z}\right)}{2\sqrt{\alpha a}} + C. \tag{9.3}$$

A suitable choice of τ (and therefore device length) can be determined. Eq. (9.2) also implies,

$$\Omega_0 = a\alpha\pi, \tag{9.4}$$

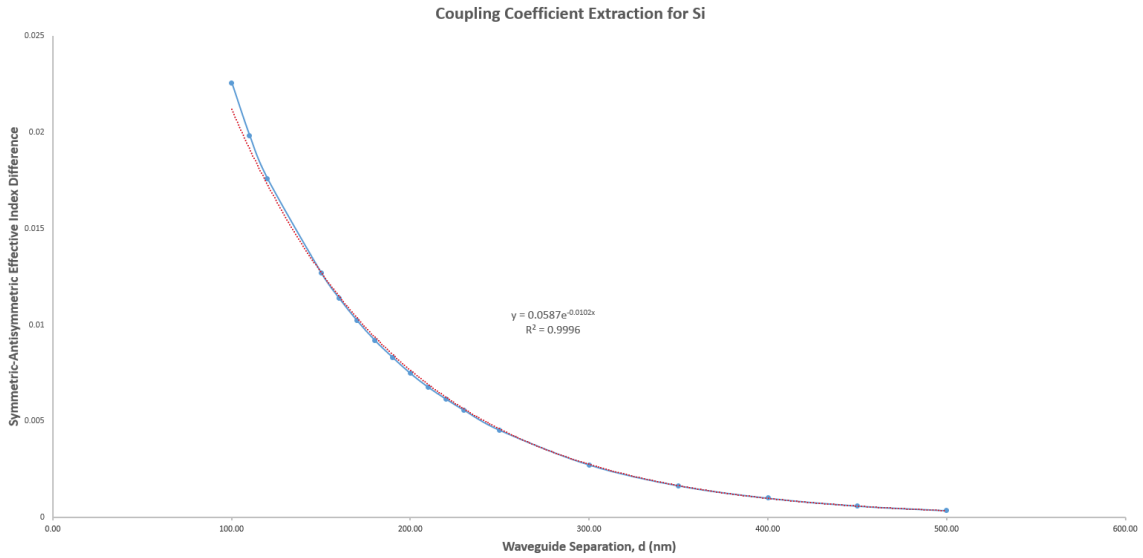

Figure 9.1: Curve fitting to extract the coupling coefficient α for silicon waveguides. This confirms the form of Eq. (8.7). This was initially performed by Dr. Zhang in COMSOL.

which determines the parabolic bending coefficient a of the adjacent waveguides. The simulation data and α can be used to do this; one starts by choosing a reasonable minimum waveguide separation for either adjacent waveguide, $d_0^{L(R)}$. This quantity corresponds to a particular Ω_0 as per the simulation data. Eq. (9.4) relates this Ω_0 to an appropriate parabolic bending coefficient a that should be chosen. With α, Ω_0, and a known, Eq. (9.3) can be evaluated to give an appropriate device length τ. Thus, a set of constant design parameters are known for the waveguide array and are summarized in Table 9.1. The last design consideration depends on the desired unitary

Parameter	**Value**	**Units**
Device Length, 2τ	300	μm
Coupling Coefficient, α	10.2	μ^{-1}
Bending Coefficient, a	$2.07\text{x}10^{-5}$	μ^{-1}
WG Width, w	500	nm
WG Thickness, t,	220	nm
Material	Si	N/A

Table 9.1: Transformation-independent design parameters for the waveguide array.

transformation at hand, which is characterized by θ and ϕ,

$$\hat{U}(\tau) = \begin{bmatrix} \cos\frac{\theta}{2} & e^{i\phi}\sin\frac{\theta}{2} \\ -e^{-i\phi}\sin\frac{\theta}{2} & \cos\frac{\theta}{2} \end{bmatrix}. \tag{9.5}$$

Since the coupling ratio between either adjacent waveguide and the central waveguide must be constant for all t, the parametrized couplings can be divided by one another to find,

$$d_0^L = d_0^R - \frac{\ln\left(\tan\frac{\theta}{2}e^{i\phi}\right)}{\alpha}, \tag{9.6}$$

which describes how the minimum waveguide separations $d_0^{L(R)}$ are related. The first choice of either adjacent waveguide's separation was decided somewhat arbitrarily from the simulation data, but Eq. (9.6) must be used to determine the second adjacent waveguide's separation in terms of the first. By setting $\theta = \frac{\pi}{4}$ and $\phi = 0$ in Eq. (9.5), one can realize a Hadamard (*beamsplitter*) gate ($\hat{U}_H$). By setting $\theta = \frac{\pi}{2}$ and $\phi = 0$, one can realize a Pauli-X (*swap*) gate ($\hat{U}_{\sigma_x}$). The transformations each of these gates perform are visualized on the Poincaré sphere in Fig. 9.2a and Fig. 9.2b. The corresponding waveguide separations used for either of these gates are listed in Table 9.2.

Type of Gate	d_0^L **(nm)**	d_0^R **(nm)**
Hadamard	237	150
Pauli-X	150	150

Table 9.2: Transformation-dependent design parameters for the waveguide array.

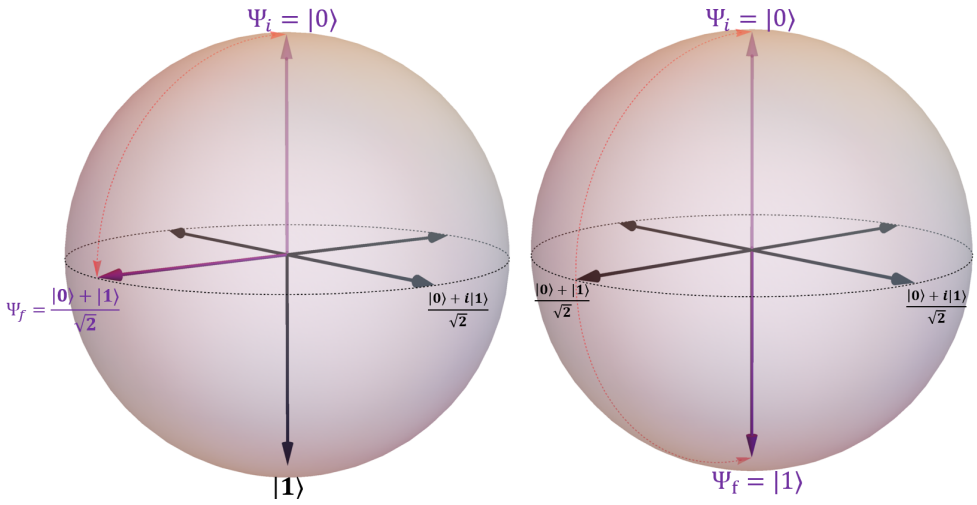

(a) (b)

Figure 9.2: (a) Hadamard gate as visualized on the Poincaré sphere. (b) Pauli-X gate as visualized on the Poincaré sphere.

9.2 Layout

The design area had a floor plan of 2 mm x 3 mm, allowing room for roughly 30 design variations. Each design variation was generated using Mentor Graphics Pyxis Layout, a schematic-driven

layout (SDL) software package that has the capability to import and generate pre-defined library elements in addition to arbitrary polygons. Constructing the bent waveguides was challenging due to the fact that the bending profile was to be parabolic - most bent waveguides are characterized in terms of a radius. Because of this, there were no appropriate pre-defined bent waveguide elements available. To get around this issue, the parabolically bent waveguides were composed of many thin, rectangular slices that fit the prescribed parabolic profile, namely that of Eq. (8.8).

In order to get the light in and out of the waveguide array, fibre grating couplers were used. These were chosen from a compact model library (CML) borrowed from the SiEPIC program. Specifications of these grating couplers are listed below in Table 9.3.

Design Wavelength (nm)	**Angle of Incidence (°)**	**Loss (dB)**
1550	20	10-20 @ 1550 nm (TE)

Table 9.3: Fibre grating coupler specifications.

9.3 Fabrication

The devices were fabricated through the Institute of Microelectronics (IME) multi-project wafer (MPW) program, which was facilitated through the Canadian Microelectronics Corporation (CMC) in collaboration with SiEPIC in Singapore. The fabrication process used 193 nm deep ultraviolet (UV) lithography, enabling 120 nm minimum feature sizes [71]. The fabrication used silicon-on-insulator wafer (Si-SiO_2) with 220 nm thick silicon on 2 micrometer thick silicon dioxide. The substrates were 32mm x 25 mm rectangles diced from 8-inch wafers. After a solvent rinse and hot-plate dehydration bake, Shipley UV210 photoresist was applied for the structure definitions [72]. UV lithography was performed with illumination conditions of numerical aperture of 0.68 and a spatial coherency factor of 0.31. The silicon was removed from exposed areas using an inductively coupled plasma (ICP) low pressure/high density etch system with a chemistry based on $SF_6/C_4F_8/O_2$ is used to etch only the top silicon layer 70 nm deep.

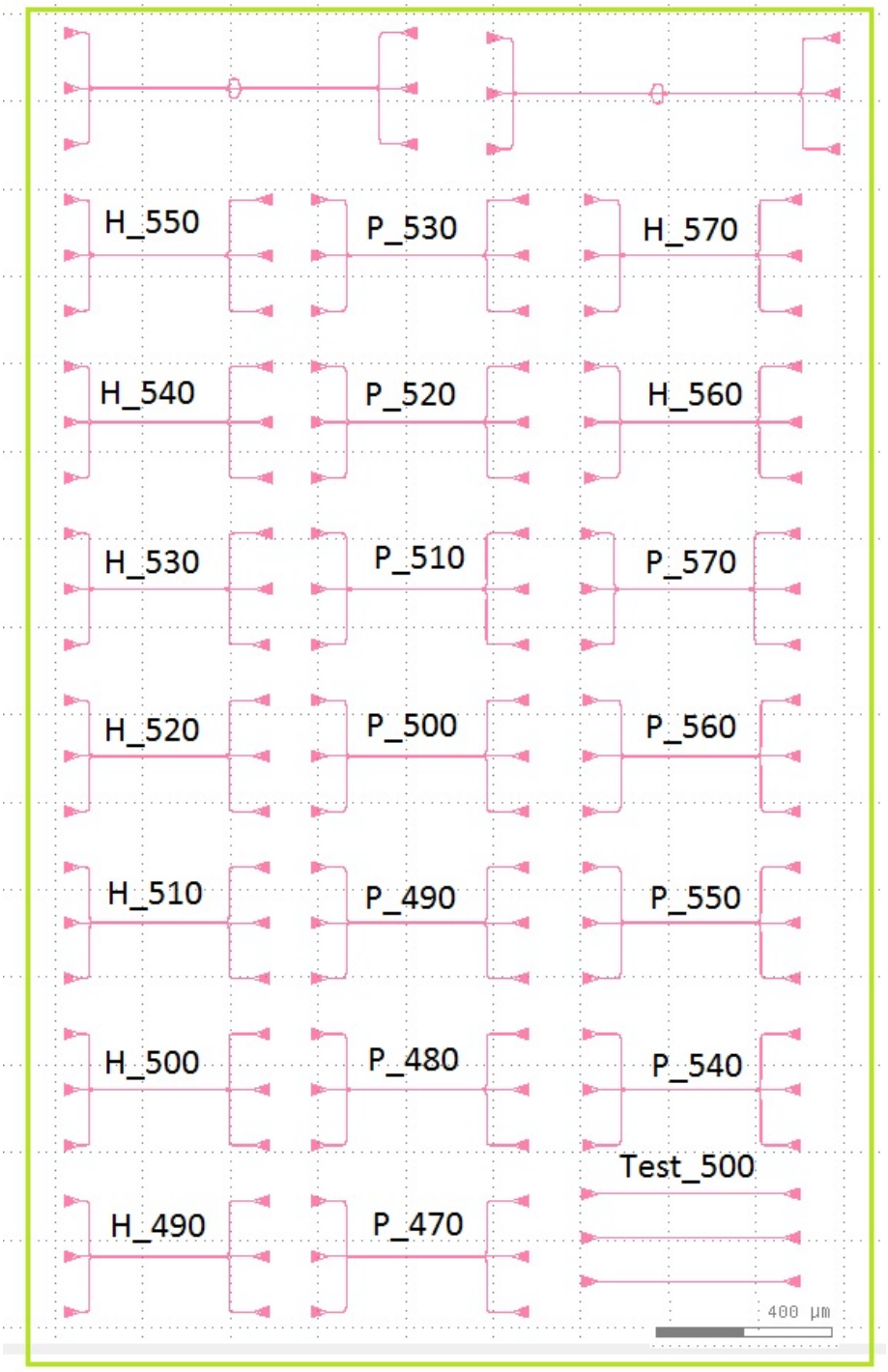

Figure 9.3: Final layout for fabrication. Many design variations were fabricated and are labelled according to device type. Here, 'H' indicates a Hadamard design and 'P' indicates a Pauli-X design. The numbers after the H (or P) indicate the waveguide width in nanometres. Several test structures (shown at the bottom right) were included to determine the insertion loss of the grating couplers.

Chapter 10

Simulations

10.1 Eigenmode Expansion Method

The performance of the waveguide array was determined through simulation. In particular, one sought to verify that Hadamard and Pauli-X configurations performed as expected. For a Hadamard gate, one would expect that launching light into one input port ($|0\rangle$ - the left waveguide or $|1\rangle$ - the right waveguide) would result in an even splitting of light between the two output ports. For a Pauli-X gate, one would expect that launching light into an input port $|0\rangle$ would result in all of the light exiting through output port $|1\rangle$ and vice-versa. A fully vectorial finite difference frequency domain (FDFD) method known as the EME method was used to carry out the simulation.

Consider the waveguide array as shown in Fig. 10.1. The EME method makes use of Yee's mesh [73] over some region of interest to solve Maxwell's equations in two dimensions for each mesh cell distributed along z. Appropriate boundary conditions are applied between each cell at position z so that the electric field equations can be written in terms of eigenmodes within each cell boundary. Finally, an S-matrix can be written at each cell boundary along z so that the field can be propagated from one cell along z to the next throughout the entire length of the device [74].

One source of inaccuracy with the EME method is the *staircase approximation*, where curved surfaces are discretized with Cartesian (straight) boundaries. In order to improve this approximation, an effective index technique is employed such that a particular cell's index of refraction is the result of an average between adjacent cells [74].

10.2 Convergence Testing

In order to ensure the simulation environment was stable, three simulation parameters were varied until device performance converged. The device under test (DUT) was a Hadamard design with a waveguide width of 500 nm. The input light field was transverse electric (TE) polarized with a wavelength of 1550 nm. The intensity at each output port was monitored for numerous trial runs. Each run varied one particular simulation parameter until the intensity readings in each output port each converged to a stable value. The relevant simulation parameters that were varied include the transverse mesh resolution (in mesh cells per micrometer), the number of sub-

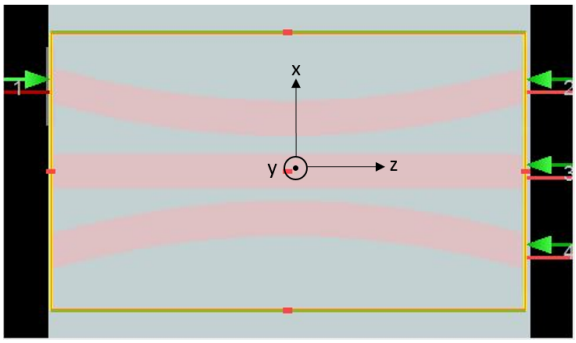

Figure 10.1: Labelled Hadamard gate in Lumerical MODE simulation environment. Here, one can see the input port (1) and the output ports (2,3,4) and the simulation region (orange).

cells (the number of longitudinal mesh cells over the entire device), and the number of modes to calculate. Each of these parameters was initially set somewhat arbitrarily such that a fast (but inaccurate) simulation was performed. Then, one at a time, each of these parameters was increasingly varied until convergence was ascertained. A more quantitative description of this *parameter sweep* is shown in Fig. 10.2 - Fig. 10.4 for the Hadamard design. Other simulation settings are provided in Table 10.1.

Background Index	1
Temperature	300 K
Wavelength	1550 nm
Boundary Conditions	Metal
Input Polarization	Fundamental TE

Table 10.1: Simulation Settings

10.3 Nominal Design Performance

The nominal design parameters for the Pauli-X gate and Hadamard gate are the parameters in Table 9.1 and Table 9.2.

In order to quantify the performance of either gate, one introduces a quantity that speaks to the relative populations in the output ports of the computational basis, and a quantity that speaks to loss. The former is the *logarithmic extinction ratio*, given by,

$$r_e = 10 \log_{10} \left(\frac{I_{|0\rangle}}{I_{|1\rangle}} \right), \tag{10.1}$$

and the latter is the power loss, P_{dB},

$$P_{dB} = 10 \log_{10} \left(\frac{I_{|0\rangle} + I_{|1\rangle}}{I_0} \right), \tag{10.2}$$

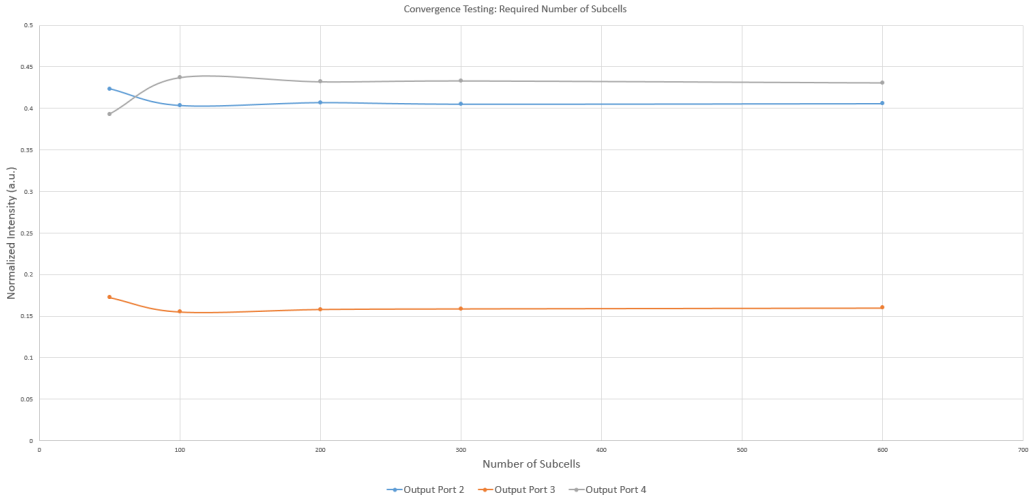

Figure 10.2: Convergence in output port intensity for variation in the number of simulation sub-cells. A total of 300 sub cells was determined to be the optimal value for this parameter.

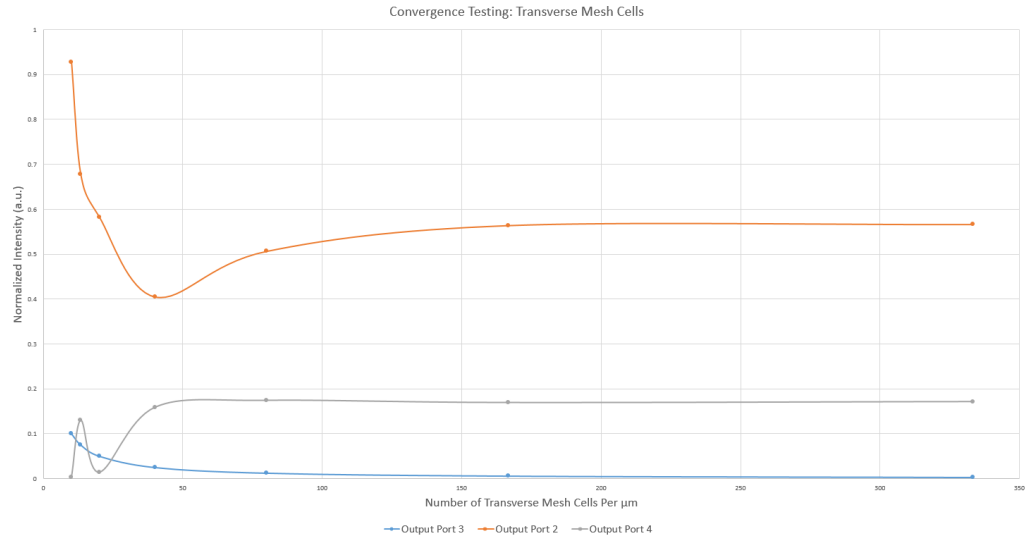

Figure 10.3: Convergence in output port intensity for variation in the number of transverse mesh cells. A total of 167 transverse mesh cells per micrometer was determined to be the optimal value for this parameter.

where $I_{|0\rangle}$ is the intensity in outut port $|0\rangle$, $I_{|1\rangle}$ is the intensity in output port $|1\rangle$, and I_0 is the input intensity. For the Hadamard gate, these quantities are compared to theory and also a simulation of a *beam-splitting* multi-mode interferometer (MMI) [75] in Table 10.2. Additionally, the relative intensities of each output port are given in Table 10.4 as percentages.

For the Pauli-X gate, these simulated quantities are compared to theory and also a simulation of

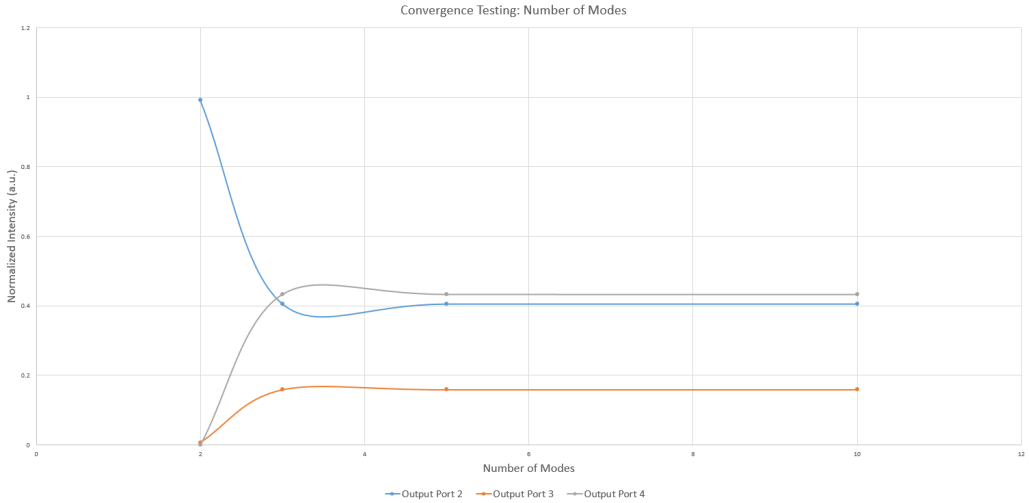

Figure 10.4: Convergence in output port intensity for variation in the number of modes. A total of 3 modes was determined to be the optimal value for this parameter.

a photonic crystal (PhC) waveguide system [76] that implements an optical logical NOT operation in Table 10.3. This device was chosen for comparison since it uses the same metric for simulating device performance, namely the *logarithmic extinction ratio* r_e of Eq. (10.1). The relative intensities of each output port are given in Table 10.4 as percentages.

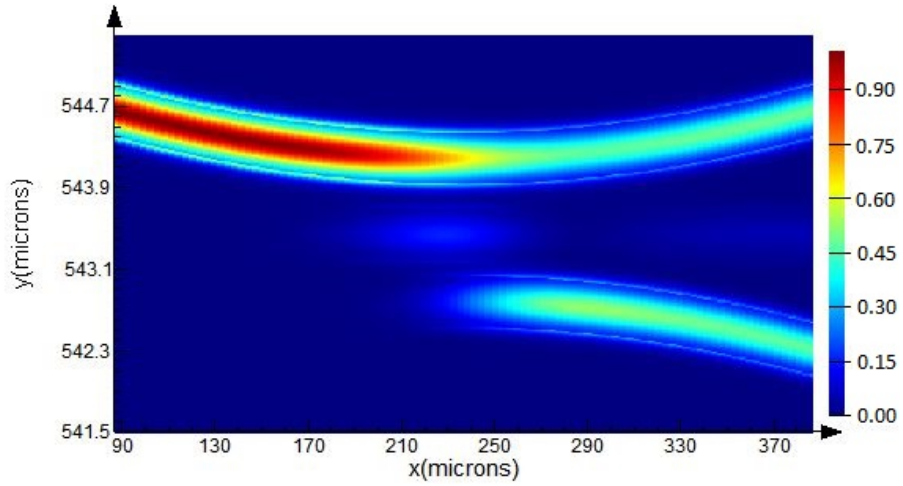

Figure 10.5: The intensity of the electric field throughout the Hadamard gate as simulated by EME. One sees a near perfect splitting of the intensity in either adjacent waveguide, as expected.

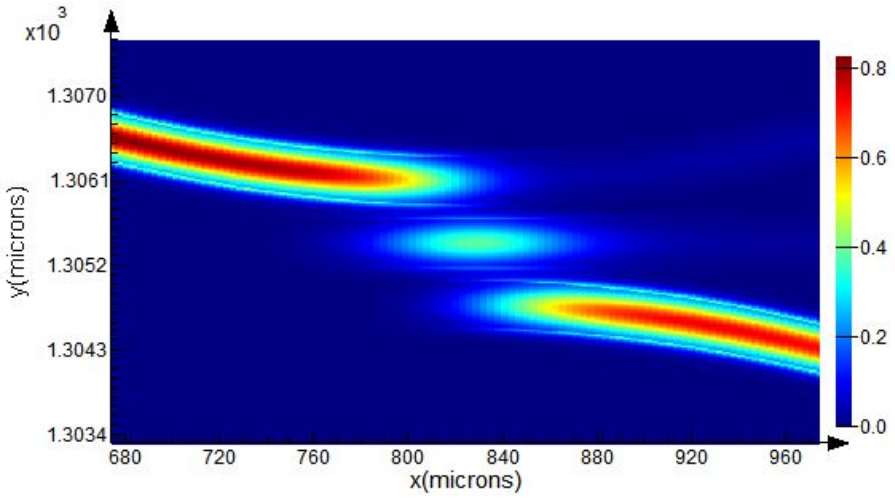

Figure 10.6: The intensity of the electric field throughout the Pauli-X gate as simulated by EME. One sees good extinction between the two output ports.

Data	r_e **(dB)**	P_{dB} **(dB)**
Theory	0	0
Sim (MMI)	0.6	$\leq$1
Sim	0.13	0.22

Table 10.2: Performance of Hadamard gate.

Data	r_e **(dB)**	P_{dB} **(dB)**
Theory	∞	0
Sim [76]	24.73	9
Sim	14.15	-0.25

Table 10.3: Performance of Pauli-X gate.

Device	**Output Port 2 -** $\|0\rangle$	**Output Port 3 -** $\|2\rangle$	**Output Port 4 -** $\|1\rangle$
Hadamard	48.2%	4.9%	46.8%
Pauli-X	3.5%	5.6%	90.9%

Table 10.4: Relative intensities ($\propto \left|\vec{E}\right|^2$) at each output port of each gate. Ideally, all of the intensity would be in Output Port 4 for the Pauli-X gate, and an even split (50%) of intensity would be in Output Port 2 and 4 for the Hadamard gate.

10.4 Robustness

As mentioned in Section 8.1, the geometric nature of these devices should prove robust against any errors that perturb the variation of the cyclic path of the waveguide-to-waveguide coupling over time in such a way that the area enclosed by the path remains constant. There were several considerations as to how these errors could manifest themselves physically in typical fabrication processes.

The time-dependent waveguide-to-waveguide coupling $\Omega(t)$ is the key parameter dictating the acquisition of geometric phase in these devices. The key parameters that affect this coupling are α, the material- and geometry-dependent coupling coefficient, as well as the waveguide separation, d, as is evident from Eq. (8.7). Therefore the errors that should be under consideration are variations in either α or d.

In the case of the latter, the idea is simple: if the waveguide separation does not follow *exact* parabolic behaviour as a function z, but rather has a, say, sinusoidal-like variation associated with it, the average deviation integrated over the entire path is null and the geometric phase is preserved. This idea is simple, but it offers an intuitive description of the types of errors that should be kept in mind when considering robustness.

In the case of the former, one could imagine that the coupling coefficient itself varies, i.e. $\alpha = \alpha(\mathbf{R}(t))$, in some *area preserving* way. One parameter that this coupling coefficient depends on is the waveguide width, w [77]. This parameter is indeed somewhat relevant, as the most common and troublesome errors resulting from the fabrication process of integrated optical devices are surface roughness of the Si wafer and side-wall roughness of the waveguides, which, in the case of the latter, gives rise to propagation losses on the order of 2.4 dB/cm for the design wavelength and polarization (TE) under consideration [78]. If these 'roughnesses' can be thought of as small, sinusoidal variations in the waveguide width and height, then perhaps the integral of these variations will again average to zero such that the geometric phase remains as desired.

Note that the errors that these devices would be robust against are rather specific. If the coupling is varied in such a way that is *not* area preserving, one can expect the device to fail entirely. For example, in the layout that was fabricated, the waveguide width w was varied from device to device, keeping all other parameters in Table 9.1 and Table 9.2 constant. The simulated performance degraded for the Hadamard gate for any $w \neq 500$ nm, the nominal design waveguide width (see Fig.10.7 and Fig.10.8). In hindsight, this should have been obvious since changing the waveguide width will change α - a very crucial design parameter.

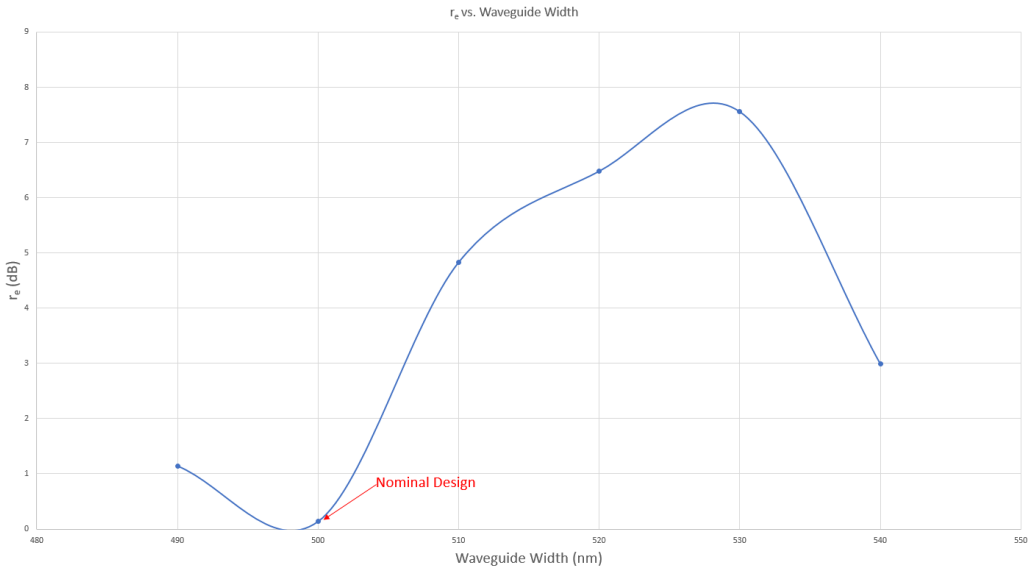

Figure 10.7: r_e vs. waveguide width for the Hadamard gate.

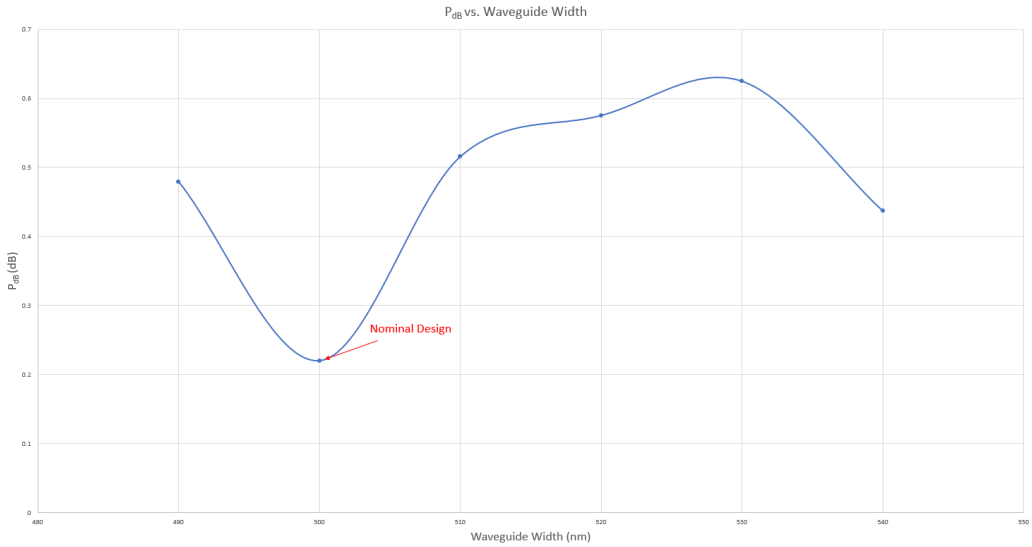

Figure 10.8: P_{dB} vs. waveguide width for the Hadamard gate.

Chapter 11

Experimental Setup

11.1 Description

The sample is placed on a vacuum stage between two, 6-axis translational stages (Thorlabs NanoMax Series) as in Fig. 11.1. Each translation stage supports a custom fibre array and fibre array holder. One stage is for the device input and the other is for the device output. Each fibre array holder is mounted on a custom-built aluminum wedge for proper angle tuning for the fibre grating couplers, as the incident light must be at an angle of 20° with respect to the normal for optimal coupling. Light at 1550 nm from a tunable, fibre pig-tailed source (Koshin Kogaku LS-601A) is routed into the input fibre array after its polarization is tuned to TE through the use of an in-line fibre polarization controller (PLC-900) and polarizer (Thorlabs ILP1550PM). Light from the input fibre array couples to the device through fibre grating couplers. Light from each output port of the device couples to three separate channels of the output fibre array through fibre grating couplers, where each channel is routed to its own photodetector (Thorlabs PDA20CS). A microscope is mounted above the sample with a live CCD camera to aid in the alignment of the fibre array channels with the individual waveguides. In addition to the schematic shown in Fig. 11.1, Table 11.1 contains all specific part details of the experimental setup.

11.2 Loss Considerations

Theoretically, the dominant loss mechanism in the experimental setup is expected to be the fibre-to-chip coupling. In general, the task of coupling light from a fibre to an integrated optical waveguide is difficult due to the mode mismatch, as it is not uncommon for the cross-sectional area between the fibre mode and the waveguide mode to differ by a two orders of magnitude. Fibre grating couplers can improve this coupling by taking advantage of diffraction modes that result from their periodic structure. The grating couplers used in this setup capture only one diffraction mode, and are therefore still inefficient. These grating couplers have been previously tested by Chrostowski *et al.* [79] and, as a result, one expects a minimum insertion loss of 10 dB for the design and setup parameters per grating coupler.

There are also propagation losses associated with silicon waveguides resulting from scattering in the waveguide. As mentioned in Section 10.4, contributors to this scattering include waveg-

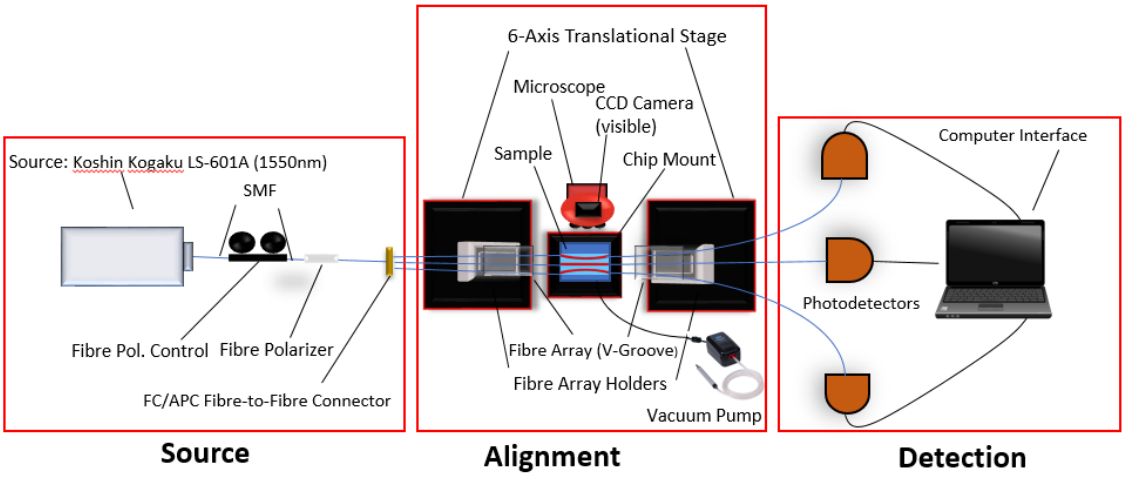

Figure 11.1: Schematic of experimental setup. All fibres are PMFs unless otherwise specified as SMFs.

Component	Part Number	Specs.
Laser	Koshin Kogaku LS-601A	1.5 mW @ 1550nm
Polarizer	Thorlabs ILP1550PM	900 μm jacket, 8.2/125 μm core/clad.
Polarization Ctrl.	Thorlabs PLC-900	900 μm jacket, 780 - 1550 nm
Fibre Array	PLCC Custom	PM fibres, 127 μm pitch, 13.5° polish angle
Fibre Array Holder	Thorlabs HFA001	12 mm width
PMF	OZ Opt. PMJ-3A3A-1550-8/125-1-1-1	30 dB Extinction Ratio
SMF	Thorlabs SMJ-28-J9	Custom 900 μm jacket
Photodetector	Thorlabs PDA20CS	800 - 1700 nm, SM Coupled
Translational Stage	NanoMax 603D	1 nm / 0.018 μrad resolution*
Vacuum Pump	Virtual TV-100	1.7 lpm flow rate
Sample Mount	Thorlabs AMA034	N/A
Fibre Holder Wedges	Custom Machined	20° incline, 0.24 kg

Table 11.1: Part details for experimental setup. *With internal piezo-drive.

uide sidewall roughness and surface roughness of the silicon wafer. Analytical models have been proposed [80] to describe this loss with the power loss per unit length, and for silicon strip waveguides, the loss is generally between 2-3 dB/cm [79]. This translates to approximately 0.06 - 0.09 dB loss for the designs herein.

In general, there are also bend losses associated with any waveguide that is not straight. The general rule of thumb is that the bending should correspond to a radius no smaller than $5 - 10$ μm to mitigate these losses [79]. While one cannot directly associate a radius with the parabolic bending profile used in this design, the bending is negligible in loss considerations due to the very small magnitude of a, the second order coefficient that characterizes the quadratic bending profile.

Each component in the setup will offer some sort of insertion loss. The minimum losses asso-

ciated with each component are summarized in Table 11.2 below.

Component	**Loss (dB)**
Grating Coupler (x2)	20
Polarizer (ILP1550PM)	0.6
Polarization Controller (PLC-900)	0.05
Propagation Losses	0.06
Theoretical Loss Total	**20.71**

Table 11.2: Sources of loss in the experimental setup. The fibres are assumed to be lossless, and each value in dB is the absolute minimum associated with each component.

Chapter 12

Summary and Discussion

The concept of quantum geometric phase has been applied to integrated optical devices for applications in quantum information. In particular, a one qubit Hadamard gate and one qubit Pauli-X gate were designed, simulated and sent to IME for fabrication. An experimental setup was also designed (and partially constructed) in order to test these devices. The physical setup construction was not completed nor was the physical testing carried out due to sole fact that device fabrication and shipment was severely delayed.

Overall, the finite-difference frequency domain simulation of the Hadamard gate was successful, outperforming the broadband MMI simulated in [75] in both extinction ratio (0.13 dB) and loss (0.22 dB). The Pauli-X gate did not outperform the PhC device simulated in [76] in terms of extinction ratio (14.15 dB), but it did outperform it in loss (-0.25 dB).

As alluded to in Chapter 7, the waveguide array exhibits non-Abelian geometric phase. This non-Abelian effect has been exploited experimentally in non-photonic systems [58],[81] that operate on the same principles as this waveguide array. One such experiment took advantage of an artificial three-level atom [58], as mentioned in Chapter 7. The non-Abelian effect was exploited by noting a π phase shift when comparing the final state resulting from first applying a Hadamard operation followed by a Pauli-X operation against applying a Pauli-X operation followed by a Hadamard operation (since $[\hat{U}_H, \hat{U}_{\sigma_x}] \neq 0$). Future experimental work of this experiment will certainly involve an attempt to to detect this phase shift. One would need a method to accurately measure the phase that comes out of each output port of the device; standard bulk-optic interferometric techniques such as comparing the output to some reference signal in a Mach-Zehnder interferometer (MZI) would not be feasible due to the precision in the knowledge of path lengths required. However, it is thought that on-chip interferometric techniques may hold possibility in determining the output phases (see Fig. 12.2). If two signals that are equal and opposite in magnitude but out of phase by π interfere, one would expect completely destructive interference. If the signals were equal and opposite in magnitude but were not out of phase at all and interfere, one would expect completely constructive interference. Both of these cases would manifest themselves in intensity, as the former would have no intensity at all, and the latter would theoretically have no loss at all. This interference could be facilitated by fabricating a 2x1 combiner or *Y-branch* that joins the output ports of the composite Hadamard - Pauli-X device. Another direction for future work would involve simulating, fabricating, and then experimentally verifying different devices that implement more arbitrary rotations on the Poincaré sphere. This would further confirm the

flexibility of the possible unitary operations the waveguide array can implement.

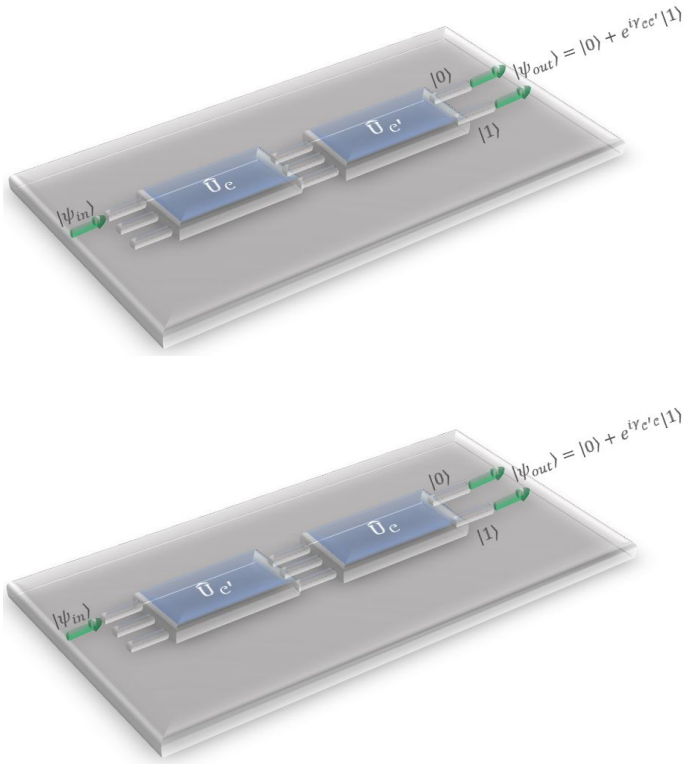

Figure 12.1: When two distinct waveguide arrays implementing $\hat{U}_C$ and $\hat{U}_{C'}$ are in series, the order matters in determining the geometric phase, and therefore the final state $|\psi\rangle$.

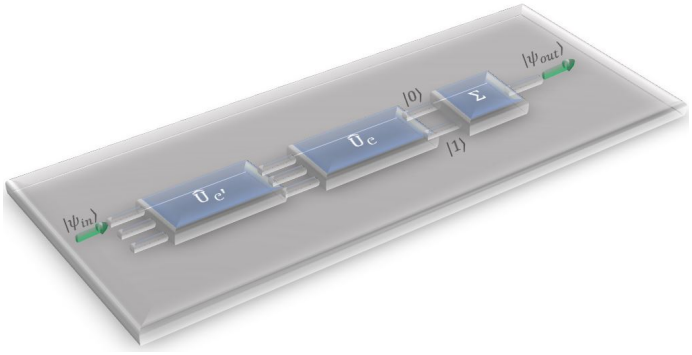

Figure 12.2: Schematic of proposed layout to detect non-Abelian geometric phase.

Chapter 13

Final Conclusion and Future Work

Two experiments exploring transformations of two dimensional photonic degrees of freedom have been examined in detail. The experiment of Part I described non-uniform polarization transformations in free space in the context of rotations on Poincaré sphere. The experiment of Part II described integrated waveguide mode transformations in the context of rotations on the Poincaré sphere.

The polarization transformation experiment of Part I was carried out to completion with experimental results. It was found that an SLM can facilitate two orthogonal rotations on the Poincaré sphere, allowing for arbitrary-known to arbitrary-known polarization transformations for input states with $s_1 = 0$. The waveguide mode transformation experiment of Part II was not carried out to completion due to the delay in fabrication of the integrated waveguide array(s). Numerical results were carried out, and it was found that the waveguide array could perform a single rotation on the Poincaré sphere to realize a Hadamard gate and a Pauli-X gate.

While each of these experiments in two dimensional transformations offer distinct applications, they both fit the mould for applications in quantum information through the Poincaré sphere. In particular, the Hadamard gate and Pauli-X gate are used for single qubit operations, but these are not the only single qubit operations that the waveguide array can realize. The parameters θ and ϕ of Section 8.2 can be tuned to design any single qubit gate, and therefore provide a universal set of single qubit gates – one prerequisite for a quantum computer. Moreover, polarization transformations are paramount to the sect of quantum information known as quantum cryptography. It was shown that non-uniform polarizations could be used to encode and decode entire images. Perhaps this work could be extended to encoding and decoding more abstract information for cryptographic purposes.

Future work for the waveguide mode transformation experiment would involve obtaining experimental data to support the simulations of Section 10.3. Additionally, another fabrication run containing the composite structures of Section 12 could be made in an attempt to exploit non-Abelian geometric phase in a photonic system.

References

[1] R. Dorn, S Quabis, and G Leuchs, "Sharper focus for a radially polarized light beam", *Physical review letters*, vol. 91, no. 23, p. 233 901, 2003.

[2] Y. Zhao, Q. Peng, C. Yi, and S. G. Kong, "Multiband polarization imaging", *Journal of Sensors*, vol. 2016, 2016. DOI: 10.1155/2016/5985673.

[3] T. W. Clark, R. F. Offer, S. Franke-Arnold, A. S. Arnold, and N. Radwell, "Comparison of beam generation techniques using a phase only spatial light modulator", *Opt. Express*, vol. 24, no. 6, pp. 6249–6264, Mar. 2016. DOI: 10.1364/OE.24.006249. [Online]. Available: http://www.opticsexpress.org/abstract.cfm?URI=oe-24-6-6249.

[4] E. Bolduc, N. Bent, E. Santamato, E. Karimi, and R. W. Boyd, "Exact solution to simultaneous intensity and phase encryption with a single phase-only hologram", *Optics Letters*, vol. 38, no. 18, pp. 3546–3549, 2013.

[5] V. Arrizón, U. Ruiz, R. Carrada, and L. A. González, "Pixelated phase computer holograms for the accurate encoding of scalar complex fields", *Journal of the Optical Society of America A*, vol. 24, no. 11, pp. 3500–3507, 2007.

[6] I. Moreno, J. A. Davis, T. M. Hernandez, D. M. Cottrell, and D. Sand, "Complete polarization control of light from a liquid crystal spatial light modulator", *Opt. Express*, vol. 20, no. 1, pp. 364–376, 2012. DOI: 10.1364/OE.20.000364. [Online]. Available: http://www.opticsexpress.org/abstract.cfm?URI=oe-20-1-364.

[7] H. Chen, J. Hao, B.-F. Zhang, J. Xu, J. Ding, and H.-T. Wang, "Generation of vector beam with space-variant distribution of both polarization and phase", *Opt. Lett.*, vol. 36, no. 16, pp. 3179–3181, 2011. DOI: 10.1364/OL.36.003179. [Online]. Available: http://ol.osa.org/abstract.cfm?URI=ol-36-16-3179.

[8] M. A. A. Neil, F. Massoumian, R. Juškaitis, and T. Wilson, "Method for the generation of arbitrary complex vector wave fronts", *Opt. Lett.*, vol. 27, no. 21, pp. 1929–1931, 2002. DOI: 10.1364/OL.27.001929. [Online]. Available: http://ol.osa.org/abstract.cfm?URI=ol-27-21-1929.

[9] C. Maurer, A. Jesacher, S. Fürhapter, S. Bernet, and M. Ritsch-Marte, "Tailoring of arbitrary optical vector beams", *New Journal of Physics*, vol. 9, no. 3, p. 78, 2007. [Online]. Available: http://stacks.iop.org/1367-2630/9/i=3/a=078.

[10] X.-L. Wang, J. Ding, W.-J. Ni, C.-S. Guo, and H.-T. Wang, "Generation of arbitrary vector beams with a spatial light modulator and a common path interferometric arrangement", *Opt. Lett.*, vol. 32, no. 24, pp. 3549–3551, 2007. DOI: 10.1364/OL.32.003549. [Online]. Available: http://ol.osa.org/abstract.cfm?URI=ol-32-24-3549.

[11] S. Franke-Arnold, J. Leach, M. J. Padgett, V. E. Lembessis, D. Ellinas, A. J. Wright, J. M. Girkin, P. Öhberg, and A. S. Arnold, "Optical ferris wheel for ultracold atoms", *Opt. Express*, vol. 15, no. 14, pp. 8619–8625, 2007. DOI: 10.1364/OE.15.008619. [Online]. Available: http://www.opticsexpress.org/abstract.cfm?URI=oe-15-14-8619.

[12] W. Han, W. Cheng, and Q. Zhan, "Design and alignment strategies of 4f systems used in the vectorial optical field generator", *Applied Optics*, vol. 54, no. 9, p. 2275, Mar. 2015, ISSN: 0003-6935, 1539-4522. DOI: 10.1364/AO.54.002275. (visited on 08/01/2017).

[13] E. H. Waller and G. von Freymann, "Independent spatial intensity, phase and polarization distributions", en, *Optics Express*, vol. 21, no. 23, p. 28 167, Nov. 2013, ISSN: 1094-4087. DOI: 10.1364/OE.21.028167. (visited on 08/25/2016).

[14] D. Maluenda, I. Juvells, R. Martínez-Herrero, and A. Carnicer, "Reconfigurable beams with arbitrary polarization and shape distributions at a given plane", *Opt. Express*, vol. 21, no. 5, pp. 5432–5439, 2013. DOI: 10.1364/OE.21.005432. [Online]. Available: http://www.opticsexpress.org/abstract.cfm?URI=oe-21-5-5432.

[15] C.-S. Guo, Z.-Y. Rong, and S.-Z. Wang, "Double-channel vector spatial light modulator for generation of arbitrary complex vector beams", en, *Opt. Lett.*, vol. 39, no. 2, p. 386, Jan. 2014, ISSN: 0146-9592, 1539-4794. DOI: 10.1364/OL.39.000386. (visited on 08/25/2016).

[16] H. Chen, T. Huang, J. Ding, and G. Li, "Independent and simultaneous tailoring of amplitude, phase, and complete polarization of vector beams", *arXiv preprint arXiv:1510.08363*, 2015. (visited on 08/25/2016).

[17] J. A. Davis, D. E. McNamara, D. M. Cottrell, and T. Sonehara, "Two-dimensional polarization encoding with a phase-only liquid-crystal spatial light modulator", *Appl. Opt.*, vol. 39, no. 10, pp. 1549–1554, 2000. DOI: 10.1364/AO.39.001549. [Online]. Available: http://ao.osa.org/abstract.cfm?URI=ao-39-10-1549.

[18] R. L. Eriksen, P. C. Mogensen, and J. Glückstad, "Elliptical polarisation encoding in two dimensions using phase-only spatial light modulators", *Opt. Commun.*, vol. 187, no. 4, pp. 325–336, 2001.

[19] F. Kenny, D. Lara, O. G. Rodríguez-Herrera, and C. Dainty, "Complete polarization and phase control for focus-shaping in high-na microscopy", *Opt. Express*, vol. 20, no. 13, pp. 14 015–14 029, 2012. DOI: 10.1364/OE.20.014015. [Online]. Available: http://www.opticsexpress.org/abstract.cfm?URI=oe-20-13-14015.

[20] I. Estévez, A. Lizana, X. Zheng, A. Peinado, C. Ramírez, J. L. Martínez, A. Márquez, I. Moreno, and J. Campos, "Parallel aligned liquid crystal on silicon display based optical setup for the generation of polarization spatial distributions", in *Modeling Aspects in Optical Metrology V*, B. Bodermann, K. Frenner, and R. M. Silver, Eds., Proc. SPIE, Jun. 2015, 95261A. DOI: 10.1117/12.2184800. (visited on 08/25/2016).

[21] X. Zheng, A. Lizana, A. Peinado, C. Ramirez, J. L. Martinez, A. Marquez, I. Moreno, and J. Campos, "Compact lcos - slm based polarization pattern beam generator", *Journal of Lightwave Technology*, vol. 33, no. 10, pp. 2047–2055, May 2015, ISSN: 0733-8724, 1558-2213. DOI: 10.1109/JLT.2015.2395256. (visited on 08/25/2016).

[22] E. J. Galvez, S. Khadka, W. H. Schubert, and S. Nomoto, "Poincaré-beam patterns produced by nonseparable superpositions of laguerre–gauss and polarization modes of light", *Applied optics*, vol. 51, no. 15, pp. 2925–2934, 2012.

[23] B. E. A. Saleh and M. C. Teich, *Fundamentals of Photonics, 2nd Ed.* Ser. Wiley Series in Pure and Applied Optics. Wiley, 2007, ISBN: 9780471839651.

[24] G. Piquero and J. Vargas-Balbuena, "Non-uniformly polarized beams across their transverse profiles: An introductory study for undergraduate optics courses", *European Journal of Physics*, vol. 25, no. 6, p. 793, 2004. [Online]. Available: http://stacks.iop.org/0143-0807/25/i=6/a=011.

[25] M. Nielsen and I. Chuang, *Quantum Computation and Quantum Information*. Cambridge University Press, 2000, ISBN: 9781107002173.

[26] A. Sit, L. Giner, E. Karimi, and J. S. Lundeen, "General lossless spatial polarization transformations", *Journal of Optics*, vol. 19, no. 9, p. 094 003, 2017. [Online]. Available: http://stacks.iop.org/2040-8986/19/i=9/a=094003.

[27] E. W. Weisstein, *MS Windows NT "inverse tangent." from mathworld–a wolfram web resource.* http://mathworld.wolfram.com/InverseTangent.html, Accessed: June 6, 2017.

[28] E. Hecht, *Optics, 4th Ed.* Pearson Addison Wesley, 2002, ISBN: 9780805385663.

[29] R. W. Boyd, *Nonlinear Optics, 3rd Ed.* Academic Press, 2008, ISBN: 9780123694706.

[30] J. Cornwell, *Group theory in physics*, ser. Techniques of physics v. 1. Academic Press, 1984, ISBN: 9780121898014. [Online]. Available: https://books.google.ca/books?id=MZofAQAAMAAJ.

[31] R. Bhandari, "Synthesis of general polarization transformers. a geometric phase approach", *Physics Letters A*, vol. 138, pp. 469–473, Jul. 1989. DOI: 10.1016/0375-9601(89)90747-0.

[32] E. Karimi, B. Piccirillo, L. Marrucci, and E. Santamato, "Light propagation in a birefringent plate with topological charge", *Opt. Lett.*, vol. 34, no. 8, pp. 1225–1227, 2009. DOI: 10.1364/OL.34.001225. [Online]. Available: http://ol.osa.org/abstract.cfm?URI=ol-34-8-1225.

[33] E. Karimi, "Light orbital angular momentum and its application on the classical and quantum information", PhD thesis, University of Naples, 2009.

[34] J. M. Renes, R. Blume-Kohout, A. Scott, and C. Caves, "Symmetric informationally complete quantum measurements", *Journal of Mathematical Physics*, vol. 45, pp. 2171–2180, Jun. 2004. DOI: 10.1063/1.1737053. eprint: quant-ph/0310075.

[35] E. W. Weisstein, *MS Windows NT "matrix trace." from mathworld–a wolfram web resource.* http://mathworld.wolfram.com/MatrixTrace.html, Accessed: June 7, 2017.

[36] *MS Windows NT imaging and spatial filtering*, https://ocw.mit.edu/courses/mechanical-engineering/2-71-optics-spring-2009/video-lectures/lecture-19-the-4f-system-binary-amplitude-pupil-masks/MIT2_71S09_lec19.pdf, Accessed: Sept. 28, 2016.

[37] J. L. Martínez, I. Moreno, M. del Mar Sánchez-López, A. Vargas, and P. García-Martínez, "Analysis of multiple internal reflections in a parallel aligned liquid crystal on silicon slm", *Opt. Express*, vol. 22, no. 21, pp. 25 866–25 879, Oct. 2014. DOI: 10.1364/OE.22.025866. [Online]. Available: http://www.opticsexpress.org/abstract.cfm?URI=oe-22-21-25866.

[38] Y.-K. Jang and P. Bos, "Analysis of the multireflection effects in compensated liquid crystal devices", *Journal of Applied Physics*, vol. 101, no. 3, 033131, 2007. DOI: 10.1063/1.2464194. eprint: http://dx.doi.org/10.1063/1.2464194. [Online]. Available: http://dx.doi.org/10.1063/1.2464194.

[39] C. Akcay, P. Parrein, and J. P. Rolland, "Estimation of longitudinal resolution in optical coherence imaging", *Appl. Opt.*, vol. 41, no. 25, pp. 5256–5262, Sep. 2002. DOI: 10.1364/AO.41.005256. [Online]. Available: http://ao.osa.org/abstract.cfm?URI=ao-41-25-5256.

[40] S. Belongie, *MS Windows NT "rodrigues' rotation formula." from mathworld–a wolfram web resource, created by eric w. weisstein.* http://mathworld.wolfram.com/RodriguesRotationFormula.html, Accessed: June 30, 2017.

[41] J. B. Altepeter, E. R. Jeffrey, and P. G. Kwiat, "Photonic State Tomography", *Adv. At. Mol. Opt. Phys.*, vol. 52, 2005.

[42] Hamamatsu, *MS Windows NT lcos-slm (liquid crystal on silicon - spatial light modulator)*, http://www.hamamatsu.com/resources/pdf/ssd/x10468_series_etc_kacc1172e.pdf, Accessed: June 20, 2017.

[43] S. Aaronson, *Quantum Computing Since Democritus*. Cambridge University Press, 2013, ISBN: 9780521199568.

[44] A. Steane, "Quantum computing", *Reports on Progress in Physics*, vol. 61, pp. 117–173, Feb. 1998. DOI: 10.1088/0034-4885/61/2/002. eprint: quant-ph/9708022.

[45] E. G. Rieffel and W. H. Polak, *Quantum Computing: A Gentle Introduction*. MIT Press, 2014, ISBN: 9780262526678.

[46] Y. Manin, "Computable and uncomputable", *Sovetskoye Radio*, 1980.

[47] R. Feynman, "Simulating physics with computers", *International Journal of Theoretical Physics*, vol. 21, pp. 467–488, Jun. 1982. DOI: 10.1007/BF02650179.

[48] E. Knill, R. Laflamme, and G. J. Milburn, "A scheme for efficient quantum computation with linear optics", *nature*, vol. 409, no. 6816, pp. 46–52, 2001.

[49] J. I. Cirac and P. Zoller, "Quantum computations with cold trapped ions", *Phys. Rev. Lett.*, vol. 74, pp. 4091–4094, 20 May 1995. DOI: 10.1103/PhysRevLett.74.4091. [Online]. Available: https://link.aps.org/doi/10.1103/PhysRevLett.74.4091.

[50] M. H. Freedman, A. Kitaev, M. J. Larsen, and Z. Wang, "Topological quantum computation", *Bull. Amer. Math. Soc.*, vol. 40, pp. 31–38, 2003. DOI: https://doi.org/10.1090/S0273-0979-02-00964-3. [Online]. Available: http://www.ams.org/journals/bull/2003-40-01/S0273-0979-02-00964-3/S0273-0979-02-00964-3.pdf.

[51] J. Clarke and F. K. Wilhelm, "Superconducting quantum bits", *Nature*, vol. 453, pp. 1031–1042, Jun. 2008. DOI: doi:10.1038/nature07128. [Online]. Available: https://www.nature.com/nature/journal/v453/n7198/full/nature07128.html.

[52] A. Ekert, M. Ericsson, P. Hayden, H. Inamori, J. A. Jones, D. K. L. Oi, and V. Vedral, "Geometric quantum computation", *Journal of Modern Optics*, vol. 47, pp. 2501–2513, Nov. 2000. DOI: 10.1080/09500340008232177. eprint: quant-ph/0004015.

[53] E. Sjoqvist, D. M. Tong, L. M. Andersson, B. Hessmo, M. Johansson, and K. Singh, "Non-adiabatic holonomic quantum computation", *New Journal of Physics*, vol. 14, no. 103035, Oct. 2012. DOI: 10.1088/1367-2630/14/10/103035.

[54] M. V. Berry, "Quantal phase factors accompanying adiabatic changes", *Proceedings of the Royal Society of London A: Mathematical, Physical and Engineering Sciences*, vol. 392, no. 1802, pp. 45–57, 1984, ISSN: 0080-4630. DOI: 10.1098/rspa.1984.0023. eprint: http://rspa.royalsocietypublishing.org/content/392/1802/45.full.pdf. [Online]. Available: http://rspa.royalsocietypublishing.org/content/392/1802/45.

[55] M. Berry, "Anticipations of the geometric phase", *Physics Today*, vol. 43, p. 34, 12 Dec. 1990. DOI: 10.1063/1.881219.

[56] Y. Aharonov and J. Anandan, "Phase change during a cyclic quantum evolution", *Phys. Rev. Lett.*, vol. 58, pp. 1593–1596, 16 1987. DOI: 10.1103/PhysRevLett.58.1593. [Online]. Available: https://link.aps.org/doi/10.1103/PhysRevLett.58.1593.

[57] J. A. Jones, V. Vedral, A. Ekert, and G. Castagnoli, "Geometric quantum computation using nuclear magnetic resonance", *Nature*, vol. 403, pp. 869–871, Feb. 2000. DOI: 10.1038/35002528. eprint: quant-ph/9910052.

[58] A. Abdumalikov Jr, J. Fink, K Juliusson, M Pechal, S Berger, A Wallraff, and S Filipp, "Experimental realization of non-abelian non-adiabatic geometric gates", *Nature*, vol. 496, no. 7446, pp. 482–485, 2013.

[59] P. G. Kwiat and R. Y. Chiao, "Observation of a nonclassical berry's phase for the photon", *Phys. Rev. Lett.*, vol. 66, pp. 588–591, 5 1991. DOI: 10.1103/PhysRevLett.66.588. [Online]. Available: https://link.aps.org/doi/10.1103/PhysRevLett.66.588.

[60] E. Sjöqvist, "A new phase in quantum computation", *Physics Online Journal*, vol. 1, p. 35, Nov. 2008. DOI: 10.1103/Physics.1.35.

[61] D. Moore, "The calculation of nonadiabatic berry phases", *Physics Reports*, vol. 210, p. 3, 1 Sep. 2002. DOI: 10.1016/0370-1573(91)90089-5.

[62] F. Wilczek and A. Zee, "Appearance of gauge structure in simple dynamical systems", *Phys. Rev. Lett.*, vol. 52, no. 24, pp. 2111–2114, 1984. DOI: 10.1103/PhysRevLett.52.2111. [Online]. Available: https://link.aps.org/doi/10.1103/PhysRevLett.52.2111.

[63] B.-L. Weng, D.-M. Lai, and X.-D. Zhang, "Non-abelian geometric phase in four-waveguide arrays", *Phys. Rev. A*, vol. 85, p. 053 801, 5 May 2012. DOI: 10.1103/PhysRevA.85.053801. [Online]. Available: https://link.aps.org/doi/10.1103/PhysRevA.85.053801.

[64] U. Gaubatz, P. Rudecki, S. Schiemann, and K. Bergmann, "Population transfer between molecular vibrational levels by stimulated raman scattering with partially overlapping laser fields. a new concept and experimental results", *The Journal of Chemical Physics*, vol. 92, no. 5363, Jan. 1990. DOI: 10.1063/1.458514.

[65] Y.-X. Du, Z.-Y. Xue, X.-D. Zhang, and H. Yan, "Detecting non-Abelian geometric phases with three-level Λ systems", *Phys. Rev. A*, vol. 84, no. 3, 034103, p. 034 103, Sep. 2011. DOI: 10.1103/PhysRevA.84.034103.

[66] B.-L. Weng, D.-M. Lai, and X.-D. Zhang, "Non-Abelian geometric phase in four-waveguide arrays", *Phys. Rev. A*, vol. 85, no. 5, 053801, p. 053 801, May 2012. DOI: 10.1103/PhysRevA.85.053801.

[67] J. Sakurai and J. Napolitano, *Modern Quantum Mechanics, 2nd Ed.* Addison-Wesley, 2011, p. 71, ISBN: 9780805382914.

[68] A. Abdumalikov Jr., J. Fink, K. Juliusson, M. Pechal, S. Berger, A. Wallraff, and S. Filipp, "Experimental realization of non-Abelian non-adiabatic geometric gates", *Nature*, vol. 496, pp. 482–485, Apr. 2013. DOI: 10.1038/nature12010. arXiv: 1304.5186 [quant-ph].

[69] S. Gasiorowicz, *Quantum Physics, 3rd Ed.* Wiley, 2003, p. 80, ISBN: 9780471057000.

[70] E. W. Weisstein, *MS Windows NT "gaussian integral." from mathworld–a wolfram web resource.* http://mathworld.wolfram.com/GaussianIntegral.html, Accessed: June 16, 2017.

[71] *MS Windows NT passive silicon photonics fabrication course 2016 – technology description*, http://www.cmc.ca/en/WhatWeOffer/Training/Courses/PastCourses/PassiveSiliconPhotonicsFabMay2016.aspx, Accessed: June 13, 2017.

[72] *MS Windows NT design rules for silicon prototyping*, https://www.a-star.edu.sg/Portals/30/IME_Research/NanoPhotonicsProgramme/IME_design%20rules%20for%20silicon%20photonics%20prototyping%20V1_2008.pdf, Accessed: June 13, 2017.

[73] K. S. Yee, "Numerical solution of initial boundary value problems involving maxwell's equations in isotropic media", *IEEE Trans. Antennas Propagat.*, vol. 14, pp. 302–307, May 1966.

[74] Z. Zhu and T. G. Brown, "Full-vectorial finite-difference analysis of microstructured optical fibers", *Opt. Express*, vol. 10, no. 17, pp. 853–864, Aug. 2002. DOI: 10.1364/OE.10.000853. [Online]. Available: http://www.opticsexpress.org/abstract.cfm?URI=oe-10-17-853.

[75] A. Maese-Novo, R. Halir, S. Romero-Garcia, D. Perez-Galacho, L. Zavargo-Peche, A. Ortega-Monux, I. Molina-Fernandez, J. G. Wanguemert-Perez, and P. Cheben, "Wavelength independent multimode interference coupler", *Opt. Express*, vol. 21, no. 6, pp. 7033–7040, Mar. 2013. DOI: 10.1364/OE.21.007033. [Online]. Available: http://www.opticsexpress.org/abstract.cfm?URI=oe-21-6-7033.

[76] C. J. Wu, C. P. Liu, and Z. Ouyang, "Compact and low-power optical logic not gate based on photonic crystal waveguides without optical amplifiers and nonlinear materials", *Appl. Opt.*, vol. 51, no. 5, pp. 680–685, Feb. 2012. DOI: 10.1364/AO.51.000680. [Online]. Available: http://ao.osa.org/abstract.cfm?URI=ao-51-5-680.

[77] K. Okamoto, *Fundamentals of optical waveguides*. Academic Press, 2010.

[78] C. Qiu, Z. Sheng, H. Li, W. Liu, L. Li, A. Pang, A. Wu, X. Wang, S. Zou, and F. Gan, "Fabrication, characterization and loss analysis of silicon nanowaveguides", *J. Lightwave Technol.*, vol. 32, no. 13, pp. 2303–2307, Jul. 2014. [Online]. Available: http://jlt.osa.org/abstract.cfm?URI=jlt-32-13-2303.

[79] L. Chrostowski and M. Hochberg, *Silicon Photonics Design: From Devices to Systems*. Cambridge University Press, 2015.

[80] P. K. Tien, "Light waves in thin films and integrated optics", *Appl. Opt.*, vol. 10, p. 2395, 1971.

[81] J. W. Zwanziger, M. Koenig, and A. Pines, "Non-abelian effects in a quadrupole system rotating around two axes", *Phys. Rev. A*, vol. 42, pp. 3107–3110, 5 Sep. 1990. DOI: 10.1103/PhysRevA.42.3107. [Online]. Available: https://link.aps.org/doi/10.1103/PhysRevA.42.3107.